

**MOLECULAR DYNAMICS SIMULATIONS AND FLOW
INJECTION STUDIES OF HYDROTHERMAL FLUIDS**

by

Andriy Plugatyr

A thesis submitted to the Department of Chemistry
in conformity with the requirements for
the degree of Doctor of Philosophy

Queen's University

Kingston, Ontario, Canada

March, 2009

Copyright ©Andriy Plugatyr, 2009

Abstract

Hydrothermal fluids near and above the critical point of water have unique and potentially very useful thermophysical properties. At present, the lack of knowledge of supercritical water chemistry hinders implementation of innovative hydrothermal technologies. The development of new experimental methods and application of molecular modeling tools is clearly warranted to provide a better understanding of the complex properties of aqueous systems at elevated temperatures and pressures.

The thermodynamic, dielectric and transport properties of hydrothermal fluids are investigated using Molecular Dynamics (MD) simulation and flow injection techniques. The spatial hydration structures and self-diffusion coefficients of phenol, aniline and naphthalene in aqueous infinitely dilute solution are examined from ambient to supercritical conditions by means of MD simulations. It is shown that the solvation shell around aromatic molecules undergoes significant changes along the liquid-vapour coexistence curve and, essentially, disappears at supercritical conditions. The changes in hydration structures are reflected in the values of the self-diffusion coefficients which dramatically increase near the critical point of water. The thermodynamic and dielectric properties of the Simple Point Charge Extended (SPC/E) water model are examined over a broad range of sub- and supercritical states. Accurate thermodynamic and dielectric equations of state (EOS) for the SPC/E water model are presented. The parameterizations provide the most accurate, up-to-date description of the properties of high-temperature SPC/E water, thus enabling for the direct comparison of molecular simulation results with experimental data via the corresponding states principle.

The experimental methodology for the study of aqueous fluids at extreme conditions by using the *ex situ* flow injection technique is presented. The methodology significantly simplifies the technical aspects of flow injection analysis in hydrothermal fluids as sample injection and

detection are performed at ambient temperature, thus allowing the use of standard on-line detection methods. The proposed *ex situ* experimental technique is applied to the examination of the hydrodynamic regime of a flow-through tubular reactor from ambient to supercritical water conditions. Application of the *ex situ* Taylor dispersion technique to measurements of the binary diffusion coefficients in hot compressed water is also presented. The *ex situ* flow injection methodology provides a basis for further development of flow injection analysis techniques at supercritical water conditions.

Co-Authorship

All data presented in the thesis manuscripts was acquired and analyzed by the author unless specified otherwise. MD simulations, described in Chapter 3, were carried out by Istok Nahtigal. The ideas and techniques presented in the manuscripts are original contributions of the author. All manuscripts were edited and co-authored by my supervisor, Dr. I.M. Svishchev.

This thesis is based on the following papers:

1. Chapter 3. I.M. Svishchev, A. Plugatyr and I.G. Nahtigal, Spatial Hydration Maps and Dynamics of Naphthalene in Ambient and Supercritical Water. *J. Chem. Phys.* **128**(12), 124515 (2008)
2. Chapter 4. A. Plugatyr and I.M. Svishchev, The Hydration of Aniline: Analysis of Spatial Distribution Functions. (*accepted to the Journal of Chemical Physics, Feb. 2009*)
3. Chapter 5. A. Plugatyr and I.M. Svishchev, Accurate Thermodynamic and Dielectric Equations of State for High-Temperature Simulated Water. *Fluid Phase Equilibr.* **277** 145 (2009)
4. Chapter 6. A. Plugatyr and I.M. Svishchev, Residence Time Distribution Measurements and Flow Modeling in a Supercritical Water Oxidation Reactor: Application of Transfer Function Concept. *J. Supercrit. Fluids* **44**(1), 31 (2008)
5. Chapter 7. A. Plugatyr and I.M. Svishchev, Diffusion Coefficients of Phenol in Hot Compressed Water: *Ex situ* Taylor Dispersion Technique and Molecular Dynamics Simulations. (*submitted to the Journal of Heat and Mass Transfer, Feb. 2009*)

Other publications by the author on the subject of this thesis:

1. I.M. Svishchev and A. Plugatyr, Supercritical water oxidation of o-dichlorobenzene: degradation studies and simulation insights, *J. Supercrit. Fluids* **37**(1), 94 (2006)
2. A. Plugatyr, I.G. Nahtigal and I.M. Svishchev, Spatial hydration structures and dynamics of phenol in sub- and supercritical water, *J. Chem. Phys.* **124**(2), 024507 (2006)
3. I.M. Svishchev and A. Plugatyr, Hydroxyl radical in aqueous solution: Computer simulation, *J. Phys. Chem. B* **109**(9), 4123 (2005)

Acknowledgements

First and foremost, I am deeply indebted to my mentor and supervisor Dr. Igor M. Svishchev for his guidance and tremendous support throughout the years of my graduate studies.

I would like to thank my supervisory committee members, Dr. Natalie Cann and Dr. Richard Oleschuk, for their valuable suggestions and comments. I would also like to thank Dr. Peter Kusalik and Dr. Bill Atkinson, who acted as external examiners, for their time and advice.

I want to express my gratitude to my friend, colleague and fierce chess opponent, Istok Nahtigal for his help and support. I would also like to thank undergraduate project course students Kathleen Kylie, Scott Cornthwaite and Ewa Golas for their help with flow injection experiments and MD simulations.

My sincere appreciation goes to Trent University Science Workshop staff, Ed Wilson and Ralph Frederick, for their technical assistance with the experimental apparatus.

The financial support of Trent and Queen's Universities, the Ontario Graduate Scholarship program and the Natural Sciences and Engineering Research Council of Canada is greatly appreciated.

My very special and warm thanks go to all my family and friends for their love and overwhelming support during the course of this study. Finally, I would like to express my heartfelt appreciation to my wife, Anna, and my daughter, Masha, who were a constant source of inspiration, encouragement and support throughout my Ph.D. studies.

Statement of Originality

I hereby certify that all of the work described within this thesis is the original work of the author. Any published (or unpublished) ideas and/or techniques from the work of others are fully acknowledged in accordance with the standard referencing practices.

The original contributions of the author are the following:

1. Development of the Mathematica® code for visualization and analysis of spatial distribution functions;
2. Development of the Mathematica® code for parameterization of the equations of state;
3. Construction of a flow-through hydrothermal reactor system;
4. Development of a novel *ex situ* methodology for flow injection studies at high-temperature and supercritical water conditions.

Andriy Plugatyr

March, 2009

Table of Contents

Abstract.....	ii
Co-Authorship	iv
Acknowledgements.....	vi
Statement of Originality.....	vii
Table of Contents.....	viii
List of Figures.....	xi
List of Tables	xiv
List of Symbols and Abbreviations.....	xv
Chapter 1 Introduction.....	1
1.1 Rationale	6
1.2 Objectives	8
1.3 Thesis Outline	9
1.4 References for Chapter 1	10
Chapter 2 Theoretical and Experimental Methods	14
2.1 Molecular Dynamics Simulations.....	14
2.1.1 General Principles.....	15
2.1.2 Molecular Dynamics Simulation Techniques	17
2.1.2.1 <i>Periodic Boundary Conditions</i>	17
2.1.2.2 <i>Potential Truncation</i>	18
2.1.2.3 <i>Ewald Summation Method</i>	20
2.1.2.4 <i>Rigid Body Rotation</i>	22
2.1.2.5 <i>Integration of the Equations of Motion</i>	24
2.1.2.6 <i>Molecular Dynamics in NVT and NPT Ensembles</i>	26
2.1.3 System properties.....	27
2.1.3.1 <i>Thermodynamic Properties</i>	28
2.1.3.2 <i>Structural Properties</i>	29
2.1.3.3 <i>Dynamic Properties</i>	31
2.1.3.4 <i>Dielectric Properties</i>	32
2.1.4 Water Models.....	35
2.2 Flow Injection Techniques.....	39
2.2.1 Residence Time Distribution	39

2.2.2 Transfer Function Concept.....	43
2.2.3 Taylor Dispersion Technique.....	48
2.3 References for Chapter 2	54
Chapter 3 Spatial Hydration Maps and Dynamics of Naphthalene in Ambient and Supercritical Water.....	59
3.1 Abstract.....	59
3.2 Introduction.....	60
3.3 Computational Details	62
3.4 Results and Discussion	64
3.4.1 Analysis of Spatial Distribution Functions	64
3.4.2 Cylindrical Distribution Functions and π -Coordination	71
3.4.3 Self-Diffusion Coefficient.....	75
3.5 Conclusion	77
3.6 References for Chapter 3	78
Chapter 4 The Hydration of Aniline: Analysis of Spatial Distribution Functions.....	80
4.1 Abstract.....	80
4.2 Introduction.....	81
4.3 Simulation Details.....	83
4.4 Results and Discussion	84
4.5 Conclusion	99
4.6 References for Chapter 4	100
Chapter 5 Accurate Thermodynamic and Dielectric Equations of State for High-Temperature Simulated Water	103
5.1 Abstract.....	103
5.2 Introduction.....	104
5.3 Simulation Details.....	108
5.4 Data Sets and Fitting Procedure.....	109
5.4.1 Thermodynamic EOS.....	109
5.4.2 Dielectric EOS	111
5.5 Data Analysis.....	112
5.5.1 Thermodynamic EOS.....	112
5.5.2 Dielectric EOS	119
5.6 Conclusion	122

5.7 References for Chapter 5	123
Chapter 6 Residence Time Distribution Measurements and Flow Modeling in a Supercritical Water Oxidation Reactor: Application of Transfer Function Concept	126
6.1 Abstract	126
6.2 Introduction	127
6.3 Experimental Apparatus and Procedure	131
6.3.1 Experimental apparatus	131
6.3.2 Experimental procedure	132
6.4 Modeling procedure and flow models	134
6.4.1 Flow parameter estimation from <i>ex situ</i> RTD measurements	134
6.4.2 Flow models	138
6.5 Results and Discussion	141
6.6 Conclusion	145
6.7 References for Chapter 6	146
Chapter 7 Diffusion Coefficients of Phenol in Hot Compressed Water: <i>Ex situ</i> Taylor Dispersion Technique and Molecular Dynamics Simulations	148
7.1 Abstract	148
7.2 Introduction	149
7.3 <i>Ex situ</i> Taylor dispersion technique	151
7.4 Experimental Apparatus and Procedures	155
7.4.1 Experimental Apparatus	155
7.4.2 Experimental procedure and flow parameters	156
7.4.3 Simulation details	159
7.5 Results and Discussion	160
7.6 Conclusion	166
7.7 References for Chapter 7	167
Chapter 8 Summary and Future Outlook	171
Appendix A.1	173
Appendix A.2	174
Appendix B.1	174
Appendix B.1	175

List of Figures

Figure 1.1 Pressure-temperature diagram of water	2
Figure 1.2 Pressure-density diagram of water	2
Figure 1.3 Isothermal compressibility of supercritical water.....	5
Figure 1.4 Dielectric constant of water	5
Figure 2.1 Schematic diagram of periodic boundary conditions.	18
Figure 2.2 Schematic representation of point charges in the Ewald summation technique.....	21
Figure 2.3 The oxygen-oxygen, $g_{OO}(r)$, and oxygen-hydrogen, $g_{OH}(r)$, radial distribution functions of the SPC/E water at ambient conditions.....	29
Figure 2.4 The oxygen-oxygen spatial distribution function of the SPC/E water at ambient conditions at a probability level of $g(r, \Omega) = 1.55$	31
Figure 2.5 The normalized linear velocity autocorrelation function of the SPC/E water at ambient conditions.	33
Figure 2.6 The static dielectric constant of the SPC/E water at 460 K and 0.785 g/cm ³ . The block size is 10 ps. Error bars represent standard error of the running average.	34
Figure 2.7 Geometries of water models	37
Figure 2.8 Schematic illustration of the RTD experiment	41
Figure 2.9 Block diagrams and the corresponding transfer functions for a) single, b) sequential, c) parallel and d) positive feedback processes.	46
Figure 2.10 Schematic illustration of the ideal Taylor dispersion experiment	50
Figure 2.11 The effect of solute diffusion on the E -curve for laminar flow in straight tubes of uniform diameter	50
Figure 3.1 Molecular geometry and reference axes for naphthalene	61
Figure 3.2 Total spatial distribution function of (a) oxygen and (b) hydrogen atoms of water around carbon atoms of naphthalene, with a probability level of $g_{CO}(r, \Omega) = 1.6$ and $g_{CH}(r, \Omega) = 1.3$, respectively, at 298 K	65
Figure 3.3 2D plots showing the probability density of oxygens of water around carbons of naphthalene at (a) 298, (b) 473 and (c) 633 K.....	68
Figure 3.4 2D plots showing the probability density of hydrogens of water around carbons of naphthalene at (a) 298, (b) 473 and (c) 633 K.....	69
Figure 3.5 Total coordination numbers, $n_{\text{Naph-O, total}}$, for naphthalene. Also shown are π -coordination numbers, $n_{\text{Naph-O, } \pi\text{-complex}}$ and π -type H-bond numbers, $n_{\text{HB, } \pi\text{-complex}}$	71

Figure 3.6 Cylindrical distribution functions of (a) oxygen and (b) hydrogen atoms of water above and below the plane of an aromatic ring of naphthalene	73
Figure 3.7 Self-diffusion coefficients for naphthalene	76
Figure 4.1 The SDF of water around central aniline molecule at 298 K. Local atomic densities of oxygen (red) and hydrogen (blue) of water are shown at probability levels of $G_O(r, \Omega) = 2.5$ and $G_H(r, \Omega) = 1.8$, respectively. (a) front view; (b) side view; (c) rear view; (d) top view. 85	85
Figure 4.2 The SDF of water around central aniline molecule at 298 K. Local atomic densities of oxygen (red) and hydrogen (blue) of water are shown at probability levels of $G_O(r, \Omega) = 1.65$ for oxygen and $G_H(r, \Omega) = 1.55$ for hydrogen atoms of water, respectively. (a) front view; (b) side view; (c) top view.	86
Figure 4.3 2D maps of local (a) oxygen, (b) hydrogen and (c) charge probability densities of water around aniline at 298 K.	88
Figure 4.4 Radial distribution functions between a) nitrogen – oxygen and b) hydrogen (amino) – oxygen and nitrogen-hydrogen (water) in aqueous aniline solution at 298 K.	91
Figure 4.5 Cylindrical distribution functions of (a) oxygen and (b) hydrogen atoms of water in the axial region of the benzene ring of aniline	92
Figure 4.6 Radial distribution functions between a) nitrogen-oxygen and b) nitrogen-hydrogen (water) and hydrogen (amino) – oxygen in aqueous aniline solution.	94
Figure 4.7 Coordination numbers and number of H-bonds for aniline.....	95
Figure 4.8 2D maps of local (a) oxygen, (b) hydrogen and (c) charge probability densities of water around aniline at 473 K.	96
Figure 4.9 2D maps of local (a) oxygen, (b) hydrogen and (c) charge probability densities of water around aniline at 633 K.	97
Figure 4.10 Self-diffusion coefficient of aniline in aqueous infinitely dilute solution.	98
Figure 5.1 Representative isotherms for the SPC/E water. Continuous lines show isotherms from 500 (bottom curve) to 880 K (top curve) with $\Delta T = 20$ K.....	113
Figure 5.2 Order parameter and the diameter of the coexistence curve as a function of the reduced temperature $\theta = 1 - T/T_c$	113
Figure 5.3 Temperature dependence of the Verschauffelt exponent, β_{eff}	114
Figure 5.4 Liquid-vapour coexistence curve for water.....	118
Figure 5.5 Liquid-vapour coexistence curve, thermodynamic spinodals and line of compressibility maximum of water, κ_T^{MAX}	118

Figure 5.6 Isothermal compressibility of water as a function of reduced density at three selected temperatures above T_c .	119
Figure 5.7 Temperature dependence of the static dielectric constant of the SPC/E water. Continuous lines represent isochors from 0.1 (bottom) to 1.0 g/cm ³ (top).	121
Figure 5.8 Static dielectric constant along the coexistence curve of water.	121
Figure 6.1 Schematics of the flow-through SCWO reactor system	130
Figure 6.2 Schematic diagrams of the a) <i>in situ</i> and b) <i>ex situ</i> RTD measurements	136
Figure 6.3 Block diagrams of the employed flow models	140
Figure 6.4 Examples of experimental and predicted RTD curves using Model 1 (a-d) and Model 2 (e-f) at a) 298 K b) 473 K, c) 648K, d) 748 K, e) 298K and f) 473 K.	143
Figure 7.1 Schematic diagrams of the a) <i>in situ</i> and b) <i>ex situ</i> Taylor dispersion techniques	152
Figure 7.2 a) Schematic diagram and b) photograph of the experimental apparatus	158
Figure 7.3 Examples of the response curves obtained with and without diffusion coil at 25 MPa and a) 298 K, b) 373 K and c) 473 K.	163
Figure 7.4 Temperature dependence of the binary diffusion coefficient of phenol in aqueous solution. The insert shows low temperature data.	164

List of Tables

Table 2.1 Electrostatic, geometric and Lennard-Jones parameters and values for the calculated physical properties of water models.....	38
Table 2.2 The most common flow models used in the RTD studies and the corresponding transfer functions.....	44
Table 2.3 The most common input functions and their corresponding Laplace transforms.....	46
Table 3.1 Simulated state points and self-diffusion coefficients, D_{self} , for naphthalene.....	63
Table 4.1 Electrostatic, geometric, and Lennard-Jones parameters for water and aniline models.....	84
Table 5.1 Critical point parameters of the SPC/E water.....	115
Table 6.1 Summary of the RTD studies in SCWO reactors.....	130
Table 6.2 Summary of the experimental conditions.....	133
Table 6.3 Mean residence times, Péclet numbers and the average <i>RMS</i> error obtained using Model 1.....	144
Table 6.4 Mean residence times, Péclet numbers and the average <i>RMS</i> error obtained using Model 2.....	144
Table 7.1 Electrostatic, geometric and Lennard-Jones parameters for water and phenol models.....	160
Table 7.2 Flow parameters and the limiting binary diffusion coefficient of phenol obtained by using the <i>ex situ</i> Taylor dispersion technique.....	164
Table 7.3 Self-diffusion coefficients of phenol in aqueous infinitely dilute solution obtained by using MD simulations.....	165

List of Symbols and Abbreviations

Chapter 2.1

A	Rotation matrix
a	Acceleration (m s^{-2})
b	Jerk (m s^{-3})
\mathcal{D}_{self}	Self-Diffusion coefficient ($\text{m}^2 \text{s}^{-1}$)
f	Force (N)
\mathcal{K}	Kinetic energy (J/mol)
k_B	Boltzmann constant
M	Total dipole moment of the simulation cell (D)
m	Mass (kg)
N	Number of particles
p	Pressure (Pa)
r	Position
Q	Quaternion
q	Partial atomic charge (e)
l	Bond length (\AA)
T	Temperature (K)
t	Time (s)
v	Velocity (m s^{-1})
\mathcal{V}	Potential energy (J/mol)
$\langle \dots \rangle$	Ensemble average

Greek symbols

α	Ewald convergence parameter
$\bar{\tau}$	Torque (N m)
μ	Molecular dipole moment (D)
ε	Lennard-Jones interaction parameter (kJ mol^{-1})
σ	Lennard-Jones interaction parameter (\AA)
ω	Angular velocity

Abbreviations

MC	Monte Carlo
MD	Molecular Dynamics
MI	Minimum image convention
NPT	Isobaric-isothermal ensemble
NVT	Canonical ensemble
PBC	Periodic Boundary Conditions
RF	Reaction Field
SPC/E	Simple Point Charge Extended
TIP	Transferable Intermolecular Potential

Subscripts and superscripts

cut.	Cut-off
eff.	Effective

Chapter 2.2

a, b	Fourier coefficients
C	Average cross-section solute concentration (mol m^{-3})
d_0	Inner tube diameter (m)
D_{12}	Binary diffusion coefficient ($\text{m}^2 \text{s}^{-1}$)
D_a	Axial dispersion coefficient ($\text{m}^2 \text{s}^{-1}$)
D_c	Coil diameter (m)
De	Dean number, $De = Re \cdot \omega^{-0.5}$ (dimensionless)
$E(t)$	E -curve or the RTD function
$h(s), h_A(s), h_D(s), h^{\text{ADPF}}(s)$	Transfer functions
$I'(t)$	Normalized impulse curve
$i(s)$	Laplace transform of $I'(t)$
L	Characteristic length (m)
\mathcal{L}	Laplace transform

N	number of tanks-in-series
$P'(t)$	Normalized pulse function
$p(s)$	Laplace transform of $P'(t)$
Pe	Péclet number, $Pe = uL/D_a$ (dimensionless)
$R'(t), R'_1(t), R'_2(t)$	Normalized response curves
$r(s), r_1(s), r_2(s)$	Laplace transforms of $R(t), R'_1(t), R'_2(t)$, respectively
Re	Reynolds number, $Re = \rho u d/\mu$ (dimensionless)
s	Laplace domain variable (s^{-1})
Sc	Schmidt number, $Sc = \eta/\rho D_{12}$ (dimensionless)
t	Time (s)
\bar{u}_0	Average cross-section fluid velocity ($m\ s^{-1}$)
ψ	Potential energy (J/mol)
x	Axial coordinate (m)

Greek symbols

$\bar{\tau}$	Mean residence time (s)
μ	Dynamic fluid viscosity (Pa s)
ω	Coil ratio, $\omega = D_c/d_0$
σ^2	Variance
ρ	Fluid density ($kg\ m^{-3}$)

Abbreviations

ADPF	Axially dispersed plug flow
RMS	Root mean square error (%)
RTD	Residence Time Distribution

Subscripts and superscripts

pred.	Predicted
-------	-----------

Chapter 5

a	Helmholtz free energy
b, c, k, l, n, v	fitting parameters
EOS	equation of state
GEMC	Gibbs ensemble Monte Carlo
HRGC	histogram reweighting grand canonical Monte Carlo
k_B	Boltzmann constant
M	total dipole moment
MF-FSS	mixed-field finite-size scaling
MW	molecular weight
p	pressure
R	gas constant
SPC/E	Simple Point Charge Extended
T	temperature
THSG	temperature and hamiltonian scaling Gibbs Monte Carlo
Z	compressibility factor
<i>Greek letters</i>	
α	reduced Helmholtz free energy, a
β	Verschaffelt exponent
ϵ	static dielectric constant
δ	reduced density, $\delta = \rho/\rho_c$
τ	inversely reduced temperature, $\tau = T_c/T$
κ	compressibility
θ	reduced temperature, $\theta = 1-T/T_c$
χ^2	chi-squared
ρ	density
ρ_d	reduced diameter
ρ_{lv}	reduced order parameter

Superscripts

$^{\circ}$	ideal
r	residual
$'$	saturated liquid
$''$	saturated vapour
MAX	maximum

Subscripts

c	critical point value
d	diameter
eff	effective
l	liquid
RF	reaction field
T	isothermal
v	vapour

Chapter 6

a, b	Fourier coefficients
C	Average cross-section tracer concentration (mol m^{-3})
d	Tube diameter (m)
D_a	Axial dispersion coefficient ($\text{m}^2 \text{s}^{-1}$)
f	Fraction of the total tracer concentration (dimensionless)
$h(s)$	Transfer function
$I'(t)$	Normalized concentration of an injected tracer at the inlet
$I(s)$	Laplace transform of $I'(t)$
k'	Pseudo-first order rate constant (s^{-1})
L	Characteristic length (m)
L	Laplace transform
P	Pressure (Pa)
$P'(t)$	Normalized tracer pulse function

$p(s)$	Laplace transform of $P'(t)$
Pe	Péclet number, $Pe = uL/D_a$ (dimensionless)
$R'(t), R'_1(t), R'_2(t)$	Normalized concentration of an injected tracer at the outlet
$r(s), r_1(s), r_2(s)$	Laplace transforms of $R(t), R'_1(t), R'_2(t)$, respectively
Re	Reynolds number, $Re = \rho u d/\mu$ (dimensionless)
s	Laplace domain variable (s^{-1})
T	Temperature (K)
t	Time (s)
\bar{u}_0	Cross-Section Averaged Axial fluid velocity ($m\ s^{-1}$)
x	Axial coordinate (m)

Greek symbols

$\bar{\tau}$	Mean residence time (s)
μ	Dynamic fluid viscosity (Pa s)
ρ	Fluid density ($kg\ m^{-3}$)

Abbreviations

ADPF	Axially dispersed plug flow
ppm	Parts per million ($1\ ppm = 1\ g\ m^{-3}$)
RMS	Root mean square error (%)
RTD	Residence time distribution
SCWO	Supercritical water oxidation

Subscripts

ave.	Average
exptl.	Experimental
mom.	Moment analysis
pred.	Predicted (modeled)

Chapter 7

C	Average cross-section solute concentration (mol m^{-3})
d_0	Inner tube diameter (m)
D_{12}	Binary diffusion coefficient ($\text{m}^2 \text{s}^{-1}$)
D_a	Axial dispersion coefficient ($\text{m}^2 \text{s}^{-1}$)
D_c	Coil diameter (m)
De	Dean number, $De = Re \cdot \omega^{-0.5}$ (dimensionless)
$h(s), h_A(s), h_D(s), h^{\text{ADPF}}(s)$	Transfer functions
$I'(t)$	Normalized impulse curve
$i(s)$	Laplace transform of $I'(t)$
L	Characteristic length (m)
\mathcal{L}	Laplace transform
P	Pressure (Pa)
$P'(t)$	Normalized pulse function
$p(s)$	Laplace transform of $P'(t)$
Pe	Péclet number, $Pe = uL/D_a$ (dimensionless)
q	Partial atomic charge (e)
r	Bond length (Å)
$R'(t), R'_1(t), R'_2(t)$	Normalized response curves
$r(s), r_1(s), r_2(s)$	Laplace transforms of $R(t), R'_1(t), R'_2(t)$, respectively
Re	Reynolds number, $Re = \rho u d/\mu$ (dimensionless)
s	Laplace domain variable (s^{-1})
Sc	Schmidt number, $Sc = \eta/\rho D_{12}$ (dimensionless)
T	Temperature (K)
t	Time (s)
\bar{u}_0	Average cross-section fluid velocity (m s^{-1})
x	Axial coordinate (m)

Greek symbols

$\bar{\tau}$	Mean residence time (s)
μ	Dynamic fluid viscosity (Pa s)
ω	Coil ratio, $\omega = D_c / d_0$
ε	Lennard-Jones interaction parameter (kJ mol^{-1})
σ	Lennard-Jones interaction parameter (\AA)
ρ	Fluid density (kg m^{-3})

Abbreviations

ADPF	Axially dispersed plug flow
MD	Molecular dynamics
<i>NPT</i>	Constant pressure and temperature
<i>NVT</i>	Constant density and temperature
ppm	Parts per million
<i>RMS</i>	Root mean square error (%)
SPC/E	Simple Point Charge Extended

Subscripts

exptl.	Experimental
simul.	Simulated

Chapter 1

Introduction

Water is a unique chemical compound that plays a key role in a variety of biological and geological processes. Its abundance and outstanding properties as a solvent have also made water an essential part of numerous technological applications.

Aqueous fluids at high temperatures and pressures have attracted growing attention over the last two decades.¹⁻²¹ At ambient temperature and pressure water exists in two states, gas and liquid (see Fig. 1.1) with the corresponding densities at saturation being about 1.85×10^{-5} and 0.997 g/cm^3 , respectively. As temperature increases, the density of saturated vapour increases (due to higher compression), whereas the liquid density decreases (due to thermal expansion), see Fig. 1.2. At the critical point ($T_c = 647.096 \text{ K}$, $\rho_c = 0.322 \text{ g/cm}^3$ and $p_c = 22.064 \text{ MPa}$)²² the difference between the densities of the gas and liquid phases disappears. Supercritical water (i.e. water above T_c) can be compressed from gas-like to liquid-like densities without going through a phase transition. The properties of water near its critical point are drastically different from those at ambient conditions. Unlike ambient water which has low compressibility, high viscosity and is an outstanding solvent for electrolytes, near-critical water is highly compressible and expandable, low in viscosity and has a low dielectric constant. High isothermal compressibility and volume expansivity of water in the near-critical region allow for significant changes in density (and subsequently some other thermophysical properties) to be achieved with small changes in temperature and/or pressure. For instance, the compressibility of supercritical water at $T = T_c + 1\text{K}$ and $\rho = \rho_c$ is four orders of magnitude larger than that of liquid water at ambient conditions, see Fig. 1.3.

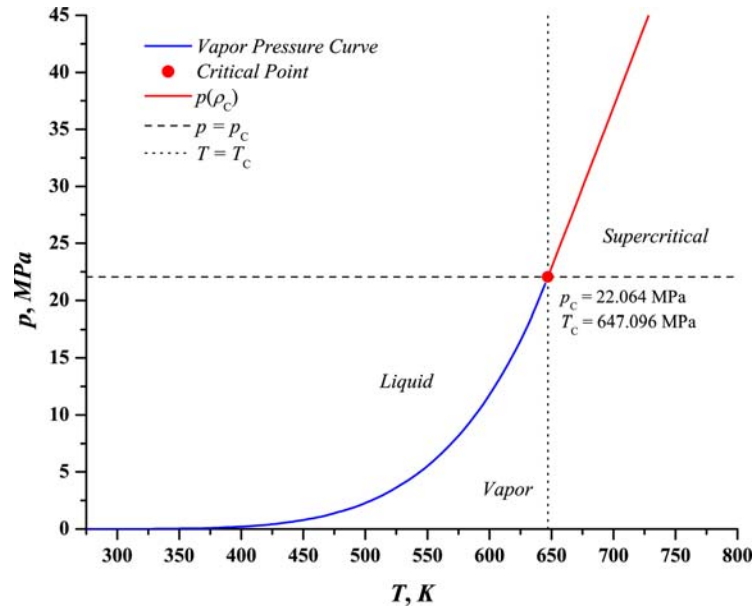


Figure 1.1 Pressure-temperature diagram of water.²³

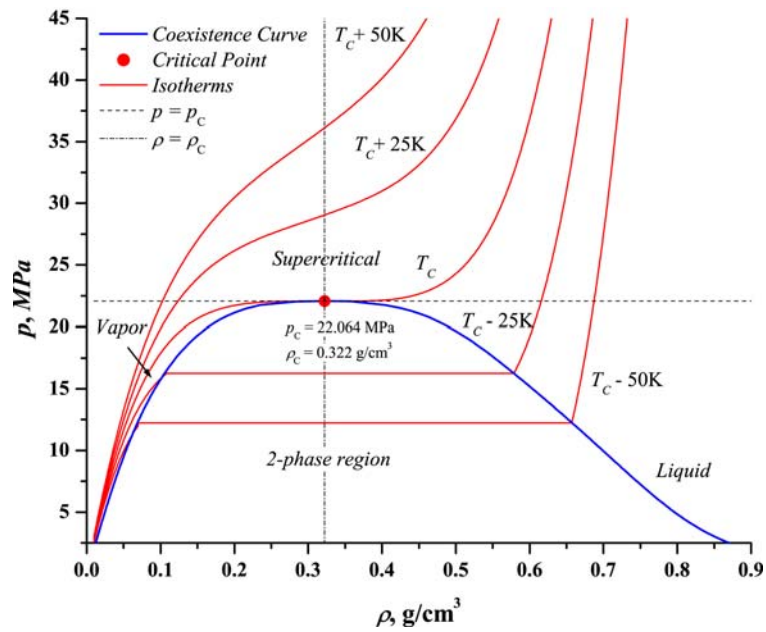


Figure 1.2 Pressure-density diagram of water.²³

Perhaps, the most remarkable and important is the change in character of water as a solvent at elevated temperatures and pressures. The behaviour of the dielectric constant of water is shown in Fig. 1.4. Near and above its critical point water acts as a low polarity fluid becoming a poor solvent for electrolytes. This phenomenon underlies geological processes of mineral formation and deposition in the deep earth and at seafloor hydrothermal vents.

Numerous experimental and theoretical studies have been conducted in order to better understand molecular-level origins of the unique behaviour of high-temperature and supercritical water, see Refs. [1-10, 21, 24-27] and therein. At ambient conditions liquid water forms a three-dimensional network of hydrogen (H-) bonds where each water molecule participates in the formation of four H-bonds. Preferred dipole orientations in the liquid water structure result in an unusually large dielectric constant of about 80 at 298 K. The average number of H-bonds per water molecule decreases with increasing temperature and decreasing density from about four at ambient conditions to less than one above the critical point. The three-dimensional network of H-bonded water molecules begins to break around 473 K and completely disappears above the critical point.^{2,6} It is worth mentioning that H-bonding still persists in dense supercritical water with the H-bonded configurations represented by small water clusters.^{5,8,9,11} These changes in water structure are reflected in the behaviour of the dielectric constant of water which rapidly decreases along the saturated liquid curve as density (and the extent of H-bonding) decreases, and reaches a value of about $\epsilon_c = 5.36^{28}$ at the critical point, see Fig. 1.4.

Near and above its critical point water also exhibits excellent transport properties. The viscosity of dense supercritical water is about ten times smaller than that at ambient conditions.¹² Subsequently, molecular mobilities rise dramatically as the critical point is approached and exceeded. The temperature and pressure dependence of water diffusivity has been studied by a number of research groups.^{27,29-36} The self-diffusion coefficient of water increases from about 2.3

$\times 10^{-9} \text{ m}^2/\text{s}$ at ambient conditions to approximately $90 \times 10^{-9} \text{ m}^2/\text{s}$ at the critical point.³⁵ Noteworthy, the substantial increase in diffusivity of water is observed around 523 K at saturation which coincides with the onset of the disruption of the spatial H-bonded structure of liquid water. It is worth mentioning that the simplistic hydrodynamic (Stokes-Einstein type) equations, commonly used for the calculation of the mass transport coefficients at moderate conditions, fail to adequately describe the behaviour of the self-diffusion coefficient of water at, near, and above its critical point.^{32, 35} This observation significantly undermines the ability to predict diffusivity of solutes based on bulk viscosity values of high-temperature and supercritical water.

The unique properties of supercritical water form a basis for the development of innovative hydrothermal technologies. Enhanced mass transfer and the ability of near-critical water to mix with gases and non-polar organic compounds makes it a very promising medium for a number of environmentally friendly technological applications, such as Supercritical Water Extraction¹⁶ and Supercritical Water Oxidation^{15,19,37} as well as for chemical processing.^{18,20,38-40} The most important technological application of water is in power generation. The need to meet the world's future energy demands has led to international efforts to develop a new generation of nuclear energy systems (GEN IV). One of the selected designs is the Supercritical-Water-Cooled-Reactor (SCWR). The SCWR concept features a combined power cycle which utilizes supercritical water both as a coolant and as a working fluid which results in considerable plant simplification. Increased thermal conductivity combined with the high heat capacity of supercritical water are expected to boost thermal efficiency of SCWRs to approximately 44% compared to about 33% for current Light Water Reactors (LWRs).⁴¹

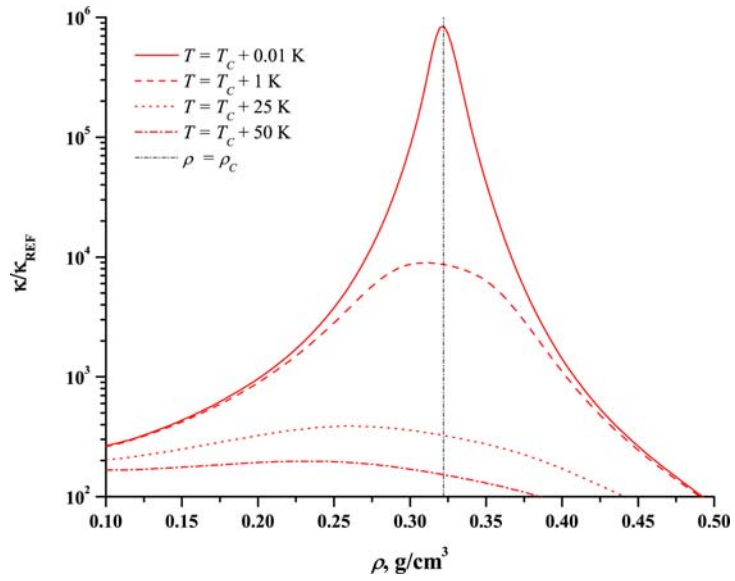


Figure 1.3 Isothermal compressibility $\kappa_T = \rho^{-1}(\partial \rho / \partial p)_T$ of supercritical water.²³ The value $\kappa_T^{\text{REF}} = 0.000453 \text{ MPa}^{-1}$ for the saturated liquid at 298.15 K was used as a reference.

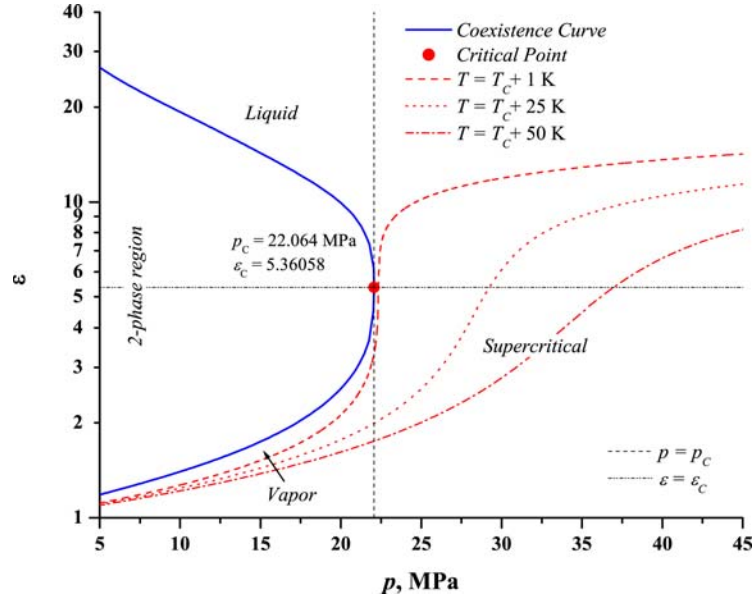


Figure 1.4 Dielectric constant of water.²⁸

1.1 Rationale

The properties of pure water have been carefully evaluated and standardized over a wide range of high-temperature and supercritical states by the International Association for the Properties of Water and Steam (IAPWS). However, the behaviour and reactivity of supercritical aqueous solutions remains poorly understood. From a technological perspective, the design and optimization of industrial processes where supercritical water is used as a solvent, a reaction medium or a working fluid, requires thorough examination of the complex properties of aqueous fluids near and above the critical point.

Nowadays, computer simulations provide valuable data about the properties of hydrothermal fluids. Considering the technical difficulties in conducting physical measurements at sub- and supercritical water conditions, molecular simulations will arguably remain the major source of information in the future. In this respect, the standardization of the properties of model systems over a wide range of high-temperature and supercritical states of water is of great practical importance. Unfortunately, despite the large number of computer simulation studies carried out for water, an accurate continuous description of its thermophysical properties is still lacking for any of the intermolecular potentials currently in use.

From a reaction kinetics perspective, elucidation of mass-transfer coefficients of solutes at near and above the critical point of water is very important for estimation of the reactions rates and in the development of predictive kinetics models. Furthermore, several recent kinetics studies⁴²⁻⁴⁸ seem to indicate that changes in H-bonding and the disappearance of the “cage” effect in particular, may cause a non-Arrhenius behaviour in the rate constants (with negative temperature dependence) for the near-diffusion controlled reactions in the range from about 423 to 623 K. Therefore, systematic studies of hydration structures and dynamics of solutes are

clearly warranted to provide a better understanding of the chemistry in water at near-critical conditions.

The need for additional experimental data on mass-transfer coefficients of solutes and validation of the molecular simulations results necessitates the development of simple experimental methods for molecular diffusivity measurements in near-critical water. From a chemical engineering standpoint, development of sampling techniques for the examination of hydrodynamic performance of chemical reactors under supercritical water conditions is essential for obtaining reliable and reproducible kinetics data.

1.2 Objectives

The objectives of this thesis are the following:

1. Examine the spatial hydration structures and molecular diffusivity of select organic compounds from ambient to supercritical water conditions by means of Molecular Dynamics (MD) simulation.
2. Provide continuous description of the thermodynamic and dielectric properties of the Simple Point Charge Extended water model over a wide range of high-temperature and supercritical states.
3. Construct an experimental flow-through apparatus for the study of hydrothermal systems.
4. Develop a flow-injection methodology for the examination of fluids at extreme conditions.
5. Examine the hydrodynamic performance of flow-through chemical reactors under supercritical water conditions.
6. Develop an experimental technique for the evaluation of the binary diffusion coefficients in high-temperature and supercritical water.

1.3 Thesis Outline

Theoretical and experimental methods are described in Chapter 2. MD simulations of naphthalene and aniline are presented in Chapters 3 and 4, respectively. The thermodynamic and dielectric equations of state for high-temperature SPC/E water are given in Chapter 5. The experimental hydrothermal reactor system and the *ex situ* flow injection methodology for the examination of the hydrodynamic performance of flow-through supercritical water reactors are described in Chapter 6. Application of the *ex situ* Taylor dispersion technique to measurements of the binary diffusion coefficients in high-temperature and supercritical water is discussed in Chapter 7. Summary and future outlook are given in Chapter 8.

1.4 References for Chapter 1

1. P. Postorino, R. H. Tromp, M. A. Ricci, A. K. Soper and G. W. Neilson, *Nature* **366** (6456), 668 (1993).
2. Y. Guissani and B. Guillot, *J. Chem. Phys.* **98** (10), 8221 (1993).
3. Y. E. Gorbaty and A. G. Kalinichev, *J. Phys.Chem.* **99** (15), 5336 (1995).
4. A. K. Soper, F. Bruni and M. A. Ricci, *J. Chem. Phys.* **106** (1), 247 (1997).
5. A. Botti, F. Bruni, M. A. Ricci and A. K. Soper, *J. Chem. Phys.* **109** (8), 3180 (1998).
6. P. Jedlovszky, J. P. Brodholt, F. Bruni, M. A. Ricci, A. K. Soper and R. Vallauri, *J. Chem. Phys.* **108** (20), 8528 (1998).
7. Y. E. Gorbaty and R. B. Gupta, *Ind. Eng. Chem. Res.* **37** (8), 3026 (1998).
8. Y. E. Gorbaty, G. V. Bondarenko, A. G. Kalinichev and A. V. Okhulkov, *Mol. Phys.* **96** (11), 1659 (1999).
9. A. A. Chialvo and P. T. Cummings, *Adv. Chem. Phys.* **109**, 115 (1999).
10. A. K. Soper, *Chem. Phys.* **258** (2-3), 121 (2000).
11. A. G. Kalinichev, *Molecular Modeling Theory: Applications in the Geosciences* **42**, 83 (2001).
12. D. A. Palmer, R. Fernandez-Prini and A. H. Harvey Eds., *Aqueous Systems at Elevated Temperatures and Pressures*, Elsevier, Academic Press, 2004.
13. H. Weingartner and E. U. Franck, *Angew.Chem.-Int.Edit.* **44** (18), 2672 (2005).

14. G. V. Bondarenko, Y. E. Gorbaty, A. V. Okhulkov and A. G. Kalinichev, *J. Phys. Chem. A* **110**(11), 4042 (2006).
15. M. D. Bermejo and M. J. Cocero, *AIChE J.* **52** (11), 3933 (2006).
16. J. Kronholm, K. Hartonen and M. Riekkola, *Trac-Trends Anal. Chem.* **26** (5), 396 (2007).
17. K. Byrappa and T. Adschiri, *Prog. Cryst. Growth Charact. Mater.* **53** (2), 117 (2007).
18. A. Kruse and E. Dinjus, *J. Supercrit. Fluids* **39** (3), 362 (2007).
19. A. Kruse and E. Dinjus, *J. Supercrit. Fluids* **41** (3), 361 (2007).
20. A. Kruse and H. Vogel, *Chem. Eng. Technol.* **31** (9), 1241 (2008).
21. M. Bernabei, A. Botti, F. Bruni, M. A. Ricci and A. K. Soper, *Phys. Rev. E* **78** (2), 021505 (2008).
22. W. Wagner and A. Pruss, *J. Phys. Chem. Ref. Data* **31** (2), 387 (2002).
23. O. Kunz, R. Klimeck, W. Wagner and M. Jaeschke, "The GERG-2004 wide-range equation of state for natural gases and other mixtures." GERG Technical Monograph 15, (2007).
24. T. Tassaing, M. C. Bellissent-Funel, B. Guillot and Y. Guissani, *Europhys. Lett.* **42** (3), 265 (1998).
25. A. G. Kalinichev, Y. E. Gorbaty and A. V. Okhulkov, *J. Molec. Liquids* **82** (1-2), 57 (1999).
26. M. C. Bellissent-Funel, *J. Molec. Liquids* **90** (1-3), 313 (2001).
27. I. A. Beta, J. C. Li and M. C. Bellissent-Funel, *Chem. Phys.* **292** (2-3), 229 (2003).
28. D. P. Fernandez, A. R. H. Goodwin, Eric W. Lemmon, J. M. H. Levelt Sengers and R. C. Williams, *J. Phys. Chem. Ref. Data* **26** (4), 1125 (1997).
29. R. Hausser, G. Maier and F. Noack, *Z. Naturforschung. Teil A* **21** (9), 1410 (1966).

30. K. Krynicki, C. D. Green and D. W. Sawyer, *Faraday Discuss.* **66** (66), 199 (1978).
31. K. R. Harris and L. A. Woolf, *-Faraday Trans.* **76**, 377 (1980).
32. W. J. Lamb, G. A. Hoffman and J. Jonas, *J. Chem. Phys.* **74** (12), 6875 (1981).
33. H. Weingartner, *Zeitschrift Fur Physikalische Chemie-Wiesbaden* **132** (2), 129 (1982).
34. M. Holz, S. R. Heil and A. Sacco, *Phys. Chem. Chem. Phys.* **2** (20), 4740 (2000).
35. K. Yoshida, C. Wakai, N. Matubayasi and M. Nakahara, *J. Chem. Phys.* **123** (16), 164506 (2005).
36. K. Yoshida, N. Matubayasi and M. Nakahara, *J. Chem. Phys.* **125** (7), 074307 (2006).
37. V. Barribang and K. Jae-Duck, *J. Environ. Sci.-China* **19** (5), 513 (2007).
38. P. E. Savage, *Chem.Rev.* **99** (2), 603 (1999).
39. F. Vogel, J. L. D. Blanchard, P. A. Marrone, S. F. Rice, P. A. Webley, W. A. Peters, K. A. Smith and J. W. Tester, *J. Supercrit. Fluids* **34** (3), 249 (2005).
40. Y. Matsumura, T. Minowa, B. Potic, S. R. A. Kersten, W. Prins, W. P. M. van Swaaij, B. van de Beld, D. C. Elliott, G. G. Neuenschwander, A. Kruse and M. J. Antal, *Biomass Bioenerg.* **29** (4), 269 (2005).
41. Ph. MacDonald, J. Buongiorno, J. W. Sterbentz, C. Davis and R. Witt, "*Feasibility Study of Supercritical Light Water Cooled Reactors for Electric Power Production*", Nuclear Energy Research Initiative Project 2001-001 INEEL/EXT-04-02530.
42. I. Janik, D.M. Bartels and C.D. Jonah, *J. Phys. Chem. A* **111** (10), 1835 (2007).
43. K. Takahashi, D. M. Bartels, J. A. Cline and C. D. Jonah, *Chem..Phys.Lett.* **357** (5-6), 358 (2002).

44. T. W. Marin, J. A. Cline, K. Takahashi, D. M. Bartels and C. D. Jonah, *J. Phys. Chem. A* **106** (51), 12270 (2002).
45. J. Cline, K. Takahashi, T. W. Marin, C. D. Jonah and D. M. Bartels, *J. Phys. Chem. A* **106** (51), 12260 (2002).
46. J. Bonin, I. Janik, D. Janik and D. M. Bartels, *J. Phys. Chem. A* **111** (10), 1869 (2007).
47. K. Ghandi, B. Addison-Jones, J. C. Brodovitch, I. McKenzie, P. W. Percival and J. Schuth, *Phys. Chem. Chem. Phys.* **4** (4), 586 (2002).
48. K. Ghandi and P. W. Percival, *J. Phys. Chem. A* **107** (17), 3005 (2003).

Chapter 2

Theoretical and Experimental Methods

2.1 Molecular Dynamics Simulations

Computer simulations have become an essential part of modern physical chemistry. Molecular simulation methods provide information about the thermodynamic, transport and structural properties of a model system. The main advantage of computer simulations is the ability to gain insights into the microscopic molecular-level origin of the macroscopic phenomena. Computer simulations are particularly valuable for the examination of system properties under extreme conditions, where physical experiments are difficult or impossible to perform.

Monte Carlo and Molecular Dynamics simulations are the two commonly used classical statistical mechanics methods. The Monte Carlo (MC) technique, in its simplest implementation, is based on a random displacement of a particle in the system. The acceptance or rejection of a random move depends on the transition probability, which is chosen to produce system averages in a particular ensemble.¹ Although MC is a very fast and efficient method for sampling the configuration space it does not provide any information about the dynamics.

The time-dependent properties of a model system can be obtained by using the molecular dynamics (MD) simulation method. The MD simulation technique is based on the solution of the Newtonian equations of motion. In this chapter, basic theory, key simulation techniques and selected water models are described.

2.1.1 General Principles

The essence of the MD simulation is the solution of the classical equations of motion which define the relationship between forces acting on a particle and the motion of the particle:

$$\mathbf{f}_i = m_i \mathbf{a}_i = m_i \frac{d \mathbf{v}_i}{dt} = m_i \frac{d^2 \mathbf{r}_i}{dt^2}, \quad (2.1)$$

where \mathbf{f} is the force, m is the mass of the particle, t is time and \mathbf{a} , \mathbf{v} and \mathbf{r} are the acceleration, velocity and position of the particle i , respectively. For an N atom 3D system the propagation of particles trajectories by one time step involves the solution of a system of either $3N$ second-order, or a corresponding set of $6N$ first-order, differential equations. The solution of the equations of motion requires calculation of the force acting on each particle. The forces are derived from the potential energy \mathcal{V} :

$$\mathbf{f}_i = -\nabla_{\mathbf{r}_i} \mathcal{V}. \quad (2.2)$$

The potential energy, which defines the energetics of interactions in the system, can be viewed as a sum of contributions arising from one-body, two-body, three-body interactions etc.:

$$\mathcal{V} = \sum_i \mathcal{V}_1(\mathbf{r}_i) + \sum_i \sum_{j>i} \mathcal{V}_2(\mathbf{r}_i, \mathbf{r}_j) + \sum_i \sum_{j>i} \sum_{k>j>i} \mathcal{V}_3(\mathbf{r}_i, \mathbf{r}_j, \mathbf{r}_k) + \dots \quad (2.3)$$

The first term in Eq. 2.3 depends only on the position of the particle and represents the effect of an external field. The second term depends on the magnitude of pair separation $\mathbf{r}_{ij} = |\mathbf{r}_i - \mathbf{r}_j|$ and contributes the most (in absence of the external field) to the total potential energy. Calculation of the interactions between triplets is computationally very expensive and typically the sum in Eq. 2.3 is truncated at the second term. The contributions to potential energy due to triplets and higher terms are included in the “effective” pair-potential:

$$\mathcal{V} \approx \sum_i \mathcal{V}_1(\mathbf{r}_i) + \sum_i \sum_{j>i} \mathcal{V}_2^{\text{eff}}(\mathbf{r}_{ij}). \quad (2.4)$$

The effective pair-interaction potential can be split further into the electrostatic and dispersion (van der Waals) interactions. The van der Waals interactions are represented by using continuous (soft-sphere, Mie-type) or discontinuous (hard-sphere, square-well) empirical functions with a few adjustable parameters.^{1,2} The most commonly used form is the Lennard-Jones 12-6 potential:

$$\mathcal{V}^{\text{LJ}}(\mathbf{r}_{ij}) = 4\epsilon_{ij} \left[\left(\frac{\sigma_{ij}}{\mathbf{r}_{ij}} \right)^{12} - \left(\frac{\sigma_{ij}}{\mathbf{r}_{ij}} \right)^6 \right], \quad (2.5)$$

where the two empirical parameters σ and ϵ are the diameter and the depth of the potential well, respectively. Interactions between unlike atoms are approximated by using the Lorentz-Berthelot mixing rules, $\sigma_{ij} = (\sigma_i + \sigma_j)/2$ and $\epsilon_{ij} = \sqrt{\epsilon_i \epsilon_j}$.

Electrostatic interactions are treated by considering an appropriate Coulomb potential:

$$\mathcal{V}^{\text{C}}(\mathbf{r}_{ij}) = \frac{q_i q_j}{4\pi\epsilon_0 \mathbf{r}_{ij}}, \quad (2.6)$$

where q_i and q_j are the charges on the sites i and j and ϵ_0 is the permittivity of free space.

Thus, the total potential energy for an atomic system in the absence of an external field is given by:

$$\begin{aligned} \mathcal{V}_{\text{tot}} &= \sum_i \sum_{j>i} \mathcal{V}_2^{\text{eff}}(\mathbf{r}_{ij}) = \sum_i \sum_{j>i} (\mathcal{V}^{\text{LJ}}(\mathbf{r}_{ij}) + \mathcal{V}^{\text{C}}(\mathbf{r}_{ij})) = \\ &= \sum_i \sum_{j>i} \left(4\epsilon_{ij} \left[\left(\frac{\sigma_{ij}}{\mathbf{r}_{ij}} \right)^{12} - \left(\frac{\sigma_{ij}}{\mathbf{r}_{ij}} \right)^6 \right] + \frac{q_i q_j}{4\pi\epsilon_0 \mathbf{r}_{ij}} \right). \end{aligned} \quad (2.7)$$

Note that interaction between a pair of rigid molecules, which is a rather complex function of the relative positions ($\mathbf{r}_i, \mathbf{r}_j$) and orientations ($\mathbf{\Omega}_i, \mathbf{\Omega}_j$), is modeled by using the so-called

“*site-site*” approximation, where the total interaction is represented by a sum of pairwise contributions from distinct sites a and b of molecules i and j :

$$\mathcal{V}(\mathbf{r}_{ij}, \mathbf{\Omega}_i, \mathbf{\Omega}_j) = \sum_a \sum_b \mathcal{V}_{ab}(\mathbf{r}_{ab}), \quad (2.8)$$

where $\mathbf{r}_{ab} = |\mathbf{r}_{ia} - \mathbf{r}_{jb}|$ is the inter-site separation.

2.1.2 Molecular Dynamics Simulation Techniques

2.1.2.1 Periodic Boundary Conditions

Simulation of the bulk properties of a substance represented by a small number of model particles (10^2 - 10^4) is performed by using periodic boundary conditions (PBC). In PBC the central simulation box is surrounded by its periodic replicas. During the simulation a particle leaving the central box is replaced by its periodic image entering the central box from an opposite direction, Fig. 2.1. Note that such a representation of a macroscopic system imposes artificial periodicity, and, thus, does not allow capturing long-wavelength (wavelengths greater than a box length) fluctuations. Generally for system sizes above 256 particles PBC have little effect on the equilibrium thermodynamic and structural properties of a model system.^{1,2}

For simplicity the geometry of a primary simulation cell is typically chosen to be a cubic box. Other geometries include the rhombic dodecahedron and the truncated octahedron, which are closer to the spherical shape, and therefore are more efficient for representing a spatially isotropic system.¹

2.1.2.2 Potential Truncation

The calculation of the potential energy of a system subject to PBC requires the calculation of all interactions of a given particle with all other particles in the primary and periodic simulation boxes, which creates an enormous computational task. However, taking into consideration the fact that the largest contribution to the potential energy arises from interactions between nearest neighbours, the short-range interactions are calculated by applying the “minimum image convention” approximation. In the minimum image (MI) convention the position of a particle is viewed to be at the center of a simulation box such that it interacts with its $N-1$ nearest neighbours only. A further approximation in handling the short-range forces involves application of a spherical cutoff, where interactions of a particle with its neighbours are calculated explicitly only within a spherical cut-off distance r_{cut} (typically half of the cubic simulation box length), Fig. 2.1.

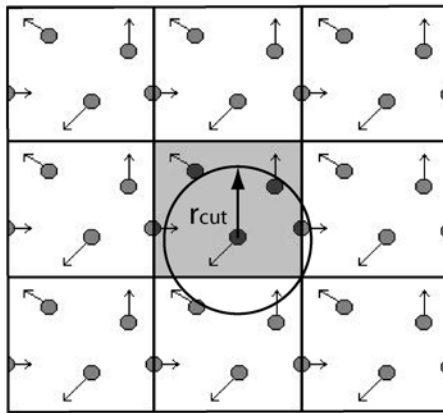


Figure 2.1 Schematic diagram of periodic boundary conditions.

To minimize the effect of potential truncation on the properties of the system, appropriate long-range interaction corrections (beyond r_{cut}) to the potential energy and virial should be applied by adding an analytical correction “tail” terms, e.g.:

$$\mathcal{V}_{\text{tot}}^{\text{LJ}} = \sum_{i < j} \mathcal{V}_{\text{cut}}^{\text{LJ}}(\mathbf{r}_{ij}) + \mathcal{V}_{\text{tail}}^{\text{LJ}}(r_{\text{cut}}), \quad (2.9)$$

where \mathcal{V}_{cut} is the truncated LJ potential and $\mathcal{V}_{\text{tail}}$ is the long-range potential energy correction term.

For two atom types a and b , the correction to the potential energy is given by:

$$\mathcal{V}_{\text{ab,tail}}^{\text{LJ}}(r_{\text{cut}}) = 2\pi \frac{N_a N_b}{V} \int_{r_{\text{cut}}}^{\infty} g_{\text{ab}}(r) \cdot \mathcal{V}_{\text{ab}}^{\text{LJ}}(r) \cdot r^2 dr, \quad (2.10)$$

where N_a and N_b are the number of atoms of types a and b , V is the volume of the system, and $g_{\text{ab}}(r)$ and $\mathcal{V}_{\text{ab}}(r)$ are the pair-correlation function and pair-potential, respectively. The $g_{\text{ab}}(r)$ is typically taken to be unity at $r > r_{\text{cut}}$.

An analytical tail correction can only be applied for rapidly decaying interaction potentials (more than r^{-3}). Accurate calculation of the long-ranged electrostatic interactions requires other methods. The two widely accepted approaches are the Ewald summation technique and the reaction field (RF) method. Both methods consider a system surrounded by a dielectric continuum with a dielectric constant ϵ_{RF} . In the RF method the electrostatic interactions beyond the cut-off distance r_{cut} are treated by using macroscopic electrostatics, where the surrounding dielectric creates a reaction field within a spherical cavity of radius r_{cut} .¹ In contrast with the RF approach, the Ewald summation technique explicitly considers the electrostatic interactions within a much bigger (macroscopic) system made of a large number of periodic replicas of the primary simulation box. In this thesis the long-range Coulomb interactions were handled by using the Ewald summation technique.

2.1.2.3 Ewald Summation Method

The Coulomb contribution to the potential energy of a system due to point charges can be expressed as¹:

$$\mathcal{V}^C(\mathbf{r}_{ij}) = \sum_{\mathbf{n}} \left(\sum_{\substack{i,j \\ i < j}} \frac{q_i q_j}{|\mathbf{r}_{ij} + \mathbf{n}|} \right), \quad (2.11)$$

where the sum over \mathbf{n} is taken over all simple cubic lattice points, $\mathbf{n} = L(k, l, m)$, L is the length of the simulation box and k , l and m are integers. The prime indicates the exclusion of the $i = j$ term for $\mathbf{n} = 0$. Note, that Eq. 2.11 is written in reduced units of charge. The lattice sum in Eq. 2.11 is only conditionally convergent. To improve the convergence, the electrostatic potential energy is viewed as a sum of charge densities. Each point charge is surrounded by a diffuse charge distribution of equal magnitude and opposite sign, so that the interactions between neighbouring point charges are screened. The form of the distribution is taken to be Gaussian:

$$\rho_i^q(\mathbf{r}) = \frac{q_i \alpha^3}{\pi^{3/2}} \exp(-\alpha^2 r^2), \quad (2.12)$$

where α determines the width of the distribution, and \mathbf{r} is the position relative to the center of the distribution. The electrostatic potential due to the screened charges is a rapidly decaying function of \mathbf{r} and therefore can be calculated by a direct summation in real space. In order to obtain the potential due to the original point charges, a cancelling distribution is added to compensate for the effect of the screening distribution. It is necessary to add the cancelling distribution to the original point charge centered at \mathbf{r}_j . In this case the electrostatic potential energy becomes a smoothly varying periodic function, which can be evaluated in the Fourier space. The final result is then corrected for the presence of the extra self-term, Fig. 2.2.

The Coulomb energy for the system of point charges in cubic periodic boundary conditions is given by¹:

$$\mathcal{V}^C(\epsilon_{\text{RF}} = \infty) = \sum_{\substack{i,j \\ i < j}} \left(\sum_{\mathbf{n}}' q_i q_j \frac{\text{erfc}(\alpha|\mathbf{r} + \mathbf{n}|)}{|\mathbf{r} + \mathbf{n}|} + \frac{1}{\pi L^3} \sum_{\mathbf{k} \neq 0} q_i q_j \frac{4\pi^2}{k^2} \exp\left(-\frac{k^2}{4\alpha^2}\right) \cos(\mathbf{k} \cdot \mathbf{r}) \right) - \frac{\alpha}{\pi^{1/2}} \sum_i q_i^2, \quad (2.13)$$

in which

$$\text{erfc}(x) = \frac{2}{\pi^{1/2}} \int_x^\infty \exp(-t^2) dt \quad (2.14)$$

is the complementary error function and $\mathbf{k} = 2\pi\mathbf{n}/L^2$.

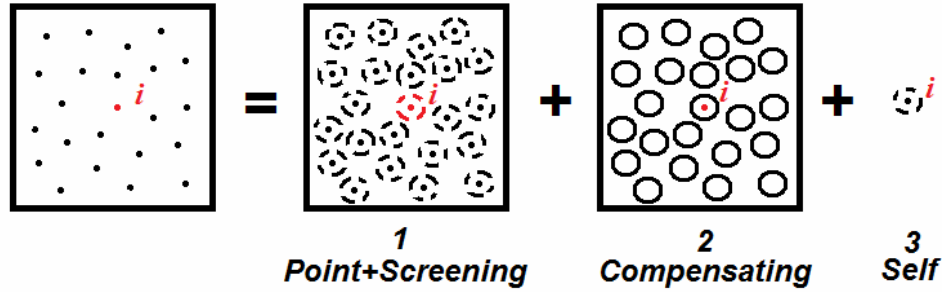


Figure 2.2 Schematic representation of point charges in the Ewald summation technique.

The accuracy in the calculation of the electrostatic interactions by using the Ewald approach depends on the value of the convergence parameter α and the truncation of the real and Fourier space sums. Traditionally, the real space sum is truncated at $\mathbf{n} = 0$, which reduces electrostatic energy calculations to the minimum image convention approximation, and, thus, significantly reduces the cost of the calculations. The convergence parameter α and the number of the reciprocal lattice vectors \mathbf{n} are chosen to minimize the error in estimation of the electrostatic energy.^{1,3} In this thesis the real space part of the Ewald sums was calculated by using the

spherical truncation with $r_{\text{cut}} = L/2$. The convergence parameter α was set at $5/L$. The number of the reciprocal lattice vectors (typically $n_{\text{MAX}}^2 \leq 30 - 32$) was chosen to maintain the relative error in the calculation the electrostatic potential energy below 0.005%.

The result in Eq. 2.13 corresponds to a macroscopic spherical sample surrounded by a conducting medium with dielectric constant $\epsilon_{\text{RF}} = \infty$, so called “tin-foil” boundary conditions. For the examination of the dielectric properties of the system, it is advantageous to use a reaction field dielectric constant ϵ_{RF} similar to that of bulk medium.^{3,4} The “surface” correction term is⁵:

$$\mathcal{V}^{\text{RF}} = \mathcal{V}^{\text{C}}(\epsilon_{\text{RF}}) - \mathcal{V}^{\text{C}}(\epsilon_{\text{RF}} = \infty) = \frac{2\pi}{(2\epsilon_{\text{RF}} + 1)V} \mathbf{M}^2, \quad (2.15)$$

where \mathbf{M} is the instantaneous total dipole moment of the simulation box of volume V . The total dipole moment is given by:

$$\mathbf{M} = \sum_i \boldsymbol{\mu}_i = \sum_i \sum_{\alpha} q_{i\alpha} \mathbf{d}_{i\alpha}, \quad (2.16)$$

where $\boldsymbol{\mu}_i$ is the molecular dipole, $q_{i\alpha}$ is the partial charge on site α of molecule i and $\mathbf{d}_{i\alpha} = \mathbf{r}_{i\alpha} - \mathbf{r}_i$ is the vector from the center to site α .

2.1.2.4 Rigid Body Rotation

The rotation of a rigid body about the center of mass is governed by the torque, $\boldsymbol{\tau}$. The equations of rotational motion in the body-fixed coordinate system are given by:

$$\begin{aligned} \dot{\omega}_x^{\text{b}} &= \frac{\tau_x^{\text{b}}}{I_{xx}} + \left(\frac{I_{yy} - I_{zz}}{I_{xx}} \right) \omega_y^{\text{b}} \omega_z^{\text{b}} \\ \dot{\omega}_y^{\text{b}} &= \frac{\tau_y^{\text{b}}}{I_{yy}} + \left(\frac{I_{zz} - I_{xx}}{I_{yy}} \right) \omega_x^{\text{b}} \omega_z^{\text{b}} \\ \dot{\omega}_z^{\text{b}} &= \frac{\tau_z^{\text{b}}}{I_{zz}} + \left(\frac{I_{xx} - I_{yy}}{I_{zz}} \right) \omega_y^{\text{b}} \omega_x^{\text{b}} \end{aligned} \quad (2.17)$$

where ω is the angular velocity and I_{xx} , I_{yy} and I_{zz} are the three principal moments of inertia. The torques, however, are most easily evaluated in the space-fixed coordinate system by considering the forces acting on all sites of the molecule:

$$\boldsymbol{\tau}_i^s = \sum_a (\mathbf{r}_{ia} - \mathbf{r}_i) \times \mathbf{f}_{ia} = \sum_a \mathbf{d}_{ia} \times \mathbf{f}_{ia} \quad (2.18)$$

where \mathbf{d}_{ia} are relative positions of atoms to the center of mass of the molecule.

Transformation between space-fixed and body-fixed coordinate systems is performed by using the rotation matrix, \mathbf{A} , which defines the molecular orientation in the space-fixed frame in terms of Euler angles (φ, θ, ψ)

$$\mathbf{A} = \begin{pmatrix} \cos\varphi \cos\psi - \sin\varphi \cos\theta \sin\psi & \sin\varphi \cos\psi + \sin\varphi \cos\theta \sin\psi & \sin\psi \sin\theta \\ -\cos\varphi \sin\psi - \sin\varphi \cos\theta \cos\psi & -\sin\varphi \sin\psi + \cos\varphi \cos\theta \cos\psi & \cos\psi \sin\theta \\ \sin\varphi \sin\theta & -\cos\varphi \sin\theta & \cos\theta \end{pmatrix} \quad (2.19)$$

so that

$$\boldsymbol{\tau}^b = \mathbf{A} \cdot \boldsymbol{\tau}^s \quad (2.20)$$

Unfortunately, the equations of motion for the molecular orientation, expressed in terms of the *three* Euler angles, diverge as θ approaches 0 or π :

$$\begin{aligned} \dot{\varphi} &= -\omega_x^s \frac{\sin\varphi \cos\theta}{\sin\theta} + \omega_y^s \frac{\cos\varphi \cos\theta}{\sin\theta} + \omega_z^s \\ \dot{\theta} &= \omega_x^s \cos\varphi + \omega_y^s \sin\varphi \\ \dot{\psi} &= \omega_x^s \frac{\sin\varphi}{\sin\theta} - \omega_y^s \frac{\cos\varphi}{\sin\theta} \end{aligned} \quad (2.21)$$

The singularity can be avoided if the molecular orientation is expressed by using a set of *four* scalar quantities, a quaternion $\mathbf{Q} \equiv (q_0, q_1, q_2, q_3)$ with $q_0^2 + q_1^2 + q_2^2 + q_3^2 = 1$.⁶ When quaternion parameters are defined as:

$$\begin{aligned} q_0 &= \cos \frac{\theta}{2} \cos \frac{\varphi + \psi}{2} \\ q_1 &= \sin \frac{\theta}{2} \cos \frac{\varphi - \psi}{2} \\ q_2 &= \sin \frac{\theta}{2} \sin \frac{\varphi - \psi}{2} \\ q_3 &= \cos \frac{\theta}{2} \sin \frac{\varphi + \psi}{2} \end{aligned} \quad (2.22)$$

the rotation matrix becomes:

$$\mathbf{A} = \begin{pmatrix} q_0^2 + q_1^2 - q_2^2 - q_3^2 & 2(q_1q_2 + q_0q_3) & 2(q_1q_3 - q_0q_2) \\ 2(q_1q_2 - q_0q_3) & q_0^2 - q_1^2 + q_2^2 - q_3^2 & 2(q_2q_3 + q_0q_1) \\ 2(q_1q_3 + q_0q_2) & 2(q_2q_3 - q_0q_1) & q_0^2 - q_1^2 - q_2^2 + q_3^2 \end{pmatrix}. \quad (2.23)$$

Singularity-free equations of motion for quaternions are given by:

$$\begin{pmatrix} \dot{q}_0 \\ \dot{q}_1 \\ \dot{q}_2 \\ \dot{q}_3 \end{pmatrix} = \frac{1}{2} \begin{pmatrix} q_0 & -q_1 & -q_2 & -q_3 \\ q_1 & q_0 & -q_3 & q_2 \\ q_2 & q_3 & q_0 & -q_1 \\ q_3 & -q_2 & q_1 & q_0 \end{pmatrix} \begin{pmatrix} 0 \\ \omega_x^b \\ \omega_y^b \\ \omega_z^b \end{pmatrix}, \quad (2.24)$$

where ω^b is the angular velocity in the body-fixed coordinate system.

2.1.2.5 Integration of the Equations of Motion

Once the forces acting on each particle have been calculated, the equations of motion can be solved by using the finite difference approach. Among most commonly used integration

schemes are the Verlet and Gear algorithms.^{1,2} In this thesis the equations of motion were integrated using the Gear predictor-corrector algorithm.

The predictor-corrector method is implemented in two stages. First, the positions, velocities, accelerations etc. of particles at time $t+\delta t$ are predicted (without solving equations of motion) by using Taylor expansion around time t :

$$\begin{aligned}
\mathbf{r}^p(t+\delta t) &= \mathbf{r}(t) + \delta t \mathbf{v}(t) + \frac{1}{2} \delta t^2 \mathbf{a}(t) + \frac{1}{6} \delta t^3 \mathbf{b}(t) + \dots \\
\mathbf{v}^p(t+\delta t) &= \mathbf{v}(t) + \delta t \mathbf{a}(t) + \frac{1}{2} \delta t^2 \mathbf{b}(t) + \dots \\
\mathbf{a}^p(t+\delta t) &= \mathbf{a}(t) + \delta t \mathbf{b}(t) + \dots \\
\mathbf{b}^p(t+\delta t) &= \mathbf{b}(t) + \dots \quad ,
\end{aligned} \tag{2.25}$$

where \mathbf{r} , \mathbf{v} , \mathbf{a} and \mathbf{b} are the positions, velocities, accelerations and jerks (the third time derivative of position), respectively. The forces at time $t+\delta t$, obtained by using the predicted positions, are used to estimate the error in the predicted values of accelerations:

$$\Delta \mathbf{a}(t+\delta t) = \mathbf{a}^c(t+\delta t) - \mathbf{a}^p(t+\delta t). \tag{2.26}$$

The error is then used to correct predicted positions, velocities, accelerations etc:

$$\begin{aligned}
\mathbf{r}^c(t+\delta t) &= \mathbf{r}^p(t+\delta t) + c_0 \Delta \mathbf{a}(t+\delta t) \\
\mathbf{v}^c(t+\delta t) &= \mathbf{v}^p(t+\delta t) + c_1 \Delta \mathbf{a}(t+\delta t) \\
\mathbf{a}^c(t+\delta t) &= \mathbf{a}^p(t+\delta t) + c_2 \Delta \mathbf{a}(t+\delta t) \\
\mathbf{b}^c(t+\delta t) &= \mathbf{b}^p(t+\delta t) + c_3 \Delta \mathbf{a}(t+\delta t)
\end{aligned} \tag{2.27}$$

The values of the empirical corrector coefficients depend on the order of the differential equation being solved and the number of position derivatives considered. In this thesis, the fourth-order Gear algorithm was employed.

2.1.2.6 Molecular Dynamics in NVT and NPT Ensembles

The equations of motion, discussed above, generate the system properties in the microcanonical (NVE) ensemble. Simulation of a model system at constant temperature and/or pressure requires modification of the equations of motion. The average system temperature can be maintained at a desired set point by coupling the system to a thermostat (thermal bath), whereas constant pressure simulations require dynamic adjustments of the simulation box size using a barostat. A number of different methods for temperature and pressure control have been developed.^{1,2}

In this study the constant-temperature simulations were performed by using Gaussian thermostat.⁷ The instantaneous kinetic temperature of the system is given by

$$T = \frac{1}{3Nk_B} \sum_{i=1}^N \frac{\mathbf{p}_i^2}{m_i}, \quad (2.28)$$

where T is temperature, \mathbf{p} and m are the momentum and mass of particle i , and k_B is the Boltzmann constant. The equations of motion can be written in such way as to constrain the current kinetic temperature to the desired thermodynamic temperature by using a “friction coefficient” $\xi(\mathbf{r}, \mathbf{p})$:⁷

$$\begin{cases} \dot{\mathbf{r}}_i = \frac{\mathbf{p}_i}{m_i} \\ \dot{\mathbf{p}}_i = \mathbf{f}_i - \xi(\mathbf{r}, \mathbf{p})\mathbf{p}_i \end{cases}, \quad (2.29)$$

with

$$\xi = \frac{\sum_i \mathbf{p}_i \mathbf{f}_i}{\sum_i |\mathbf{p}_i|^2}. \quad (2.30)$$

The Gaussian thermostat generates the trajectories in the isokinetic (NVE_{kin}) ensemble, which differ from the truly canonical averages by $O(1/N)$.¹ In this study, separate thermostats were used to control the translational and rotational temperatures.

MD simulations at constant pressure were carried out by using Andersen barostat, which couples the system's pressure p to the volume of the simulation box V by using a fictional piston of "mass" Q .⁸ The adjustable parameter Q determines the frequency of volume fluctuations. The kinetic and potential energies for the piston are given by:

$$\begin{aligned}\mathcal{K}_V &= \frac{1}{2}Q\dot{V}^2, \\ \mathcal{V}_V &= pV\end{aligned}\tag{2.31}$$

where p is the desired pressure. If the position and velocities of particles are written in reduced units so that $\mathbf{r} = \mathbf{s} \cdot V^{1/3}$ and $\mathbf{v} = \dot{\mathbf{s}} \cdot V^{1/3}$, the equations of motion become:

$$\begin{cases} \ddot{\mathbf{s}} = \frac{\mathbf{f}_i}{m_i V^{1/3}} - \frac{2 \dot{\mathbf{s}} \dot{V}}{3 V} \\ \ddot{V} = \frac{(p - \bar{p})}{Q} \end{cases},\tag{2.32}$$

where p and \bar{p} are the instantaneous and the desired pressure, respectively. The instantaneous pressure of the simulation cell is given by:

$$pV = Nk_B T - \frac{1}{3} \sum_{\substack{i,j \\ i < j}} \mathbf{f}_{ij} \mathbf{r}_{ij}.\tag{2.33}$$

2.1.3 System properties

The aim of computer experiments is to measure certain properties of a model system at given experimental conditions. As in a typical physical experiment it is extremely important to

allow sufficient time for the system to reach equilibrium (or steady-state, in case of non-equilibrium MD) before taking measurements.

2.1.3.1 Thermodynamic Properties

In computer simulations the simple experimentally observable thermodynamic quantities, such as temperature and pressure (Eqs. 2.28 and 2.33), are obtained by averaging instantaneous values $\mathcal{A}(t)$ over the length of the equilibrated trajectory, τ_{run} :

$$\langle \mathcal{A}(t) \rangle_{\text{run}} = \frac{1}{\tau_{\text{run}}} \sum_{\tau_{\text{run}}} \mathcal{A}(t), \quad (2.34)$$

where $\langle \dots \rangle$ denotes ensemble average.

The error in ensemble averages is typically obtained from the analysis of the statistically uncorrelated parts (blocks) of the trajectory:

$$\sigma^2(\mathcal{A}) = \frac{1}{n_{\text{block}}} \sum_{n_{\text{block}}} \left(\langle \mathcal{A}(t) \rangle_{\text{block}} - \langle \mathcal{A}(t) \rangle_{\text{run}} \right)^2, \quad (2.35)$$

where $\sigma^2(\mathcal{A})$ is an estimate of the variance and the block average is given by:

$$\langle \mathcal{A}(t) \rangle_{\text{block}} = \frac{1}{\tau_{\text{block}}} \sum_{\tau_{\text{block}}} \mathcal{A}(t), \quad (2.36)$$

where τ_{block} is the length of the time-block.

2.1.3.2 Structural Properties

The local structure of a fluid can be characterized by a set of distribution functions. The radial distribution function (RDF), or $g(r)$, is the simplest site-site pair distribution function which describes how, on average, the atoms (sites) are radially packed around each other. The RDF is defined as a probability density of finding site j at a certain distance r from site i located at the origin:

$$g(r) = \rho^{-2} \left\langle \sum_i \sum_{j \neq i} \delta(\mathbf{r}_i) \delta(\mathbf{r}_j - \mathbf{r}) \right\rangle = \frac{V}{N^2} \left\langle \sum_i \sum_{j \neq i} \delta(\mathbf{r} - \mathbf{r}_{ij}) \right\rangle. \quad (2.37)$$

The radial distribution functions for the Simple Point Charge Extended⁹ (SPC/E) water model at ambient conditions are shown in Fig. 2.3.

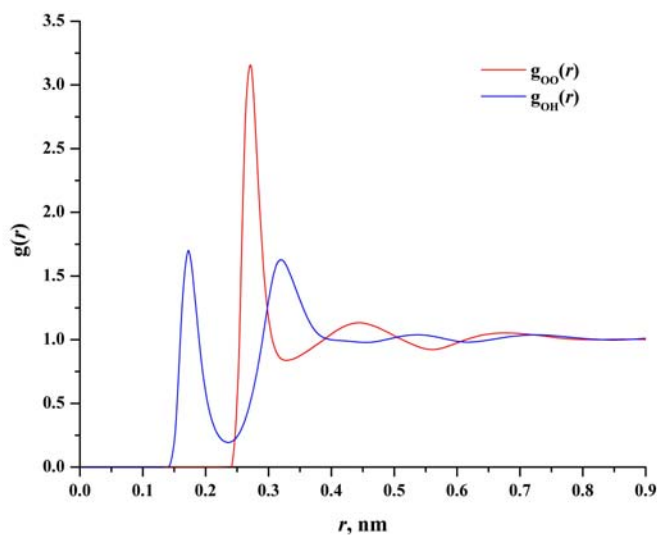


Figure 2.3 The oxygen-oxygen, $g_{OO}(r)$, and oxygen-hydrogen, $g_{OH}(r)$, radial distribution functions of the SPC/E water at ambient conditions.

The information about the position and intensity of peaks in $g(r)$ can be used to deduce the local structure of the fluid. The integration of the RDF yields the coordination number, which gives the average number of neighbours within a certain radial distance. The $g(r)$ is directly related to the experimental structure factors obtained by X-ray and neutron diffraction measurements and, thus, is commonly used to gauge a model potential.

The RDF can fully characterize the structure of an atomic fluid only. An unambiguous elucidation of a local structure in a molecular system requires not only radial but also angular information. The spatial distribution function (SDF), or $g(r, \mathbf{\Omega})$, introduced by Svishchev and Kusalik¹⁰, is the orientationally resolved pair distribution function. The SDF is evaluated in the body-fixed coordinate system of a molecule. In spherical body-fixed coordinate system with $\mathbf{\Omega} \equiv (\theta, \varphi)$ the SDF is given by:

$$g(r, \mathbf{\Omega}) = \frac{I}{\rho \Delta V_{n,m,l}} \left\langle \sum_i \sum_{j \neq i} \delta(\theta_i - \theta_{ij}) \delta(\varphi_m - \varphi_{ij}) \delta(\mathbf{r}_n - \mathbf{r}_{ij}) \right\rangle, \quad (2.38)$$

where

$$\Delta V_{n,m,l} = \frac{1}{3} (\cos \theta_{l-1} - \cos \theta_l) (\varphi_{m-1} - \varphi_m) (\mathbf{r}_n^3 - \mathbf{r}_{n-1}^3) \quad (2.39)$$

and indexes n , l , and m indicate partitioning of the radial and the angular coordinates.

The SDF is typically visualized as an isodensity surface at some probability level, for instance, higher than that of a bulk system. The oxygen-oxygen SDF for the SPC/E water at ambient conditions is shown in Fig. 2.4. This figure clearly illustrates the local tetrahedral structure of water at 298K. The two cups located along the direction of the OH bond of water are due to the H-bond accepting neighbours, whereas the elongated feature below the central oxygen

atom corresponds to the H-bond donating water molecules. The two more distant features are due to the interstitial non-hydrogen bonded neighbours.

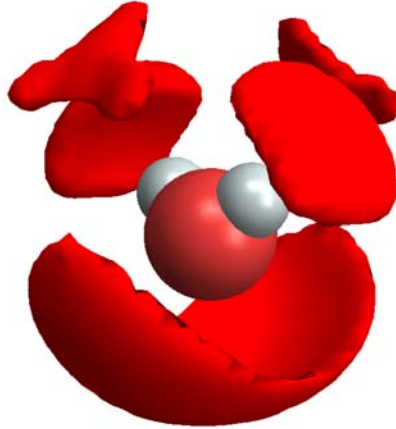


Figure 2.4 The oxygen-oxygen spatial distribution function of the SPC/E water at ambient conditions at a probability level of $g(r, \Omega) = 1.55$.

2.1.3.3 Dynamic Properties

The time-dependent properties of a model system are commonly examined with the aid of time correlation functions:

$$c_{\mathcal{A}\mathcal{B}}(t) = \frac{\langle \mathcal{A}(0)\mathcal{B}(t) \rangle}{\langle \mathcal{A}(0)\mathcal{B}(0) \rangle}, \quad (2.40)$$

where $c_{\mathcal{A}\mathcal{B}}(t)$ is the normalized time correlation function of properties \mathcal{A} and \mathcal{B} . The time integrals of the time correlation functions are related to the transport coefficients. For example, the self-diffusion coefficient is given by:^{1,2}

$$\mathcal{D}_\alpha = \frac{k_B T}{m} \int_{t=0}^{t=\infty} c_\alpha^{vv}(t) dt, \quad (2.41)$$

where \mathcal{D}_α is the translational self-diffusion coefficient in the principal molecular frame ($\alpha = x, y, z$), T is the temperature, k_B is the Boltzmann constant, m is the mass of the particle and $c_\alpha^{vv}(t)$ is the normalized linear velocity autocorrelation function defined in the local frame¹¹ (see Fig. 2.5):

$$c_\alpha^{vv}(t) = \frac{\langle [\mathbf{v}_\alpha(0)\mathbf{e}_\alpha(0)][\mathbf{v}_\alpha(t)\mathbf{e}_\alpha(0)] \rangle}{\langle [\mathbf{v}_\alpha(0)\mathbf{e}_\alpha(0)][\mathbf{v}_\alpha(0)\mathbf{e}_\alpha(0)] \rangle}, \quad (2.42)$$

where $\mathbf{e}_\alpha(0)$ are the unit vectors of the principal molecular frame at $t = 0$ and $\mathbf{v}_\alpha(t)$ is the α component of the linear velocity of the center of mass.

The self-diffusion coefficient can be also obtained from the mean-square displacement by using the Einstein relation:^{1,2}

$$2t\mathcal{D} = \lim_{t \rightarrow \infty} \frac{1}{3} \langle (\mathbf{r}_i(t) - \mathbf{r}_i(0))^2 \rangle, \quad (2.43)$$

where $\mathbf{r}_i(t)$ is the particle position.

In addition to providing information about the dynamics and transport coefficients, time-correlation functions can be used to calculate spectra via Fourier transforms.

2.1.3.4 Dielectric Properties

The dielectric constant of a model system is obtained by examining the equilibrium fluctuations of the total dipole moment \mathbf{M} of the primary simulation cell.¹²

$$\frac{(\epsilon - 1)(2\epsilon_{\text{RF}} + 1)}{2\epsilon_{\text{RF}} + \epsilon} = \frac{4\pi}{3} \frac{\langle \mathbf{M}^2 \rangle - \langle \mathbf{M} \rangle^2}{Vk_B T}, \quad (2.44)$$

with

$$\mathbf{M} = \sum_i \boldsymbol{\mu}_i \quad (2.45)$$

where $\boldsymbol{\mu}$ is the molecular dipole, V is the volume of the primary simulation cell, T is the temperature, k_B is the Boltzmann constant, ϵ_{RF} is the dielectric at the boundary and ϵ is the dielectric constant of the medium. Note, that calculation of the dielectric constant requires rather long simulation runs (especially at low temperatures and high densities) so that $\langle \mathbf{M}^2 \rangle$ reaches a stable value and $\langle \mathbf{M} \rangle$ is effectively zero. The variation of the static dielectric constant of the SPC/E water with time is shown in Fig. 2.6.

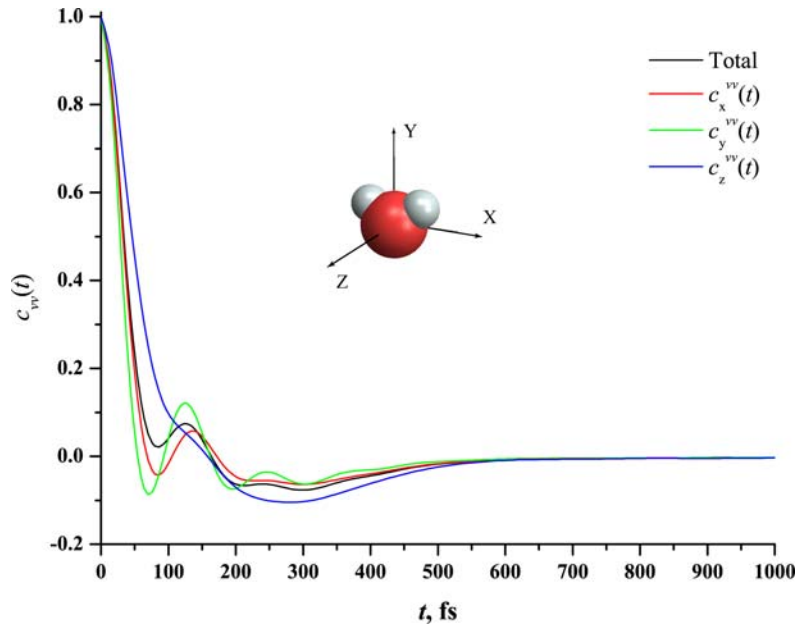


Figure 2.5 The normalized linear velocity autocorrelation function of the SPC/E water at ambient conditions.

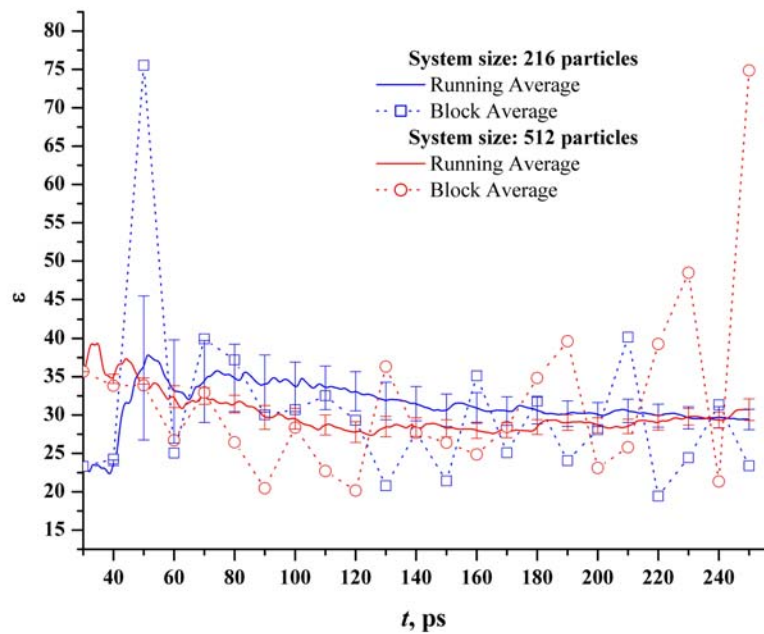


Figure 2.6 The static dielectric constant of the SPC/E water at 460 K and 0.785 g/cm^3 . The block size is 10 ps. Error bars represent standard error of the running average.

2.1.4 Water Models

Molecular simulations are widely used in the study of aqueous fluids. The potential describing the interactions between water molecules is an essential part of molecular modeling of aqueous systems. Over the years a large number of water models have been proposed. The history of the development, parameters and performance of interaction potentials for water has been described in several review articles.¹³⁻¹⁶ The main effort in the development of water models has been put into accurate representation of properties of water as a solvent.

Among the most successful effective pair-potentials for water is the Simple Point Charged Extended (SPC/E) model by Berendsen *et al.*⁹ This three-site rigid non-polarizable water model is represented by partial charges located directly on the oxygen and hydrogen atoms with the Lennard-Jones interaction potential on the oxygen. The geometry, charges and LJ parameters are given in Table 2.1. Despite its simplicity, the SPC/E model reproduces reasonably well the thermodynamics, structure and dynamics of real water over a wide range of states. The results of SPC/E model for the dielectric constant, self-diffusion coefficient, pair correlation functions, critical point parameters etc. agree well with experimental data.^{13-15, 17-24}

Another widely used family of water models is the Transferable Intermolecular Potentials (TIPs). The most commonly used is the four-site TIP4P model.²⁵ In contrast to the SPC/E potential, the negative charge in TIP4P model is positioned on the bisector of the HOH angle in the direction of the hydrogens. Several modifications of the TIP4P potential have been proposed to improve the performance of the model for high-density states and ices.²⁶⁻²⁹

Rigid non-polarizable condensed phase potentials, such as SPC/E and TIP4P, poorly describe the thermodynamic properties of a real water vapour due to their inability to account for the electronic polarization. Among the most successful polarizable water potentials³⁰⁻³⁵ are the

Polarizable Point Charge (PPC) model of Svishchev *et al.*³⁰ and the Gaussian Charge Polarizable Model (GCPM) developed by Chialvo and Cummings³³. While maintaining the simplicity of point charge models, the PPC model accounts for the polarization of the molecule in a local electric field. The polarization of the molecule is modeled in terms of the charge magnitude on its three sites and the position of the negative charge. In the GCPM model, which is similar to PPC, the partial point charges are replaced by diffuse (Gaussian) charge distributions. Polarizability is introduced via induced dipoles located at the centers of mass of the water molecules. The dispersion interactions in the GCPM are described by a Buckingham exp-6 potential. The parameters and calculated physical properties of select water models are given in Table 2.1. The geometries of water models listed in Table 2.1 are shown in Fig. 2.7.

It is worth mentioning that none of the models developed so far is capable of accurately representing the properties of water over substantially large ranges of temperature and density which include all three phases. Therefore, the choice of a water model largely depends on the phenomenon and conditions being examined. Further considerations include the cost of simulations which for non-polarizable models scales as a square of the number of sites. Implementation of the polarizability into water potential slows down calculations by a factor of 2 to 10.

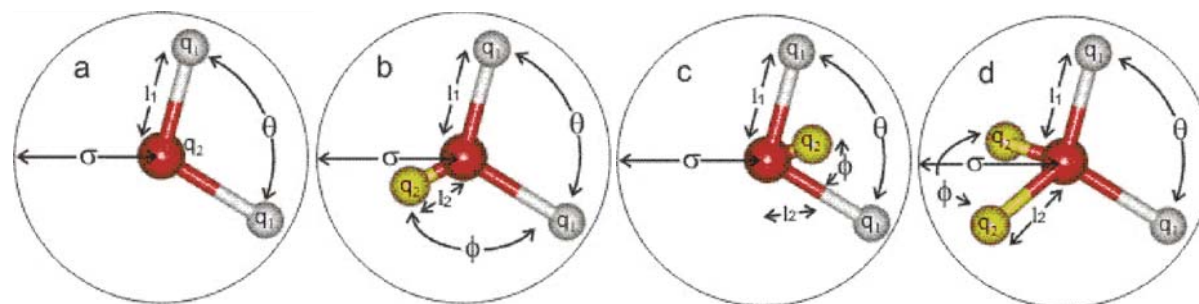


Figure 2.7 Geometries of water models (adapted from <http://www.lsbu.ac.uk/water/models.html>).

Indexes a-d indicate the geometry type of water models listed in Table 2.1.

Table 2.1 Model parameters and values for the calculated physical properties of water models.

Model	Type*	σ , Å	ϵ , kJ/mol	l_1 , Å	l_2 , Å	q_1	q_2	θ °	ϕ °	μ , D	ϵ^+	$D \times 10^{-5}$ cm ² /s ⁺	ρ_{\max} , °C	T_c , K	ρ_c , g/cm ³	P_c , bar
<i>SPC/E</i> ¹	a	3.166	0.65	1	-	0.4238	-0.8476	109.47	-	2.35 ²	71 ²	2.49 ³	-38 ⁴	640 ⁵	0.29 ⁵	160 ⁵
<i>TIP4P</i> ⁶	c	3.15	0.65	0.9572	0.15	0.52	-1.04	104.52	52.26	2.18 ⁷	53 ²	3.29 ³	-25 ⁷	588 ⁸	0.315 ⁸	149 ⁸
<i>TIP4P/2005</i> ⁹	c	3.159	0.7749	0.9572	0.1546	0.5564	-1.1128	104.52	52.26	2.30 ⁹	60 ⁹	2.08 ⁹	+5 ⁹	640 ⁸	0.31 ⁸	146 ⁸
<i>TIP5P</i> ⁷	d	3.12	0.67	0.9572	0.7	0.241	-0.241	104.52	109.47	2.29 ⁷	81.5 ⁷	2.62 ³	+4 ⁷	521.3 ¹⁰	0.336 ¹⁰	85.6 ¹⁰
<i>PPC</i> ¹¹	b	3.234	0.60	0.943	0.06	0.517	-1.034	106	127	2.52 ¹¹	77 ¹¹	2.6 ¹¹	+4 ¹¹	606 ¹²	0.30 ¹²	195 ¹²
<i>GCPM</i> ¹³	c	3.69	0.9146	0.9572	0.27	0.6113	-1.2226	104.52	52.26	2.723 ¹³	84.3 ¹³	2.26 ¹³	-13 ¹³	642.21 ¹³	0.334 ¹³	245.6 ¹³
<i>Exp.</i> ¹⁴										1.855 (gas)	78.4	2.30	3.984	647.1	0.322	220.64

* Refer to Fig. 2.7

+ At 298 K

1. Ref. [9]; 2. Ref. [11]; 3. Ref. [36]; 4. Ref. [37]; 5. Ref. [20]; 6. Ref. [25]; 7. Ref. [38]; 8. Ref. [39]; 9. Ref. [29]; 10. Ref. [40]; 11. Ref. [30]; 12. Ref. [21]; 13. Ref. [33]; 14. Ref. [41].

2.2 Flow Injection Techniques

Flow Injection⁴² (FI) is a family of powerful non-chromatographic methods for solution handling and data acquisition. FI principles are used in a variety of chemical, clinical, environmental and industrial applications.⁴³⁻⁴⁵ FI methods are based on injection of a well-defined volume of sample into a continuously flowing carrier stream. The designs of FI systems range from very simple to quite elaborate. The basic FI manifold consists of a pump, an injector, a reactor and a flow-through detector. The advantages of FI techniques over conventional batch methods include, but are not limited to, high degree of automation, flexibility and simplicity of instrumental set-up.

In addition to the application of FI methods in routine chemical analysis, continuous monitoring, on-line flow treatment, process control, etc. the FI can be also used as an impulse-response technique. In impulse-response FI experiments the information about physical and/or chemical transformation(s) in a flow system is obtained from analysis of the initial and final time-concentration profiles. Examples of impulse-response FI measurements include elucidation of molecular diffusion coefficients (Taylor dispersion technique), examination of thermal or chemical stability of target compounds/materials, dissolution rates, degree of enzyme immobilization etc.⁴⁶ For instance, corrosion of a target material inserted in the carrier stream, can be studied by repeatedly injecting small amounts of a corrosive agent and monitoring the release of material with suitable detection methods.⁴⁷

2.2.1 Residence Time Distribution

Perhaps one of the most important practical applications of the impulse-response technique in chemical engineering practice is the examination of the hydrodynamic performance

of chemical reactors.⁴⁸⁻⁵⁰ Analysis of impulse-response curves of an inert tracer compound gives information about the residence time distribution (RTD) function of a flow-through reactor vessel. The RTD function characterizes the time spent by an element of fluid from its entry into the system until it reaches the exit, see Fig. 2.8. The RTD curve provides useful information about the flow pattern (e.g. extent of fluid mixing, pathological flows etc.) which is used for diagnostics and optimization of reactor performance.^{49,51} The advantage of RTD measurements over the computational fluid dynamics (CFD) methods is that impulse-response experiments do not require an *a priori* knowledge of fluid properties whereas, solutions of the (Navier-Stokes) momentum balance equations relies on accurate values of thermodynamic and transport coefficients of a fluid.

The RTD function or *E*-curve is mathematically related to the input and response signals through the convolution integral:

$$R(t) = \int_0^t I(\tau)E(t-\tau)d\tau = I \otimes E, \quad (2.46)$$

where $I(t)$ and $R(t)$ are respectively input and response curves, $E(t)$ is the RTD function for which $\int_0^\infty E(t)dt = 1$. It is important to emphasize that, in contrast to the response curve, the RTD function of a vessel (at particular operating conditions) does not depend on the shape (form) of the input function. In other words, the RTD curve can be obtained by the deconvolution of an arbitrary input and the corresponding response functions. In practice, most of the flow injection experiments are performed by introducing a very short pulse of a tracer into a flowing system, which allows one to approximate the input signal $I(t)$ by the Dirac delta function, $C_0\delta(t)$, where C_0 is the initial concentration of the injected tracer. Although such approximation is rarely fulfilled in reality, it considerably simplifies the solution of Eq. 2.46.

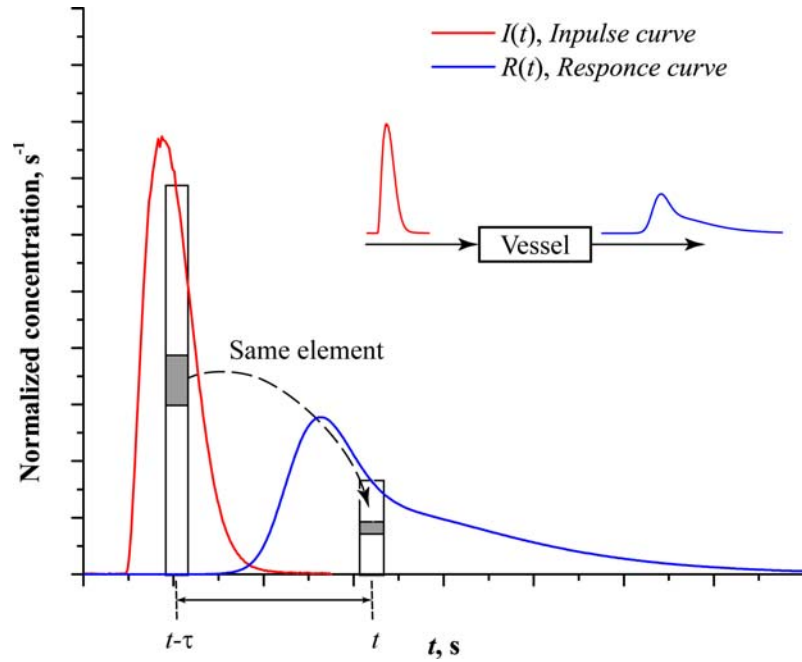


Figure 2.8 Schematic illustration of the RTD experiment. Adapted from Ref. [49]

The RTD function for a δ -input is given by:

$$E(t) = \frac{C_e(t)}{\int_0^{\infty} C_e(t) dt}, \quad (2.47)$$

where $C_e(t)$ is the exit concentration of a tracer at time t .

The RTD curve is typically characterized by calculating the moments of the distribution. Commonly, only the first two moments are considered. The first moment corresponds to the mean residence time of the fluid in the reactor vessel, τ , and is given by:

$$\tau = \int_0^{\infty} t \cdot E(t) dt. \quad (2.48)$$

The second moment of the distribution, the variance, σ^2 , describes the spread of a tracer due to dispersion processes:

$$\sigma^2 = \int_0^{\infty} (t - \tau)^2 E(t) dt . \quad (2.49)$$

The direct numerical evaluation of moments of the RTD function from the experimental impulse-response curves has the shortcoming of giving significant errors due to the weighting factor t^n , which puts a large weight on the tail of distribution.⁵² Various approaches to flow modeling and parameter estimation from the tracer injection experiments are discussed in detail in a number of publications, see Refs. [49, 51-53] and therein.

In short, behaviour of an ideal reactor can be described by using plug-flow (PF), perfect continuously stirred (CST) tank or power-law fluid (laminar flow) models. Real flow systems often deviate from ideal behaviour and are commonly modeled by using tanks-in-series (N -CST) or dispersed plug-flow (DPF) models. The axially dispersed plug-flow (ADPF) model is perhaps the most widely used model for the description of flow-through in vessels, and is given by the following differential equation:

$$\frac{\partial C}{\partial t} = D_a \frac{\partial^2 C}{\partial x^2} - \bar{u}_0 \frac{\partial C}{\partial x} - k' C , \quad (2.50)$$

where C is the tracer concentration, D_a is the axial dispersion coefficient, \bar{u}_0 is the area-averaged axial velocity of the fluid and k' is the first-order rate constant. In this model, the dispersion term accounts for the deviations of a real system from an ideal plug flow behaviour. Axial dispersion or longitudinal mixing of the fluid in a reactor vessel may occur due to several reasons, such as radial molecular diffusion, non-uniform fluid velocity profile distribution, etc. One of the main advantages of this flow model is that it allows for the description of flow patterns ranging from plug ($D_a = 0$) to fully mixed ($D_a \rightarrow \infty$) flows and does not require any prior knowledge of the

velocity distribution profile in the system. The axial dispersion coefficient, D_a , is commonly expressed as a characteristic dimensionless Péclet number, Pe_L :

$$Pe_L = \frac{uL}{D_a}, \quad (2.51)$$

where L is the length of a reactor. In a few special cases the ADPF model can be solved analytically. Thus, for small extents of axial dispersion ($Pe_L > 500$) in absence of chemical reaction ($k' = 0$) the E -curve is given by⁴⁹:

$$E(t) = \frac{I}{\tau} \sqrt{\frac{Pe_L}{4\pi}} \exp\left\{-\frac{Pe_L(t-\tau)^2}{4\tau^2}\right\}. \quad (2.52)$$

In case of a δ -impulse injection, the flow parameters, Pe_L and τ , can be evaluated by direct fitting the experimental response curve into Eq. 2.52.

Unfortunately, for a vast majority of situations (non-ideal injection of a tracer compound, complex flow-through reactor configuration etc.) the time-domain analytical solution can not be obtained. However, an analytical solution of an arbitrary flow model can be easily evaluated in the frequency domain with the aid of transfer functions.

2.2.2 Transfer Function Concept

Application of transfer functions in modeling flows in pipes, chemical reactors and analytical systems has been described in a number of publications, see Refs. [50, 51, 54-56] and therein. Briefly, the transfer function, $h(s)$, for the system initially at rest (or in equilibrium), is defined as the ratio of the Laplace transform of the response function of the system to the Laplace space perturbation input signal by the following equation:⁵⁴

$$h(s) = \frac{\int_0^{\infty} R(t)e^{-st} dt}{\int_0^{\infty} I(t)e^{-st} dt} = \frac{r(s)}{i(s)}, \quad (2.53)$$

where s is the Laplace space variable, $r(s)$ and $i(s)$ are the Laplace transforms of the response, $R(t)$, and the impulse, $I(t)$, functions, respectively. An analytical expression for a transfer function can be derived from Eq. 2.53 using a particular flow model and appropriate initial and boundary conditions. The most common flow models and their corresponding transfer functions are presented in Table 2.2.

Table 2.2 The most common flow models used in the RTD studies and the corresponding transfer functions.

<i>Flow Model:</i>	<i>Transfer Function:</i>
<i>a) Ideal Models:</i>	
<i>Plug-Flow (PF)</i>	$h(s) = \exp[-\tau_{PF} \cdot s]$
<i>Perfect Mixing (CSTR)</i>	$h(s) = \frac{1}{1 + \tau_H \cdot s}$
<i>a) Non-ideal Models</i>	
<i>Tanks-in-Series (N-CSTR)</i>	$h(s) = \frac{1}{(1 + \tau \cdot s)^N}$
<i>Axially Dispersed Plug-Flow (ADPF)</i>	
<i>Pe > 500</i>	$h(s) = \exp\left[\frac{Pe_L}{2}(1 - \varphi)\right]$
<i>Open Boundary Conditions</i>	$h(s) = \frac{1}{\varphi} \exp\left[\frac{Pe_L}{2}(1 - \varphi)\right]$
<i>Closed Boundary Conditions</i>	$h(s) = \frac{4 \cdot \varphi \exp\left[\frac{Pe_L}{2}(1 - \varphi)\right]}{(1 + \varphi)^2 - (1 - \varphi)^2 \exp[-Pe_L \cdot \varphi]}$
<i>where</i>	$\varphi = \sqrt{1 + \frac{4 \cdot s \cdot \tau}{Pe_L}}$

The transfer function approach is ideally suited for characterization of complex FI manifolds and/or flow patterns (e.g. multi-channel input, feedback control, presence of stagnant regions, channelling of fluid or short-circuiting etc.) where several different processes may occur simultaneously or in sequence. In short, a dynamical flow system in the Laplace domain can be visualized by using block diagrams, where each block represents a transfer function with block connectors indicating the flow of a signal, as in Fig. 2.9. Taking into consideration the design/geometry of the FI system, and/or by examining the experimental impulse/response curves, a suitable combined model can be selected. For example, the transfer function for a reactor, described by the plug-flow and complete mixing regimes in sequence, is given by:

$$h_R(s) = \exp[-\tau_{PF} \cdot s] \cdot \frac{1}{1 + s \cdot \tau_H}, \quad (2.54)$$

where τ_{PF} and τ_H are the plug-flow and the hydraulic residence times, respectively.

Thus, the Laplace domain response curve for a particular flow model can be easily obtained by combining the model's transfer function with an appropriate Laplace domain input signal, i.e. $r(s) = i(s)h_R(s)$. The most common input functions used in the RTD studies and their Laplace transforms are given in Table 2.3.

The model parameters can be obtained by using Fourier analysis⁵⁷, transfer function fitting in the Laplace domain⁵⁸ or time-domain analysis^{51,59,60}. The time-domain curve fitting method is considered to be the most accurate and robust procedure.⁵² The method is based on time-domain comparison of the experimental and predicted response curves, where the predicted response curve, $R'(t)$, is calculated by using the measured (or approximated) tracer impulse function, $I(t)$, and the flow model transfer function.

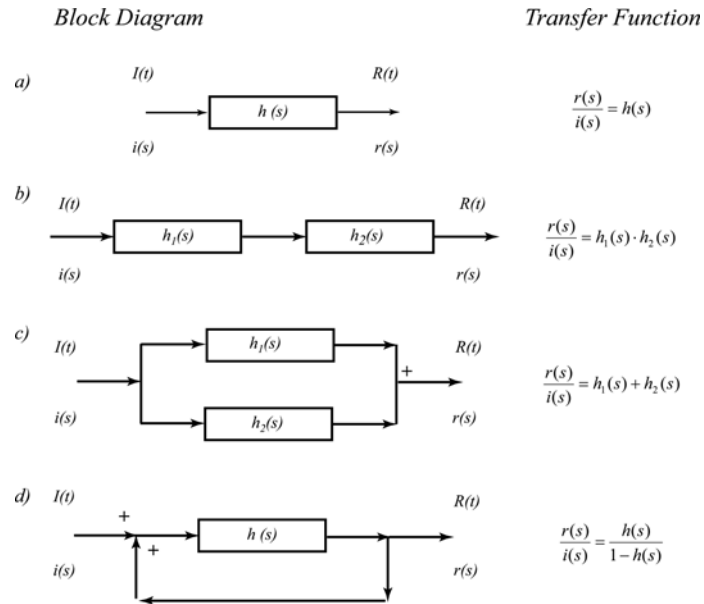
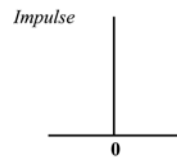
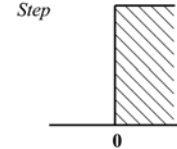
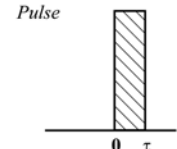


Figure 2.9 Block diagrams and the corresponding transfer functions for a) single, b) sequential, c) parallel and d) positive feedback processes.

Table 2.3 The most common input functions and their corresponding Laplace transforms.

	<i>Input Function, I(t)</i>	<i>Laplace Transform of Input Function, i(s)</i>
<i>Impulse</i>		<p style="text-align: center;"><i>Dirac Delta</i></p> <p style="text-align: center;">$C_i \delta(t)$</p> <p style="text-align: center;">C_i</p>
<i>Step</i>		<p style="text-align: center;"><i>Heaviside</i></p> <p style="text-align: center;">$C_i U(t)$</p> <p style="text-align: center;">$\frac{C_i}{s}$</p>
<i>Pulse</i>		<p style="text-align: center;">$C_i \{U(t) - U(t - \tau_{pulse})\}$</p> <p style="text-align: center;">$\frac{C_i (1 - \exp[-\tau_{pulse} \cdot s])}{s}$</p>

The normalized impulse curve may be expressed by a Fourier series as:

$$I(t) = \frac{a_0}{2} + \sum_{n=1}^{\infty} \left[a_n \cos\left(\frac{n \cdot \pi \cdot t}{\tau}\right) + b_n \sin\left(\frac{n \cdot \pi \cdot t}{\tau}\right) \right], \quad (2.55)$$

with Fourier coefficients given by

$$a_n = \frac{1}{\tau} \int_0^{2\tau} I(t) \cos\left(\frac{n \cdot \pi \cdot t}{\tau}\right) dt \quad (2.56)$$

and

$$b_n = \frac{1}{\tau} \int_0^{2\tau} I(t) \sin\left(\frac{n \cdot \pi \cdot t}{\tau}\right) dt, \quad (2.57)$$

where 2τ is a time long enough so that $I(t \rightarrow 2\tau) = 0$.

The predicted response function, $R'(t)$, can be also represented by the Fourier series:

$$R'(t) = \frac{a_0^+}{2} + \sum_{n=1}^{\infty} \left[a_n^+ \cos\left(\frac{n \cdot \pi \cdot t}{\tau}\right) + b_n^+ \sin\left(\frac{n \cdot \pi \cdot t}{\tau}\right) \right], \quad (2.58)$$

where the Fourier coefficients are

$$a_n^+ = \frac{1}{\tau} \int_0^{2\tau} R'(t) \cos\left(\frac{n \cdot \pi \cdot t}{\tau}\right) dt \quad (2.59)$$

and

$$b_n^+ = \frac{1}{\tau} \int_0^{2\tau} R'(t) \sin\left(\frac{n \cdot \pi \cdot t}{\tau}\right) dt. \quad (2.60)$$

The Fourier coefficients in Eqs. 2.55 and 2.58 are related through the definition of the transfer function in the Fourier domain ($s = in\pi/\tau$):

$$h\left(\frac{i \cdot n \cdot \pi}{\tau}\right) = \frac{\int_0^{2\tau} R(t) e^{-\left(\frac{i \cdot n \cdot \pi}{\tau}\right)t} dt}{\int_0^{2\tau} I(t) e^{-\left(\frac{i \cdot n \cdot \pi}{\tau}\right)t} dt}, \quad (2.61)$$

so that

$$a_n^+ - ib_n^+ = (a_n - ib_n) \cdot h\left(\frac{i \cdot n \cdot \pi}{\tau}\right). \quad (2.62)$$

Thus, the Fourier coefficients of the predicted response curve, $R'(t)$, can be evaluated based on the measured input signal and the transfer function parameters. The experimental and predicted response curves are then compared in terms of the root mean square error (*RMS*):

$$RMS = \sqrt{\frac{\int_{t_1}^{t_2} (R(t) - R'(t))^2 dt}{\int_{t_1}^{t_2} R(t)^2 dt}}, \quad (2.63)$$

which is minimized with respect to transfer function parameters using an optimization algorithm.

2.2.3 Taylor Dispersion Technique

The Taylor dispersion technique, another widely used application of the flow injection principles, is a commonly used method for molecular diffusion coefficient measurements, Refs. [61-66] and therein. The method, based on the original works by Taylor⁶⁷ and Aris⁶⁸, relies on the dispersion measurement of a pulse of a solute (pure or in solution) flowing in laminar flow through a long capillary tube of uniform diameter. The advantages of this technique over other methods^{69, 70} are low cost, experimental simplicity and high achievable accuracy.

Briefly, the Taylor dispersion method utilizes the parabolic velocity profile characteristic of laminar flow to resolve capillary peak broadening due to the effect of molecular diffusion alone. An ideal Taylor dispersion experiment is shown schematically in Fig. 2.10. The mathematical model considers a fluid flowing in laminar flow* through an infinitely long isothermal straight capillary tube of uniform diameter d_0 with average cross-section axial velocity \bar{u}_0 . At time $t = 0$ an infinitely narrow plug of sample is injected into the tube at $x = 0$, such that the concentration of the solute is uniform over the cross section. At laminar flow conditions the intermixing between streamlines can only occur due to molecular diffusion process. Thus, if the binary diffusion coefficient of a solute, denoted D_{12} , is infinitely small, the injected plug will assume a parabolic velocity profile which will yield a widely dispersed peak, see Fig. 2.11. If the opposite is true and the diffusion coefficient is very large, then the plug elements will uniformly sample all different streamlines which will result in the original sharp peak, slightly broadened by diffusion in the axial direction, Fig. 2.11.

The dispersion process can be mathematically described by the one-dimensional differential equation for the concentration perturbation averaged over a cross section (a.k.a. Axially Dispersed Plug-Flow model):

$$\frac{\partial C}{\partial t} = D_a \frac{\partial^2 C}{\partial x^2} - \bar{u}_0 \frac{\partial C}{\partial x}. \quad (2.64)$$

* Laminar or streamline flow – a type of fluid (liquid or gas) flow in which the fluid travels smoothly in parallel layers (laminae). The velocity, pressure and other properties remain constant at each point in the fluid.⁴⁹

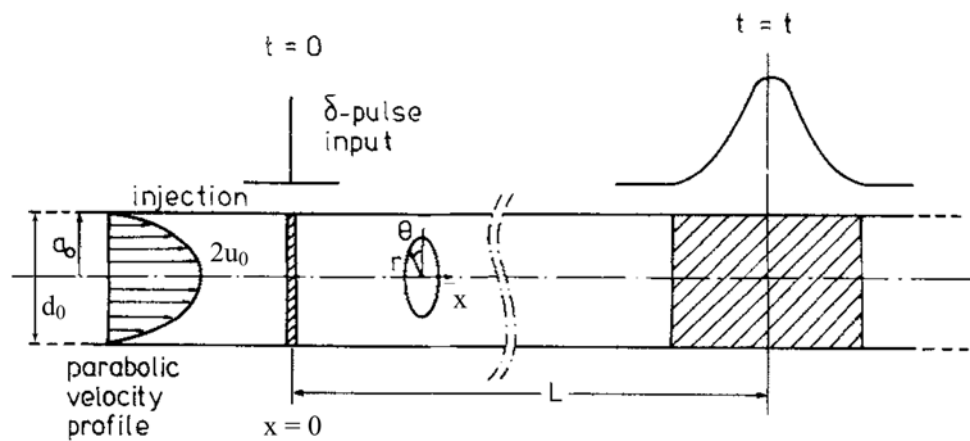


Figure 2.10 Schematic illustration of the ideal Taylor dispersion experiment. Adapted from Ref. [71].

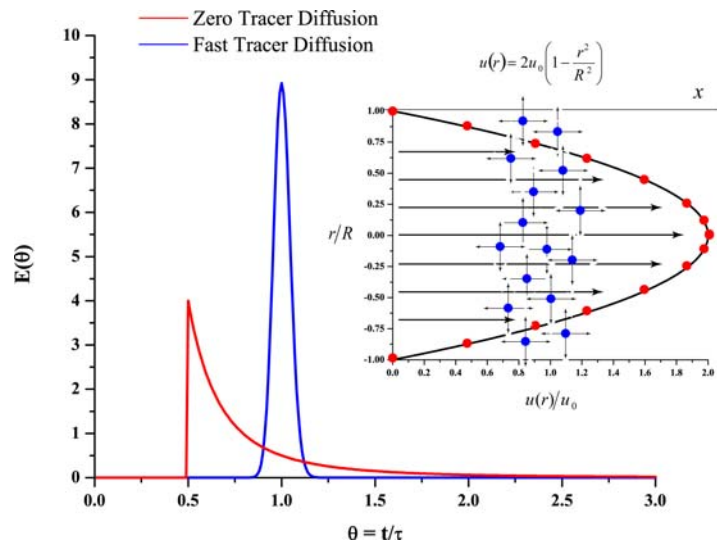


Figure 2.11 The effect of solute diffusion on the E -curve for laminar flow in straight tubes of uniform diameter (τ is the hydraulic holding time). The insert shows the parabolic velocity profile characteristic to laminar flow regime.

It has been shown^{67,68,71} that the axial dispersion coefficient, D_a , is related to the binary diffusion coefficient of a solute, D_{12} , via:

$$D_a \cong D_{12} + \frac{\bar{u}_0^2 d_0^2}{192 \cdot D_{12}} \quad (2.65)$$

where d_0 is the inner diameter of the tube. Note also that the result in Eq. 2.65 is an approximation which is subject to two experimental conditions:⁷¹

$$\bar{u}_0 > \frac{700 D_{12}}{(d_0/2)} \quad (2.66)$$

and

$$\frac{D_{12} \cdot \tau}{(d_0/2)^2} > 700 \quad (2.67)$$

where τ is the mean residence time of the pulse in the manifold. It is worth mentioning that the condition in Eq. 2.67 is rarely fulfilled in practice as it requires very long experimental runs. It

has been shown⁷¹ that for $\frac{D_{12} \cdot \tau}{(d_0/2)^2} > 10$ the error in estimation of the diffusion coefficient from

Eq. 2.65 is less than 0.6%, which is significantly lower than the experimental uncertainty of the measurement (typically on the order of 3-5 %).

Practical considerations for the Taylor dispersion technique include flow parameter determination from the concentration distribution measurements, sample introduction, influence of the sample concentration on the diffusivity measurements and diffusion tube geometry. It is worth mentioning that, due to experimental limitations, the Taylor dispersion measurements are conducted in coiled capillaries, whereas the mathematical treatment of the dispersion process outlined above is based on diffusion in long straight tubes of uniform circular diameter. The implications of helical tube geometry for the diffusion coefficient measurement have been

considered by several research groups.⁷¹⁻⁷³ Among dimensionless parameters required to describe the dispersion process in coiled tubes are the Reynolds number,

$$Re = \frac{\rho \bar{u}_0 d_0}{\eta}, \quad (2.68)$$

the Schmidt number,

$$Sc = \frac{\eta}{\rho D_{12}}, \quad (2.69)$$

the coil ratio,

$$\omega = \frac{D_c}{d_0}, \quad (2.70)$$

and the Dean number

$$De = Re \cdot \omega^{-0.5}, \quad (2.71)$$

where ρ is density and η is dynamic viscosity of the fluid. The Reynolds number is a measure of relative magnitudes of inertial and viscous forces. Thus, for flow in tubes a fully developed laminar flow is established for $Re < 2000$, whereas for $Re > 4000$, the flow is turbulent.⁴⁹ The Schmidt number determines the ratio of kinematic viscosity ($\nu = \eta/\rho$) to mass diffusivity. Typical values of Sc number are on the order of 0.25-2.5 and 250 – 2500 for gases and liquids, respectively. The De number is the Reynolds number modified by the coil curvature (i.e. analog of Re for coiled tubes). The relative error in parameter estimation from the experimental response curves obtained in helical tubes by using Eq. 2.65 is given by⁷²:

$$g(Re, Sc, \omega) = \left(-\frac{192}{\omega^2} \right) \left\{ \frac{4 Re^4}{576^2 \times 160} \left[-\frac{2569}{15840} Sc^2 + \frac{109}{43200} \right] + \frac{2 Re^2}{576 \times 144} \left[\frac{31}{60} Sc - \frac{25497}{13440} \right] + \left[\frac{419}{120 \times 196} + \frac{1}{4} \left(\frac{1}{Re^2 Sc^2} + \frac{1}{192} \right) \right] \right\} \quad (2.72)$$

Eq. 2.72 in combination with Eqs. 2.66 and 2.67 can be used as a guide for the FI manifold design as well as optimization of operating flow parameters. Alizadeh *et al.*⁷¹ indicate that, for $\omega > 100$ and any set of conditions that satisfy inequality $De^2Sc < 20$, the coiling of the diffusion tube has a negligible effect ($< 0.05\%$) on the dispersion process. Jansen⁷³, based on numerical calculations, concluded that for $\omega > 20$ and $De^2Sc < 100$ “*there will be no significant difference*” ($< 3\%$) with the straight tube behaviour.

2.3 References for Chapter 2

1. M.P. Allen and D.J. Tildesley, *Computer Simulation of Liquids*, Oxford University Press, Oxford (1989)
2. D. Frenkel and B. Smit, *Understanding Molecular Simulation: From Algorithms to Applications*, Academic Press, San Diego (1996).
3. P.G. Kusalik, *J. Chem. Phys.* **93**(5), 3520 (1990).
4. G. Hummer, N. Gronbech-Jensen and M. Neumann, *J. Chem. Phys.* **109** (7), 2791 (1998).
5. S.W. Deleeuw, J.W. Perram and E.R. Smith, *Proc. R. Soc. London Ser. A-Math. Phys. Eng. Sci.* **373** (1752), 27 (1980).
6. D.J. Evans, *Mol. Phys.* **34** (2), 317 (1977).
7. D.J. Evans and O. P. Morriss, *Comput. Phys. Rep.* **1** (6), 297 (1984).
8. H.C. Andersen, *J. Chem. Phys.* **72** (4), 2384 (1980).
9. H.J.C. Berendsen, J.R. Grigera and T.P. Straatsma, *J. Phys. Chem.* **91** (24), 6269 (1987).
10. P.G. Kusalik and I.M. Svishchev, *Science* **265** (5176), 1219 (1994).
11. I.M. Svishchev and P.G. Kusalik, *J. Phys. Chem.* **98** (3), 728 (1994).
12. M. Neumann, O. Steinhauser and G. S. Pawley, *Mol. Phys.* **52** (1), 97 (1984).
13. D. van der Spoel, P.J. van Maaren and H.J.C. Berendsen, *J. Chem. Phys.* **108** (24), 10220 (1998).
14. A. Wallqvist and R. D. Mountain, *Rev. Comput. Chem.* **13**, 183 (1999).
15. A.G. Kalinichev, *Rev. Mineral. Geochem.* **42**, 83 (2001).

16. B. Guillot, *J. Mol. Liq.* **101** (1-3), 219 (2002).
17. J. Alejandro, D.J. Tildesley and G.A. Chapela, *J. Chem. Phys.* **102** (11), 4574 (1995).
18. G.C. Boulougouris, I.G. Economou and D.N. Theodorou, *J. Phys. Chem. B* **102** (6), 1029 (1998).
19. J. R. Errington, K. Kiyohara, K. E. Gubbins and A.Z. Panagiotopoulos, *Fluid Phase Equilib.* **150-151**, 33 (1998).
20. Y. Guissani and B. Guillot, *J. Chem. Phys.* **98** (10), 8221 (1993).
- 2.1 T.M. Hayward and I.M. Svishchev, *Fluid Phase Equilibria* **182** (1-2), 65 (2001).
22. R. Mountain and A. Wallquist, "A collection of results for the SPC/E water model." NISTIR 5778 (1996).
23. M. Neumann, *Computer simulation of water and the dielectric equation of state*, in Physical Chemistry of Aqueous Systems: Meeting the Needs of Industry, Proceedings of the 12th International Conference on the Properties of Water and Steam, edited by H. J. White Jr., J. V. Sengers, D. B. Neumann and J. C. Bellows, pp. 261-268 (1995).
24. E. Wasserman, B. Wood and J. Brodholt, *Berichte Der Bunsen-Gesellschaft-Phys. Chem. Chem. Phys.* **98** (7), 906 (1994).
25. W. L. Jorgensen, J. Chandrasekhar, J. D. Madura, R. W. Impey and M. L. Klein, *J. Chem. Phys.* **79** (2), 926 (1983).
26. S.W. Rick, *J. Chem. Phys.* **114** (5), 2276 (2001).
27. H. W. Horn, W. C. Swope, J. W. Pitera, J. D. Madura, T. J. Dick, G. L. Hura and T. Head-Gordon, *J. Chem. Phys.* **120** (20), 9665 (2004).

28. J.L.F. Abascal, E. Sanz, R.G. Fernandez and C. Vega, *J. Chem. Phys.* **122** (23), 234511 (2005).
29. J.L.F. Abascal and C. Vega, *J. Chem. Phys.* **123** (23), 234505 (2005).
30. I.M. Svishchev, P.G. Kusalik, J. Wang and R.J. Boyd, *J. Chem. Phys.* **105** (11), 4742 (1996).
31. P.J. van Maaren and D. van der Spoel, *J. Phys. Chem. B* **105** (13), 2618 (2001).
32. H.A. Stern, F. Rittner, B.J. Berne and R.A. Friesner, *J. Chem. Phys.* **115** (5), 2237 (2001).
33. P. Paricaud, M. Predota, A.A. Chialvo and P.T. Cummings, *J. Chem. Phys.* **122** (24), (2005).
34. Y.J. Wu, H.L. Tepper and G.A. Voth, *J. Chem. Phys.* **124** (2), 024503 (2006).
35. G. Lamoureux, E. Harder, I. V. Vorobyov, B. Roux and A. D. MacKerell, *Chem. Phys. Lett.* **418** (1-3), 245 (2006).
36. M.W. Mahoney and W.L. Jorgensen, *J. Chem. Phys.* **112** (20), 8910 (2000).
37. L.A. Baez and P. Clancy, *J. Chem. Phys.* **101** (11), 9837 (1994).
38. M.W. Mahoney and W.L. Jorgensen, *J. Chem. Phys.* **112** (20), 8910 (2000).
39. C. Vega, J.L.F. Abascal and I. Nezbeda, *J. Chem. Phys.* **125** (3), 034503 (2006).
40. M. Lisal, J. Kolafa and I. Nezbeda, *J. Chem. Phys.* **117** (19), 8892 (2002).
41. H. J. White Jr. *et al.*, *Physical Chemistry of Aqueous Systems: Meeting the Needs of Industry*, Proceedings of the 12th International Conference on the Properties of Water and Steam (1995).
42. J. Ruzicka and E. H. Hansen, *Anal. Chim. Acta* **78** (1), 145 (1975).
43. J. M. Calatayud and M. C. Icardo, *Flow Injection Analysis | Clinical and Pharmaceutical Applications*, in *Encyclopedia of Analytical Science*, edited by P. Worsfold, A. Townshend and C. Poole, Elsevier, Oxford, pp. 76-89 (2005).

44. A.F. Danet and M. Badea, *Flow Injection Analysis | Industrial Applications*, in Encyclopedia of Analytical Science, edited by P. Worsfold, A. Townshend and C. Poole, Elsevier, Oxford, pp. 89-97 (2005).
45. M. Miró and W. Frenzel, *Flow Injection Analysis | Environmental and Agricultural Applications*, in Encyclopedia of Analytical Science, edited by P. Worsfold, A. Townshend and C. Poole, Elsevier, Oxford, pp. 57-76 (2005).
46. J. Ruzicka, *Fresenius Zeitschrift Fur Analytische Chemie* **329** (6), 653 (1988).
47. J. Ruzicka and E.H. Hansen, *Anal. Chim. Acta* **179**, 1 (1986).
48. P.V. Danckwerts, *Chem. Eng. Sci.* **50** (24), 3857 (1952).
49. O. Levenspiel, *Chemical Reaction Engineering*, 3rd ed., Wiley & Sons (1999).
50. A. Pinheiro Torres and F. A. R. Oliveira, *J. Food Eng.* **36** (1), 1 (1998).
51. C.Y. Wen and L.T. Fan, *Models for Flow Systems and Chemical Reactors*, Marcel Dekker Inc., New York (1973).
52. M.A. Fahim and N. Wakao, *Chem. Eng. J.* **25** (1), 1 (1982).
53. S.D. Kolev, *Anal. Chim. Acta* **308** (1-3), 36 (1995).
54. M.J. Hopkins, A. J. Sheppard and Paul Eisenklam, *Chem. Eng. Sci.* **24** (7), 1131 (1969).
55. A. Abad, S. C. Cardona, J. I. Torregrosa, F. López and J. Navarro-Laboulais, *J. Math. Chem.* **V38** (4), 541 (2005).
56. C. Castelain, D. Berger, P. Legentilhomme, A. Mokrani and H. Peerhossaini, *Int. J. Heat Mass Transfer* **43** (19), 3687 (2000).

57. S. K. Gangwal, R. R. Hudgins, A. W. Bryson and Silvestro.Pi, *Can. J. Chem. Eng.* **49** (1), 113 (1971).
58. K. Østergaard and M. L. Michelsen, *Can. J. Chem. Eng.* **47**, 107 (1969).
59. W.C. Clements, *Chem. Eng. Sci.* **24** (6), 957 (1969).
60. A.S. Anderssen and E. T. White, *Chem. Eng. Sci.* **25** (6), 1015 (1970).
61. T. Umecky, T. Kuga and T. Funazukuri, *J. Chem. Eng. Data* **51** (5), 1705 (2006).
62. N. Mogi, E. Sugai, Y. Fuse and T. Funazukuri, *J.Chem.Eng.Data* **52** (1), 40 (2007).
63. R. Niesner and A. Heintz, *J. Chem. Eng. Data* **45** (6), 1121 (2000).
64. T. Funazukuri, C. Y. Kong and S. Kagei, *J. Supercrit. Fluids* **38** (2), 201 (2006).
65. R. Castillo, C. Garza and J. Orozco, *J. Phys. Chem.* **96** (3), 1475 (1992).
66. X.N. Yang and M.A. Matthews, *J. Colloid. Interface Sci.* **229** (1), 53 (2000).
67. G.I. Taylor, *Proc. Roy. Soc. Lond.* **A219**, 186 (1953).
68. R. Aris, *Proc. Roy. Soc. Lond.* **A235**, 67 (1956).
69. K.K. Liong, P.A. Wells and N.R. Foster, *J. Supercrit. Fluids* **4** (2), 91 (1991).
70. T. Funazukuri, C.Y. Kong and S. Kagei, *J. Supercrit. Fluids* **46** (3), 280 (2008).
71. A. Alizadeh, C.A. Nieto de Castro and W. A. Wakeham, *Int. J. Thermophys.* **1** (3), 243 (1980).
- 72 R.J. Nunge, T.-S. Lin and W.N. Gill, *J. Fluid Mech.* **51** (02), 363 (1972).
73. L.A.M. Janssen, *Chem. Eng. Sci.* **31** (3), 215 (1976).

Chapter 3

Spatial Hydration Maps and Dynamics of Naphthalene in Ambient and Supercritical Water

3.1 Abstract

The hydration structures and dynamics of naphthalene in aqueous solution are examined using molecular-dynamics simulations. The simulations are performed at several state points along the coexistence curve of water up to the critical point, and above the critical point with the density fixed at 0.3 g/cm^3 . Spatial maps of local atomic pair-density are presented which show a detailed picture of the hydration shell around a bicyclic aromatic structure. The self-diffusion coefficient of naphthalene is also calculated. It is shown that water molecules tend to form π -type complexes with the two aromatic regions of naphthalene, where water acts as the H-bond donor. At ambient conditions, the hydration shell of naphthalene is comprised, on average, of about 39 water molecules. Within this shell, two water molecules can be identified as π -coordinating, forming close to one H-bond to the aromatic rings. With increasing temperature, the hydration of naphthalene changes dramatically, leading to the disappearance of the π -coordination near the critical point.

3.2 Introduction

Hydrophobic hydration has become a topic of considerable interest during the last half century¹⁻³. The hydrophobic effects are important in stabilizing biological structures. They also determine the environmental fate of many hazardous contaminants, such as polycyclic aromatic hydrocarbons (PAHs). When a hydrophobic substance is dissolved in water, the network of hydrogen (H-) bonds tends to reorganize around a solute by creating a cavity. Aromatic species are particular interesting candidates for the study of the hydrophobic hydration, as they form weak π -type complexes with water.

Computer simulations provide most of our current information concerning the structure of water around the solute. In recent years several investigations of benzene - water interactions have been carried out, using Monte Carlo (MC) and molecular-dynamics (MD) methods.⁴⁻¹⁴ These studies have shown that water molecules form a hydrophobic cavity around benzene, with little preference for the C-H \cdots OH₂ complex formation in the plane of the benzene ring. The results also indicate that axially coordinated water molecules tend to adopt a π -type H-bonding arrangement along the C₆ axis of benzene (H-bond is formed between the hydrogens of water and the π -electronic system of the aromatic ring); see, for example, local density maps given by Raschke and Levitt⁴, and Laaksonen *et al.*¹¹ MC studies by Ravishanker *et al.*⁸ and Linse *et al.*¹⁰ have reported the axial coordination of 2 and 2.8 water molecules respectively, whereas MD study by Schravendijk and van der Vegt¹³ reports the presence of one π -type hydrogen bond between the center of the aromatic ring of benzene and water. It is worthwhile noting that in a classical point-charge model a small partial negative charge is placed on the carbon atoms of benzene (with the periphery hydrogens carrying positive charges), which favours H-bond formation between the central area of the ring and axially coordinated water molecules.¹⁵

In this work we have chosen to study naphthalene, an important bicyclic aromatic species. Its molar solubility in water at room temperature is approximately two orders of magnitude lower than that of benzene. Naphthalene, like benzene, has an oblate shape. It has larger surface area, and this can be used to explain its lower solubility (over benzene). The effects of aromaticity are less obvious to discern. On the one hand, an aromatic nature of this molecule should favour π -complexation with water, as its structure is essentially two fused benzene rings. On the other hand, the two carbons making up the fused-ring region of naphthalene (carbons 9 and 10 in the standard nomenclature, see Fig. 3.1) exhibit partial positive charges, as shown by *ab-initio* studies.^{16,17} One can argue that its ability to form H-bonds is constrained due to a reduction in negative charge density on its fused-ring structure, hence, its low molar solubility in water.

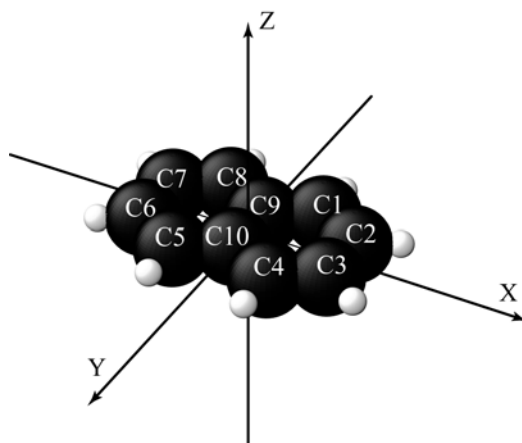


Figure 3.1 Molecular geometry and reference axes for naphthalene

Another point of interest is the influence of temperature on hydration. The three-dimensional (3D) H-bond network structure of water begins to disappear above 400 K, as revealed by neutron scattering studies and computer simulations, which has a dramatic effect on

aqueous solubility and critical micelle concentration.¹⁸⁻²⁰ To our knowledge, the effect of temperature on hydration of naphthalene has not yet been investigated.

The main purpose of this work is to characterize the hydration structure around naphthalene by means of MD simulation, from ambient to supercritical conditions. The detailed 3D maps of local atomic pair-density are presented. We calculate the number of water molecules making up the first hydration shell, or the coordination number, and the extent of H-bonding to the aromatic rings. The self-diffusion coefficient of naphthalene in water is also calculated, as the experimental measurements are not in agreement with each other. This information is needed in many practical applications, such as the supercritical water oxidation technology and environmental modeling.

The remainder of this chapter is organized as follows. Computational details are described in Section 3.3. Simulation results are discussed in Section 3.4. Our conclusions are given in Section 3.5.

3.3 Computational Details

The simple point-charge (SPC/E) model of Berendsen *et al.*²¹ for water was used in this study. The point charge parameters and geometry chosen for naphthalene were by McDonald *et al.*¹⁶ Simulations of naphthalene-water system were performed in the *NVT* ensemble along the coexistence curve of the SPC/E water between 263 and 633 K, and above the critical point at 833K with the density fixed at 0.3 g/cm³. Table 3.1 lists examined state points, together with the simulated values for the self-diffusion coefficient of naphthalene. Note that the critical temperature of the SPC/E water was estimated to be 630 K by Bougoulouris *et al.*²² and 641 K by Hayward *et al.*²³ The system size was 988 water molecules and 1 naphthalene molecule. The thermostatted equations of motions were integrated using the fourth-order Gear algorithm²⁴ with

the time step of 1 fs, and the rotational degrees of freedom were represented using quaternions²⁵. The long-range Coulombic forces were evaluated using the Ewald summation technique in cubic periodic boundary conditions. The Lennard-Jones interaction cutoff radius was set at half of the cell side length. The equilibrated simulation run times were 400 ps long. The self-diffusion coefficients were calculated from the velocity autocorrelation function. The statistical uncertainty in the self-diffusion coefficient for naphthalene was estimated to be around 10% at 298 K increasing to 30% at 833 K, while for water the uncertainty was less than 1%. A Linux-based parallel Transport GX28 system with dual 64 bit AMD Opteron processors was employed.

We have also performed an additional simulation of benzene-water mixture at infinite dilution at temperature of 298 K. The model of Jorgensen⁷ for benzene was used.

Table 3.1 Simulated state points and self-diffusion coefficients, D_{self} , for naphthalene

<i>Temperature (K)</i>	<i>Density ($\times 10^3 \text{ kg/m}^3$)</i>	<i>D_{self} ($\times 10^9 \text{ m}^2/\text{s}$)</i>
263	1.000	0.292
298	1.000	1.21
373	0.952	3.15
473	0.847	7.55
573	0.665	16.9
633	0.3	59.3
833	0.3	56.5

3.4 Results and Discussion

3.4.1 Analysis of Spatial Distribution Functions

The traditional radial distribution function (RDF), the $g(r)$, the usual output of computer simulations and x-ray diffraction (or neutron scattering) experiments, does not fully describe liquid structure in a system where particles interact via strongly anisotropic (direction dependent) potentials. Better understanding of complex liquids can be achieved by using the spatial distribution function (SDF), the $G(\mathbf{R})$ or $G(r, \mathbf{\Omega})$, where r and $\mathbf{\Omega} = (\theta, \phi)$ are the radial and angular coordinates of the site-site separation vector, \mathbf{R} . In particular, the spatial distribution function can be used to map and visualize the 3D distribution of atomic (molecular) density surrounding each molecule in a liquid, as shown by Svishchev and Kusalik²⁶, and Soper²⁷ in their work with water. Some of its recent applications to the study of hydrophobic hydration include benzene-water⁴ and phenol-water²⁸ systems.

In this study we provide detailed 3D maps of local solvent density around a naphthalene molecule in an infinitely dilute aqueous solution. Fig. 3.2(a) illustrates the local structure at ambient conditions. In this figure the total SDF of oxygen atoms of water around carbon atoms of naphthalene is shown (from top and side perspectives). This density map graphically represents ten individual $C_{\text{naphthalene}}-O_{\text{water}}$ pair-distributions. Note that in Fig. 3.2(a) red color identifies locations of oxygen atoms around each carbon site at the probability level of the $G_{\text{CO}}(r, \mathbf{\Omega}) = 1.6$ or higher. At this probability level, both an overall hydration shell (large “carved” oval shape with solute molecule inside) and its π -coordinating water molecules (2 pairs of small ovals on both sides of the naphthalene plane) are clearly revealed.

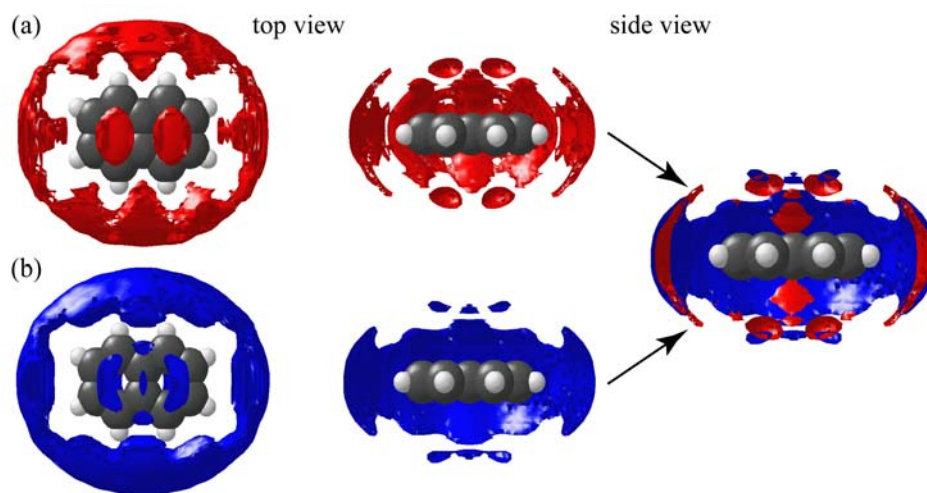


Figure 3.2 Total spatial distribution function of (a) oxygen and (b) hydrogen atoms of water around carbon atoms of naphthalene, with a probability level of $g_{CO}(r, \Omega) = 1.6$ and $g_{CH}(r, \Omega) = 1.3$, respectively, at 298 K. Combined side view plot is also shown.

Spatial density map in Fig. 3.2(a) is drawn using the spherical reference frame for each individual $C_{\text{naphthalene}}-O_{\text{water}}$ distribution; only regions of the total local pair-density equal to or higher than 1.6 are displayed. To gain further insights into the local structure we also show actual pair-density levels at different separations from a central molecule. This is done by mapping the coordinates of water molecules into the principal Cartesian frame (with the origin placed on the molecular center of symmetry of naphthalene, see Fig. 3.1), and displaying the two-dimensional (2D) density plots for different planar slices, cut through the spatial density map⁴. Thus, in Fig. 3.3 we present the 2D maps of local oxygen density for the orthogonal X - Y , X - Z and Z - Y planes, at three different temperatures. These plots help visualize the hydration shell in the plane of solute molecule (the X - Y plane), and in the perpendicular-to-plane directions. In Fig. 3.3 the color depth represents the probability level. The hydration shell (cage), π -coordination and cavity (excluded

volume) can be clearly seen from the red-scale shading, where white represents lowest density increasing to dark red as highest density. Comparison of these density plots at increasing temperatures shows a diminishing structure around naphthalene, noting that near the critical point, at 633 K, there is effectively no π -coordination or “cage” remaining.

Similarly, Fig. 3.2(b) shows the total SDF of hydrogen atoms of water around naphthalene, which combines 20 individual $C_{\text{naphthalene}}\text{-H}_{\text{water}}$ SDFs. It is important to note that the hydrogen density is offset, positioned towards the non-fused carbons of the molecule, or in other words to the outside of the ovals seen in the carbon-oxygen SDF [Fig. 3.2(a)]. This is due to the geometry of the water molecule and the mode of coordination, with one of the two hydrogens pointing toward the aromatic ring (H-bonding). The inner hydrogen is hidden from view in Fig. 3.2(b), but can be clearly seen in the 2D maps of Fig. 3.4 showing the probability and structure of the hydrogen density in the X - Y , X - Z and Z - Y planes passing through the center of the naphthalene molecule (same planar cuts through the SDF as in Fig. 3.3, but now for the hydrogen density). A progressive decline of π -coordination with temperature is again clearly revealed in this figure. At a temperature of 473 K, π -coordination nearly disappears, while a diminished hydration cage is still evident, as demonstrated by the enhanced pair-density around the periphery of the naphthalene ring [see Figs. 3.3(b) and 3.4(b)]. At 633 K, the hydrogen density distribution reveals no specific hydration structures.

We now turn our focus on the calculation of the total coordination number, or the number of water molecules involved in forming the hydration shell of naphthalene. Traditionally, the calculation of the coordination number has relied upon the integration of the radial distribution functions. For example, the coordination number for water (around water) in neat liquid is usually calculated by integrating the first peak of the oxygen-oxygen pair-density distribution, the $g_{\text{OO}}(r)$. It is apparent from Figures 3.2-3.4 that the hydration shell of naphthalene has an ellipsoidal

shape, with some localized features due to the π -coordination. Using the rotationally averaged and spherically symmetric atom – atom RDFs, i.e. the $g_{CO}(r)$ functions, or the center-of-mass – center-of-mass RDF for naphthalene – water pairs can be ambiguous (as for any large multi-site molecule), due to spatial averaging.

In order to account for the shape of the hydration shell, we have chosen to perform the 3D integration of the unfolded SDF, the $G_{CO}(\mathbf{R})$, as it offers the most straightforward definition of the coordination number. The coordination number is calculated from a triple integral of the solute-solvent SDF over volume occupied by the hydration shell. We shall use the Cartesian coordinate frame and write it as:

$$n_{Naph-O, total} = \rho \cdot \iiint_{V_h} G_{CO}(\mathbf{R}) dV, \quad (3.1)$$

where $n_{Naph-O, total}$ is the total coordination number of water molecules around naphthalene, $G_{CO}(\mathbf{R})$ is the total carbon-oxygen pair-distribution, ρ_O is the average number density of oxygen atoms, $\mathbf{R} = (x, y, z)$, $dV = dx dy dz$ and V_h is the volume of the hydration shell. It should be noted that we normally compute and accumulate the site-site spatial distribution functions during the simulation run using the local spherical coordinates, r and $\mathbf{\Omega} = (\theta, \phi)$, of the site-site separation vector, \mathbf{R} . The simulated pair-density distributions can be also mapped into the principal Cartesian reference frame, in which molecular axes of symmetry define the reference axes (as in Fig. 3.1). Use of Cartesian coordinates has an advantage of uniformly sized volume elements, which can simplify the visualization of the local pair-density for large molecules and its multiple integration. One can also directly map the local pair-density into the Cartesian space during the simulation run, as was done by Raschke and Levitt in their study of benzene-water system⁴.

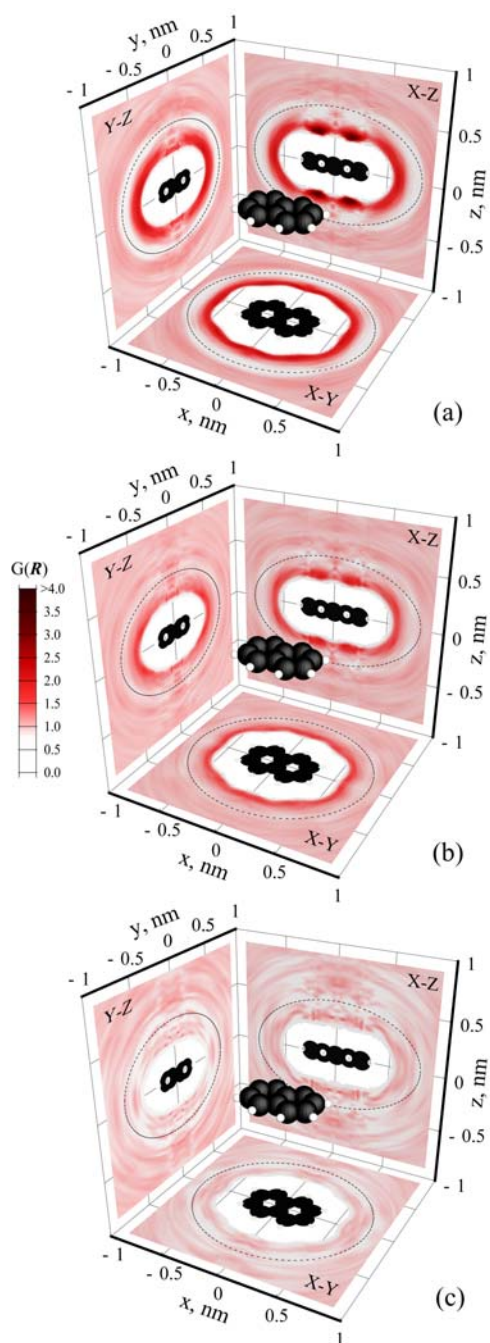


Figure 3.3 2D plots showing the probability density of oxygens of water around carbons of naphthalene at (a) 298, (b) 473 and (c) 633 K. Cuts through the carbon-oxygen SDF along the orthogonal X - Y , X - Z and Z - Y planes are shown. Color depth represents probability level. The integration boundaries for the Equation (3.1) are shown with the thin dashed lines.

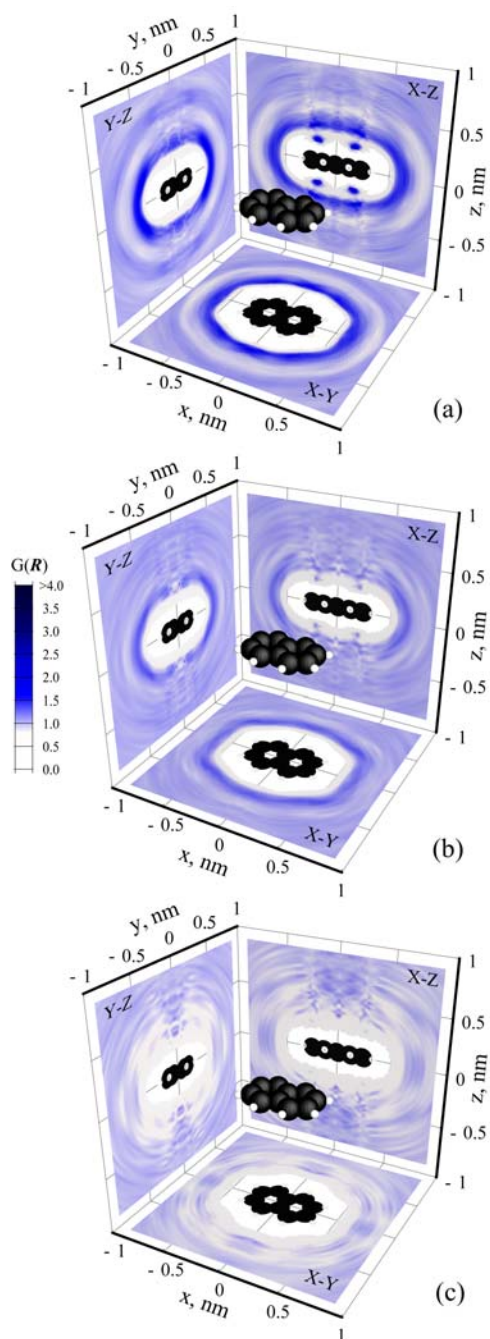


Figure 3.4 2D plots showing the probability density of hydrogens of water around carbons of naphthalene at (a) 298, (b) 473 and (c) 633 K. Cuts through the carbon-hydrogen SDF along the orthogonal X - Y , X - Z and Z - Y planes are shown. Color depth represents probability level.

The integration boundaries in Eq. 3.1 (i.e. the outer boundaries of the hydration shell) represent the surface in 3D space on which the first minima of the SDF are located. In practice, locating these minima can be tricky due to the statistical noise in the SDF and/or “weak” structural features (for example, the SDF may have no clear minimum in certain spatial regions around solute molecule). In our case, the hydration shell is nearly ellipsoidal in shape, and using this assumption it was decided to fit to the locations of first minima of the SDF $G_{\text{Co}}(\mathbf{R})$, an ellipsoid of the form:

$$\frac{x^2}{a^2} + \frac{y^2}{b^2} + \frac{z^2}{c^2} = 1, \quad (3.2)$$

where a , b and c are the fit parameters. For comparison, one can draw an analogy with the radial analysis of the structure in simple liquids, where the first minimum of the $g(r)$ usually defines the radius of the outer boundary of the first coordination shell (sphere). In this study we use a non-spherical volume element. Then, in the fit procedure, we simply require the $G_{\text{Co}}(\mathbf{R})$ to have a global minimum value on a quadric (ellipsoidal) surface given by Eq. 3.2. We may add that this 3D analysis can be easily extended to arbitrary solvation shapes.

To illustrate our approach, we display the integration boundaries for the naphthalene-water system, as projected onto the three principal coordinate planes X - Y , X - Z and Y - Z , in Fig. 3.3. They are shown as ellipses (the thin dashed lines) overlaying the regions of the lowest pair-density (the lighter colored regions) that are located on the outside of the first maximum (the darker area). The coordination number is thus the average number of water molecules located within the ellipsoidal volume which (projected) boundaries are the thin dashed lines in Fig. 3.

The average coordination number of naphthalene at ambient conditions as determined from our simulations appears to be 39.2 water molecules. At higher temperatures the coordination number of naphthalene decreases sharply, to about 6.5 water molecules at 633 K. All our

coordination numbers are given in Fig. 3.5. For comparison, we have also performed a simulation of benzene in water at infinite dilution and calculated its coordination number from the total carbon-oxygen SDF for the benzene-water pairs. The coordination number of benzene at ambient conditions appears to be 32.0. A similar value (30.7 coordinated water molecules) has been reported by Linse¹⁰, although for a different benzene model.

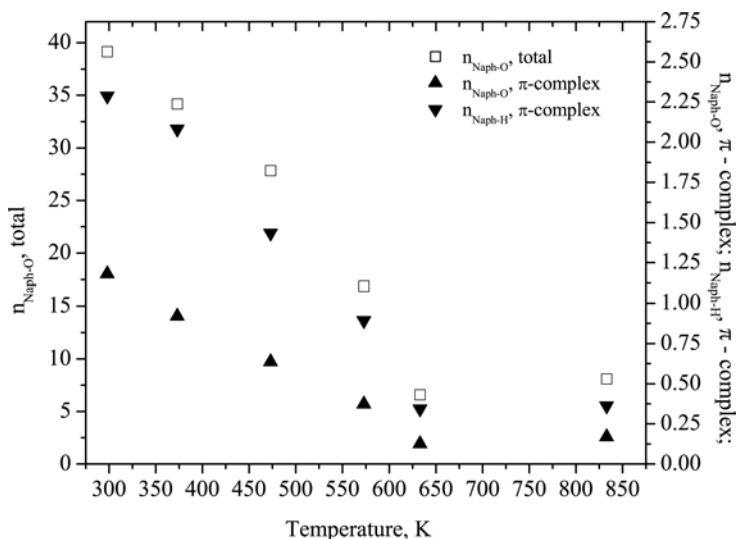


Figure 3.5 Total coordination numbers, $n_{\text{Naph-O}, \text{total}}$, for naphthalene. Also shown are π -coordination numbers, $n_{\text{Naph-O}, \pi\text{-complex}}$ and π -type H-bond numbers, $n_{\text{HB}, \pi\text{-complex}}$.

3.4.2 Cylindrical Distribution Functions and π -Coordination

One of the most interesting features of the naphthalene hydration maps are four distinct peaks located above and below the plane of the molecule (two on each side), due to the π -coordinated water molecules. Our next step will be the calculation of their average number (hereafter, π -coordination number), as well as the number of hydrogen bonds formed by these

molecules with the biaromatic structure. For the analysis of coordination and H-bond numbers in the π -region we have employed the cylindrical distribution function (CDF) introduced by Plugatyr *et al.*²⁸ in their work with phenol. We recall that the CDF $g(r, z)$ is defined as the probability of finding an atom at a separation z from the plane of the molecule within the cylindrical volume of radius r ; this distribution function is well suited to characterize the axial coordination of water molecule above and below the plane of aromatic rings (for more details see Fig. 1 of Ref. 28). We should also point out that the variable r in the CDF is the radius of the cylindrical sector and not the radius-vector of the neighbouring site (as in the SDF). The origin of the local frame for the naphthalene-water CDFs is placed on the center of each aromatic ring.

In the case with naphthalene r is set to 1.217 Å, or the radius of either aromatic ring, thus each CDF shown in this work is the average of four equivalent distributions (accounting for 2 rings and 2 directions, i.e. $+z$ and $-z$). The CDF for ring (naphthalene) – oxygen (water) pairs was used to determine the average π -coordination number, $n_{\text{Naph-O}, \pi\text{-complex}}$ (i.e. the number of water molecules located just above and below the aromatic rings), while the CDF for ring (naphthalene) - hydrogen (water) pairs was used to determine the average number of H-bonds between naphthalene and its π -coordinated water molecules, $n_{\text{HB}, \pi\text{-complex}}$.

Fig. 3.6(a) shows a series of the ring - oxygen CDFs, from 298 K to 833 K. The position of the first peak shifts from 3.1 Å at 298 K to 3.2 Å and 3.5 Å at 473 K and 633 K, respectively. At ambient temperature (298 K) the first minimum appears at 5.1 Å, shifting to smaller separations with increasing temperature. Integration up to the first minimum yields the numerical value for the average π -coordination number. With temperature the number of π -coordinated water molecules decreases from 2.3 at 298 K to about 0.34 at 633 K (see Fig. 3.5). In other words, at ambient conditions on average only 2 water molecules occupy 4 accessible regions for π -coordination near the biaromatic structure of naphthalene.

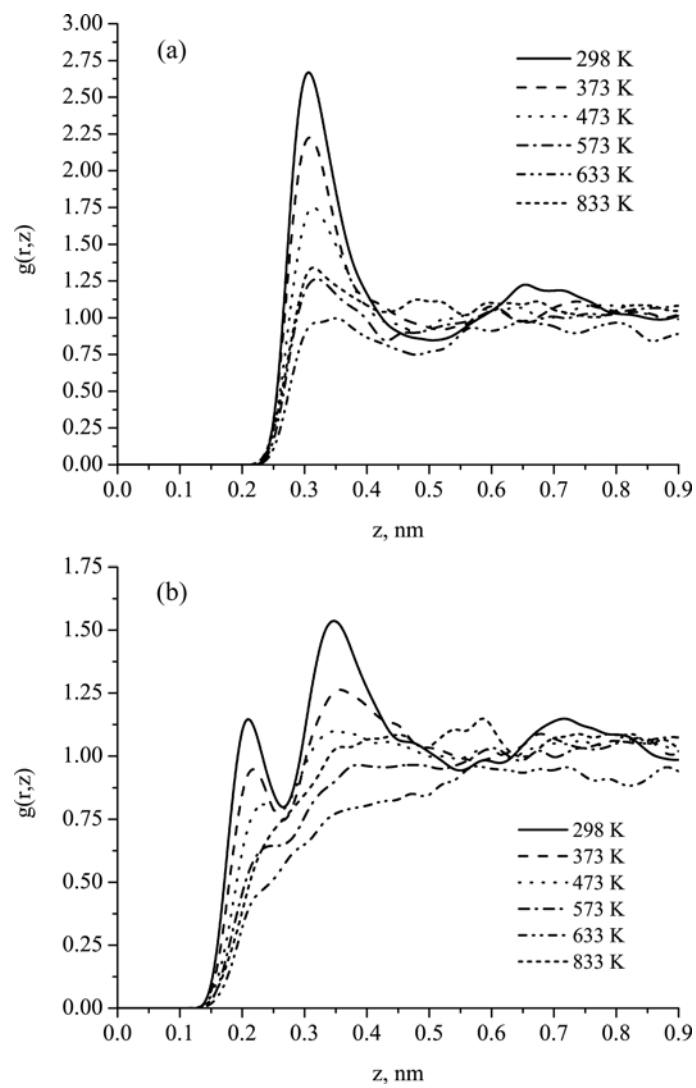


Figure 3.6 Cylindrical distribution functions of (a) oxygen and (b) hydrogen atoms of water above and below the plane of an aromatic ring of naphthalene (due to symmetry, both rings are equivalent)

Calculation and integration up to the first minimum of the ring - hydrogen CDF [Fig. 3.6(b)] yields the number of hydrogen bonds that naphthalene forms with its π -coordinated water molecules. We should point out that the first minimum in the ring - hydrogen CDF is clearly evident at temperature of 298 K at about 2.4 Å, but disappears at 373 K and higher; for this reason, the constant integration limit of 0.244 nm was used at all temperatures to estimate the number of H-bonds. At ambient temperature naphthalene is involved in roughly 0.29 π -type H-bonds per side of each aromatic ring (hence, overall naphthalene accepts 1.17 H-bonds), with this dropping to 0.03 at 633 K. This means that only about a half of the π -coordinated water molecules form H-bonds with the aromatic rings. One may also conclude that near and above the critical point of the SPC/E water the extent of this axial H-bonding to naphthalene is nearly zero. All these data can be found summarized in Fig. 3.5.

Similar analysis of the benzene-water CDFs reveals that at 298 K benzene ring π -coordinates 1.44 water molecules (0.72 molecules can be found on each side of the aromatic ring), forming overall 1.14 π -type H-bonds (0.57 H-bonds on each side of the aromatic ring). We may thus conclude that benzene is more H-bonded with water than naphthalene (per ring basis); its aromatic ring is twice more likely to accept H-bonds than each of the aromatic rings of naphthalene. No doubt, lesser H-bond accepting capacity of naphthalene greatly diminishes its solubility in water.

3.4.3 Self-Diffusion Coefficient

Aqueous molecular diffusivities of naphthalene have been measured in a range of temperatures, and the results tend to depend on the degree of dilution. Thus, for ambient conditions, Gustafson and Dickhut²⁹ report a value of $0.75 \times 10^{-9} \text{ m}^2 \text{ s}^{-1}$, while Tominaga *et al.*³⁰ give $0.94 \times 10^{-9} \text{ m}^2 \text{ s}^{-1}$, the concentration of naphthalene being 15 ppm (50 % saturation) and 1 ppm, respectively. Presumably, at a higher concentration naphthalene begins to self-associate, which increases its effective molar volume accounting for the decrease in its observed diffusion rate. As the experimental measurements are not in agreement with each other, in this work we calculate the self-diffusion coefficient of naphthalene at infinite dilution, an important property that is used in engineering practices and multimedia environmental models.³¹ The linear velocity autocorrelation function (VACF) for the center of mass of naphthalene was used to calculate its self-diffusion coefficient. Note that at lower temperatures, this VACF has a characteristic minimum occurring at about 0.61 ps, which indicates a cage effect. Above the critical point of water, the VACF decays exponentially, indicating weak intermolecular interactions. Fig. 3.7 reports the calculated self-diffusion coefficients, along with the experimental results.

Our simulated self-diffusion coefficients for naphthalene tend to correlate more closely with the experimental (1 ppm) values of Tominaga *et al.*,³⁰ particularly at lower temperatures. As the uncertainty in the simulated data for naphthalene appears to be large (around 10 % at 298K), we have compared the VACF results with those that can be obtained by analyzing the mean square displacement. The self-diffusion coefficient of naphthalene at 298 K obtained from the VACF is $1.21 \times 10^{-9} \text{ m}^2/\text{s}$, which compares well with the value of $1.15 \times 10^{-9} \text{ m}^2/\text{s}$ obtained from the mean square displacements. For water these two methods yield, respectively, 2.57 and $2.56 \times 10^{-9} \text{ m}^2 \text{ s}^{-1}$.

With temperature the self-diffusion coefficient of naphthalene increases, as expected, with a particularly dramatic rise near the critical point of water. This effect can be explained by the fact that the number of water molecules making up the hydration shell around naphthalene dramatically drops; hence, the increase in thermal motion and disruption of the H-bond network act together to liberate naphthalene from the constraint of the hydration shell.

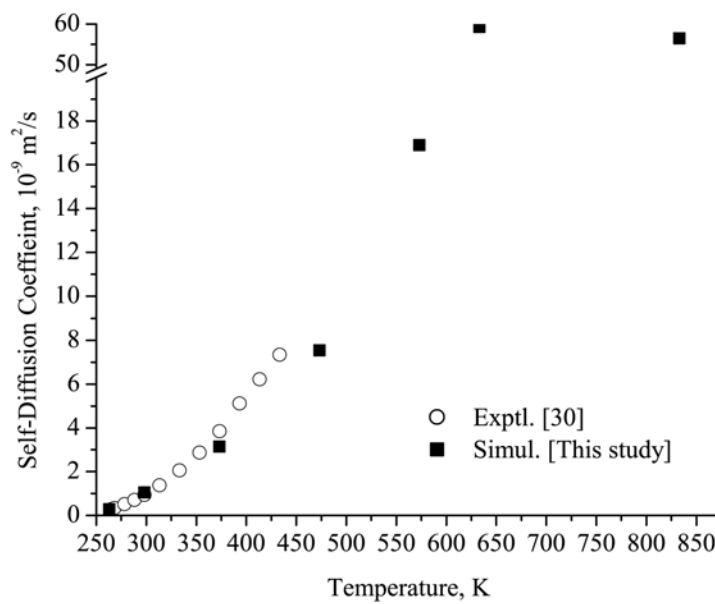


Figure 3.7 Self-diffusion coefficients for naphthalene

3.5 Conclusion

In this chapter, results have been presented from classical MD simulations of aqueous naphthalene at infinite dilution. The structure and dynamics of a simulated system along and above the coexistence curve of SPC/E water have been studied. Detailed, spatially-resolved, 3D maps of local water density around naphthalene have been obtained. These hydration maps clearly show the augmentation of local water density around the periphery of the naphthalene molecule due to the hydrophobic cage effect and the π -coordination. The total number of water molecules in the hydration shell, or the coordination number, was calculated by direct 3D integration of the local spatial pair-density distributions (the atom-atom SDFs). At ambient temperature the hydration shell of naphthalene contains, on average, 39 water molecules. Within this shell, two water molecules can be described as π -coordinating, forming close to one H-bond to the aromatic rings. The extent of π -type H-bonding to the aromatic regions in the naphthalene-water system is less than that in the benzene-water system, thus underlying naphthalene's hydrophobic nature. With increasing temperature, the hydration of naphthalene undergoes significant changes, with the loss of H-bonding and cage structure near the critical point of water. The average number of water molecules found around naphthalene at near critical and supercritical conditions (at 633 and 833 K, respectively) is around 6. These striking changes to the hydration structure affect the self-diffusion coefficient, which shows a dramatic increase near the critical point.

3.6 References for Chapter 3

1. A. Ben-Naim, *Hydrophobic Interactions* (Plenum Press, New York, 1980)
2. L. R. Pratt, *Ann. Rev. Phys. Chem.* **53**, 409 (2002)
3. D. Chandler, *Nature*, **437**, 640 (2005)
4. T.M. Raschke and M. Levitt, *J. Phys. Chem. B*, **108**, 13492 (2004)
5. S. Urahata, K. Coutinho and S. Canuto, *Chem. Phys. Lett.* **274**, 269 (1997)
6. S. Urahata and S. Canuto, *Chem. Phys. Lett.* **313**, 235 (1999)
7. W..L. Jorgensen and D.L. Severance, *J. Am. Chem. Soc.* **112**, 4768 (1990)
8. G. Ravishanker, P. K. Mehrotra, M. Mezei and D. L. Beveridge, *J. Am. Chem. Soc.* **106**, 4102 (1984)
9. P. Linse, G. Karlstrom and B. Jonsson, *J. Am. Chem. Soc.* **106**, 4096 (1984)
10. P. Linse, *J. Am. Chem. Soc.* **112**, 1744 (1990)
11. A. Laaksonen, P. Stilbs and R.E. Wasylishen, *J. Chem. Phys.* **108**, 455 (1998)
12. E.C. Meng and P. A. Kollman, *J. Phys. Chem.* **100**, 11460 (1996)
13. P. Schravendijk and N.F.A. van der Vegt, *J. Chem. Theory Comput.* **1**, 643 (2005)
14. P.T. Cummings, A.A. Chialvo and H.D. Cochran, *Chem. Eng. Sci.* **49**, 2735 (1994)
15. C.J. Gruenloh, J.R. Carney, C.A. Arrington, T.S. Zwier, S.Y. Fredericks and K.D. Jordan, *Science* **276**, 1678 (1997)
16. N.A. McDonald, H.A. Carlson and W.L. Jorgensen, *J. Phys. Org. Chem.* **10**, 563 (1997)

17. S. Tsuzuki, K. Honda, T. Uchimaru and M. Mikami, *J. Chem. Phys.* **120**, 647 (2004)
18. K.J. Shinoda, *J. Phys. Chem.* **81**, 1300 (1977)
19. D. Evans and P.J. Wightmann, *Colloid Interface Sci.*, **71**, 147 (1979)
20. D. Evans, M. Allen, B. Ninham and A. Fouda, *J. Solution Chem.* **13**, 87 (1984)
21. H.J.C. Berendsen, J.R. Grigera and T.P. Straatsma, *J. Phys. Chem.* **91**, 6269 (1987)
22. G.C. Boulougouris, I.G. Economou and D.N. Theodorou, *J. Phys. Chem. B* **102**, 1029 (1998)
23. T.M. Hayward and I.M. Svishchev, *Fluid Phase Equilib.* **182**, 65 (2001)
24. D.J. Evans and J.P. Morriss, *Comput. Phys. Rep.* **1**, 297 (1984)
25. D. J. Evans, *Mol. Phys.* **34**, 317 (1977)
26. I.M. Svishchev and P.G. Kusalik, *J. Chem. Phys.* **99**, 3049 (1993)
27. A. Soper, *J. Chem. Phys.* **101**, 6888 (1994)
28. A. Plugatyr, I. Nahtigal and I.M. Svishchev, *J. Phys. Chem.* **124**, 24507 (2006)
29. K.E. Gustafson and R.M. Dickhut, *J. Chem. Eng. Data*, **39**, 281 (1994)
30. T. Tominaga, S. Matsumoto and T.J. Ishii, *Phys Chem.*, **90**, 139 (1986)
31. D. Mackay, *Multimedia Environmental Models: The Fugacity Approach* (Lewis Publishers, Michigan, 1991)

Chapter 4

The Hydration of Aniline: Analysis of Spatial Distribution Functions

4.1 Abstract

Molecular dynamics simulations of aniline in aqueous infinitely dilute solution are performed from ambient to supercritical conditions. Spatial hydration structures of aniline are examined along the liquid-vapour coexistence curve of water at 298, 373, 473, 573 and 633 K and above the critical point at 733 and 833 K with density fixed at 0.3 g/cm^3 . The coordination and H-bond numbers of aniline are calculated. The self-diffusion coefficient of aniline is also evaluated. The hydration structures of aniline at high temperatures are drastically different from those in ambient water. At room temperature the solvation shell of aniline is comprised of approximately 32 water molecules, whereas above the critical point aniline forms a complex with about 8 water molecules. We find that in ambient water the lone pair of nitrogen of the amino group is hydrated by one water molecule, with which it forms one H-bond. The amino hydrogens are hydrated by approximately one water molecule each, but form, on average, 0.6 H-bonds (each). The results also indicate the formation of weak H-bonded π -complexes between hydrogen of water and the aromatic ring of aniline.

4.2 Introduction

Over the last two decades, near-critical water has attracted much attention as a promising medium for a variety of technological applications such as power generation, hazardous waste utilization, materials processing, etc.¹⁻⁶ The development and optimization of these technologies requires thorough examination of complex properties of near-critical aqueous solutions. Understanding the effect of *solvent* on the diffusivity and reactivity of *solutes* at sub- and supercritical water conditions is of particular interest. The loss of the extended H-bonded structure of water at near critical conditions enhances the diffusivity of solutes. On the other hand, the disappearance of the solvent “cage” affects reaction kinetics as the number of collisions per encounter decreases from “multiple” at ambient conditions to a “single” event in a low-density supercritical water. The interplay between these two factors is particularly pronounced for rates of near-diffusion-controlled reactions which exhibit non-Arrhenius behaviour (with negative temperature dependence) in the range of about 423 to 623 K.⁷⁻¹³ Systematic studies of molecular dynamics and hydration structures are clearly warranted to provide a detailed understanding of the chemical reaction mechanisms in water at near-critical conditions.

From a chemical perspective, the information about mass transport coefficients and hydration structures of the reacting species is essential for estimation of the diffusion-controlled limit via the Smoluchowski equation. Unfortunately, very little is known about diffusivity of organic solutes at near and above the critical point of water.¹⁴⁻¹⁷ Furthermore, the simple hydrodynamic (Stokes-Einstein-Debye) approach, commonly used for the calculation of the mass transport coefficients at ambient conditions, does not adequately describe the behaviour of the self-diffusion coefficient of water at near and above its critical point.^{18,19}

In this study, we examine solvation structures and self-diffusion coefficients of aniline in aqueous infinitely dilute solution from ambient to supercritical conditions. Aniline is an important model system which allows for the study of both hydrophilic and hydrophobic hydration. Small gas-phase aniline-water complexes have been previously examined by several research groups²⁰⁻²². Piani *et al.*²² and Spoerel and Stahl²⁰ have studied the properties of the 1:1 aniline–water complex. The results indicate that in this complex water is H-bonded to aniline with the interaction taking place at the lone pair of the nitrogen. Inokuchi *et al.*²¹ have studied infrared photodissociation spectra of [aniline-(H₂O)_{*n*}]⁺ (*n* = 1-8) complexes which were interpreted with the aid of DFT calculations. The authors show that for *n* = 2, water forms 1-1 H-bonded structure with each amino hydrogen of aniline, whereas for *n* = 3, a 2-1 branched complex was reported.

A number of computer simulation studies, focused on the properties of aqueous amine solutions,²³⁻³⁰ indicate that at ambient conditions the amino group is coordinated to about three water molecules and exhibits much better H-bond accepting than H-bond donating character.^{23,25,27-29}

The goal of this study is to examine the hydration structure and diffusivity of aniline from ambient to supercritical water conditions. The remainder of the chapter is organized as follows. Computational details are described in Section 4.2. Simulation results are discussed in Section 4.3. Our conclusions are given in Section 4.4.

4.3 Simulation Details

In this study the Simple Point Charge Extended³¹ (SPC/E) water model was used. The rigid point charge interaction potential for aniline, based on the OPLS force field, was taken from work of Jorgensen and co-workers.²⁷ The geometry, charges and Lennard-Jones (LJ) parameters are given in Table 4.1.

MD simulations were carried out in the *NVT* ensemble along the liquid side of the coexistence curve of the SPC/E water at 298, 373, 473 and 573 with the corresponding densities being 1.00, 0.96, 0.87 and 0.67 g/cm³, respectively. In the supercritical region simulations were performed at 633, 733 and 833 K with density fixed at 0.30 g/cm³. The system size was 503 waters and 1 aniline molecule. The isokinetic equations of motion were integrated using the fourth-order Gear algorithm³² with time step of 1 fs. Rotational equations of motion were represented using quaternions.³³ The equilibrated simulation run lengths were 500 ps. The long-range Coulomb forces were handled by means of Ewald sums in cubic periodic boundary conditions. The cutoff distance for the LJ interactions was set at half of the simulation cell length. The translational diffusion coefficient was calculated from the velocity autocorrelation function (VACF). The simulations were carried out on a Linux-based parallel Transport GX28 system with dual 64 bit AMD Opteron processors.

Table 4.1 Electrostatic, geometric, and Lennard-Jones parameters for water and aniline models.

<i>Species</i>	<i>Atom</i>	ϵ (kcal/mol)	σ (Å)	q (e)	R (Å)	\angle (deg)
H ₂ O ^a	H	0.0000	0.0000	0.4238		109.47 (H-O-H)
	O	0.1554	3.1660	-0.8476	1.000	
C ₆ H ₅ NH ₂ ^b	C _{ipso}	0.070	3.550	0.180	1.400 (C=C)	120.0 (CCC)
	C _A	0.070	3.550	-0.115	1.080 (C-H)	120.0 (CCH)
	H _A	0.030	2.420	0.115	1.430 (C-N)	120.0 (CCN)
	N	0.170	3.300	-0.900	1.010 (N-H)	111.0 (CNH)
	H(N)	0.000	0.000	0.360		106.4 (HNH)

^a Ref. [31]; ^b Ref. [27].

4.4 Results and Discussion

In this study we employ the radial, cylindrical and spatial distribution functions to examine the details of the hydration of aniline molecule. The spatial distribution function³⁴ (SDF), or $G(r, \mathbf{\Omega})$, accounts for both radial, r , and angular components, $\mathbf{\Omega} = (\theta, \varphi)$, of the site-site separation vector \mathbf{R} and is best suited for characterization of complex spatially anisotropic interactions between molecular species.^{16, 17, 30, 35-39}

The primary structure of water around aniline at ambient conditions is shown in Fig. 4.1. The hydrating water molecules form, as expected, both H-bond donating and H-bond accepting pairs with the amino group. Two pairs of cups along the direction of the N-H bonds are due to H-bond accepting water molecules, whereas elongated features located below the nitrogen are due to H-bond donating water molecules. In addition, water tends to form a π -type complex with the aromatic region of aniline, as indicated by the presence of a pair of contours directly above and

below the center of the aromatic ring, see Fig. 4.1. The hydration shell of aniline at low probability levels is drawn in Fig. 4.2. This figure illustrates the general shape of the hydrophobic shell around aniline.

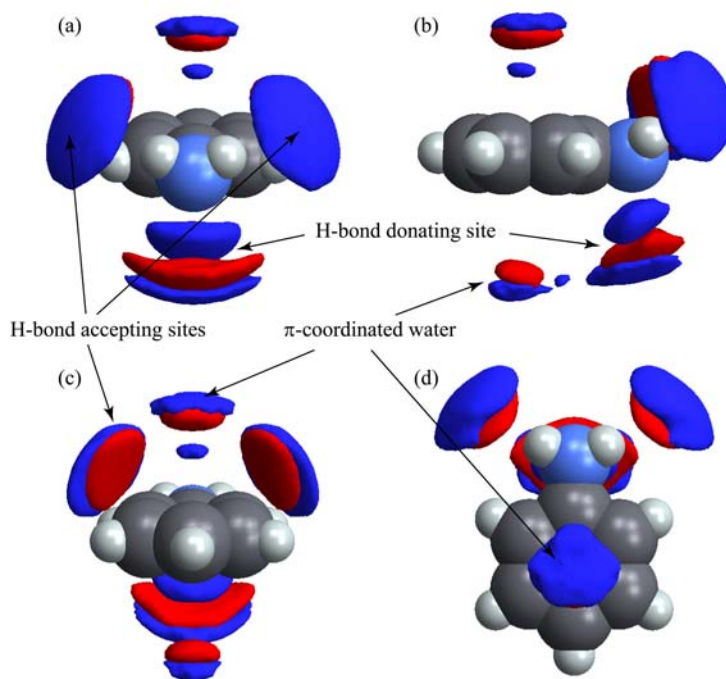


Figure 4.1 The SDF of water around central aniline molecule at 298 K. Local atomic densities of oxygen (red) and hydrogen (blue) of water are shown at probability levels of $G_O(r, \Omega) = 2.5$ and $G_H(r, \Omega) = 1.8$, respectively. (a) front view; (b) side view; (c) rear view; (d) top view.

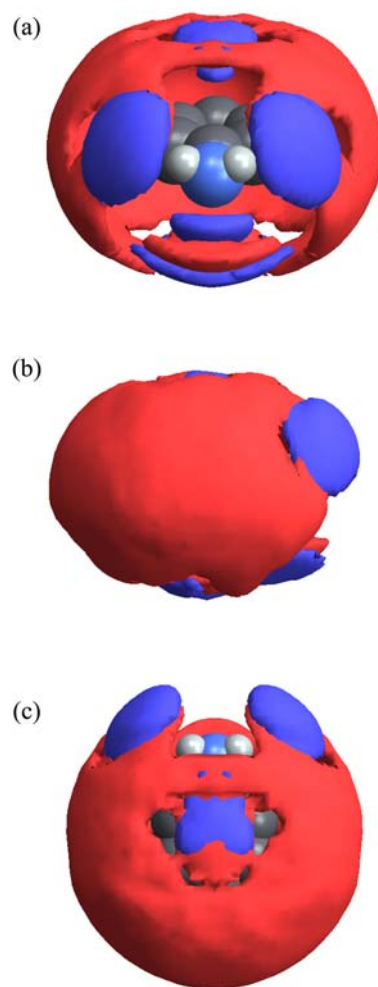


Figure 4.2 The SDF of water around central aniline molecule at 298 K. Local atomic densities of oxygen (red) and hydrogen (blue) of water are shown at probability levels of $G_O(r, \Omega) = 1.65$ for oxygen and $G_H(r, \Omega) = 1.55$ for hydrogen atoms of water, respectively. (a) front view; (b) side view; (c) top view.

Details of the hydration structure of aniline can be clearly seen in Fig. 4.3, which displays 2D density maps (cuts through the 3D spatial distributions) of oxygen, hydrogen and charge probability densities in the three orthogonal planes with respect to the symmetry of aniline molecule. The charge probability density, $\mathbf{G}_q(\mathbf{r}, \boldsymbol{\Omega})$, was obtained by combining the aniline-oxygen SDF, $\mathbf{G}_O(\mathbf{r}, \boldsymbol{\Omega})$, and the aniline-hydrogen SDF, $\mathbf{G}_H(\mathbf{r}, \boldsymbol{\Omega})$:

$$\mathbf{G}_q(\mathbf{r}, \boldsymbol{\Omega}) = q_O \cdot \mathbf{G}_O(\mathbf{r}, \boldsymbol{\Omega}) + 2 \cdot q_H \cdot \mathbf{G}_H(\mathbf{r}, \boldsymbol{\Omega}), \quad (4.1)$$

where q_O and q_H are the partial charges on oxygen and hydrogen atoms of water. Fig. 4.3 clearly illustrates the most probable location and orientation of H_2N - and π -coordinated water molecules in the first hydration shell of aniline. In addition to relatively strong coordination of water molecules around the amino group and the π -region, shown with darker colors, Fig. 4.3 also reveals the details of the secondary, more distant features of water structure in the vicinity of the amino group. Thus, the ridge spanning around the amino group at distances from 3.5 Å to about 3.9 Å (see Fig. 4.3(a,c), X-Z projections) is due to the presence of a bridging water²⁸, which, arguably, is H-bonded to both neighbours occupying H-bond accepting sites. The charge density maps, Fig. 4.3(c), show details of the electrostatic environment around aniline and allow for discerning those features of the hydration structure that might not be visible on atomic density distributions. Thus, Fig. 4.3(c) illustrates the layered structure of the hydration shells of aniline characterized by alternating hydrogen-oxygen densities. Note that the inner and outer layers of the first hydration shell consist of primarily hydrogen atoms of water, with oxygen located in-between.

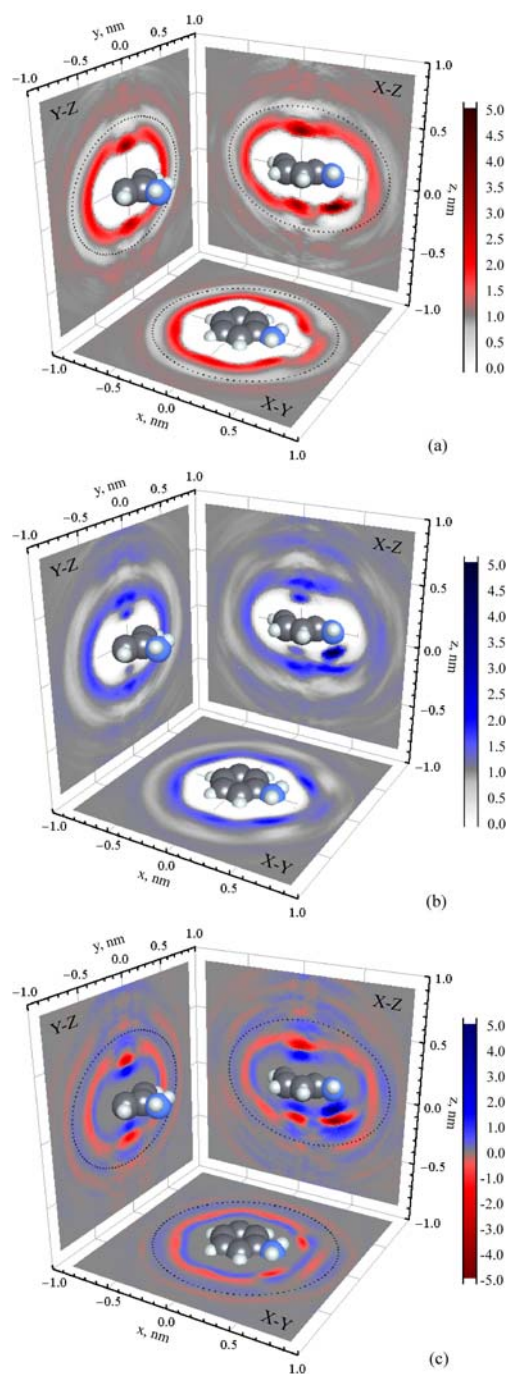


Figure 4.3 2D maps of local (a) oxygen, (b) hydrogen and (c) charge probability densities of water around aniline at 298 K. Color depths represent probability level. The boundary of the first hydration shell is shown by the dashed line.

The results of previous studies on methylamine^{23,28} indicate that the amino group is coordinated to about three water molecules with which it forms approximately two (apparently strong) hydrogen bonds. The nature of the third water molecule is somewhat unclear. Based on the analysis of the RDFs, Dunn and Nagy²³ have speculated that the third “non-hydrogen bonded” water forms a bridge between the two other H-bonded neighbours. Kusalik²⁸ having examined both RDFs and SDFs, concluded that the bridging water feature, clearly resolved in the nitrogen-oxygen SDF (see Fig.8 of Ref [28]), is located too far from the nitrogen, and therefore cannot be accounted as the extra water molecule. According to Kusalik²⁸, the nitrogen accepts a single strong H-bond from water, while water, in return, accepts only one strong H-bond from the amino group, where H-bond accepting water (located at the appropriate separation of 2.8 Å) occupies only one of the two H-bond accepting cups (see Fig. 4.1) at any instant in time. The second cup is occupied by a slightly more distant water molecule that is H-bonded to the local hydration structure.

It should be mentioned that previous discussions in literature are based on the analysis of the nitrogen-oxygen RDF, which shows a distinct first maxima at about 2.83-2.85 Å corresponding to apparently strong N-H ...O and N ...H-O hydrogen bonds. The analysis of the nitrogen-oxygen SDF, obtained in this study, indicates that the maxima of the probability density for the oxygen of the H-bond donating water site is located somewhat closer to the nitrogen than that of the H-bond accepting water. In order to obtain an unambiguous picture we have used the nitrogen-oxygen SDF to compute the radial distribution function of oxygen atoms above and below the plane of the aniline molecule, Fig. 4.4(a). The results clearly illustrate that the total $g_{N-O}(r)$ is, in fact, a combination of two different distributions. The below-the-plane $g_{N-O}(r)$, which is due to the H-bond donating water, is characterized by a sharp peak located at 2.8 Å with corresponding minima at 3.24 Å, and does indicate the presence of a strong H-bond. The above-

the-plane RDF (H-bond accepting neighbours) shows a broad first peak with maxima and minima shifted to 2.98 Å and 4.4 Å, respectively, and therefore suggests a weaker H-bond. Averaging of these two RDFs yields the first maximum at 2.83 Å with minimum at 3.42 Å, which is in agreement with previous results.^{23,28} Fig. 4.4(b) shows a complementary set of N-H(w) and H(N)-O RDFs. The position and shape of the first peak in $g_{\text{N-H(w)}}(r)$ with maxima and deep minima (~ 0.1) located at 1.8 Å and 2.39 Å confirms the presence of a strong H-bond between the hydrogen of water and the nitrogen. Note, that relative positions of the first peaks in $g_{\text{N-O}}(r)$ and $g_{\text{N-H(w)}}(r)$ at 2.8 Å and 1.8 Å, respectively, suggest a linear H-bond. At the same time, the $g_{\text{(N)H-O}}(r)$ is characterized by the first maximum at about 2.0 Å with the minimum (~ 0.4) at 2.4 Å. Thus, the H-bond accepting sites appear to be shifted farther away by about 0.2 Å from the norm for a strong H-bond location. Analysis of the coordination numbers reveals that the lone pair of nitrogen is hydrated by one water molecule with which it forms one strong linear H-bond. Integration of the $g_{\text{H(N)-O}}(r)$ and the above-the-plane $g_{\text{N-O}}(r)$ up to 3.44 Å (actual location of the minima is difficult to discern due to overlapping secondary structure features) indicates that each H-bond accepting cup contains close to one water molecule, forming in total, two weak (0.6) H-bonds with the hydrogens of the amino group. In the analysis of coordination numbers for water molecules located in the π -region of aniline, we have employed the cylindrical distribution function (CDF) proposed by Plugatyr *et al.*¹⁶ The CDF is well suited for characterization of the local atomic density around planar surfaces.^{16,17} The CDFs of the oxygen, $g_{\text{X-O}}(r,z)$, and hydrogen, $g_{\text{X-H}}(r,z)$, atoms of water in aniline's aromatic region are shown in Fig. 4.5. Note, that positive z values correspond to pair distributions above the plane of aniline as defined in Fig. 4.1(a-c). At 298K, the oxygen CDF, Fig. 4.5(a), is characterized by the first peaks located at $|z| = 3.2$ Å with the corresponding minima at $|z| = 5.1$ Å. The total number of π -coordinated water molecules at ambient conditions was determined to be 1.53. The hydrogen CDF, given in Fig. 4.5(b), suggests

the presence of weak π -type H-bonds between hydrogen atoms of water and the aromatic ring, as indicated by small peaks centered at $|z| = 2.3 \text{ \AA}$ with minima at $|z| = 2.7 \text{ \AA}$. At 298 K the total number of π -type H-bonds was determined to be 0.75. Note, that the strong coordination of water molecules around the amino group of aniline affects the distribution of water molecules in the π -region, as indicated by slightly asymmetric peaks ($\sim 10 \%$) below and above the plane of aniline, Fig.4.5.

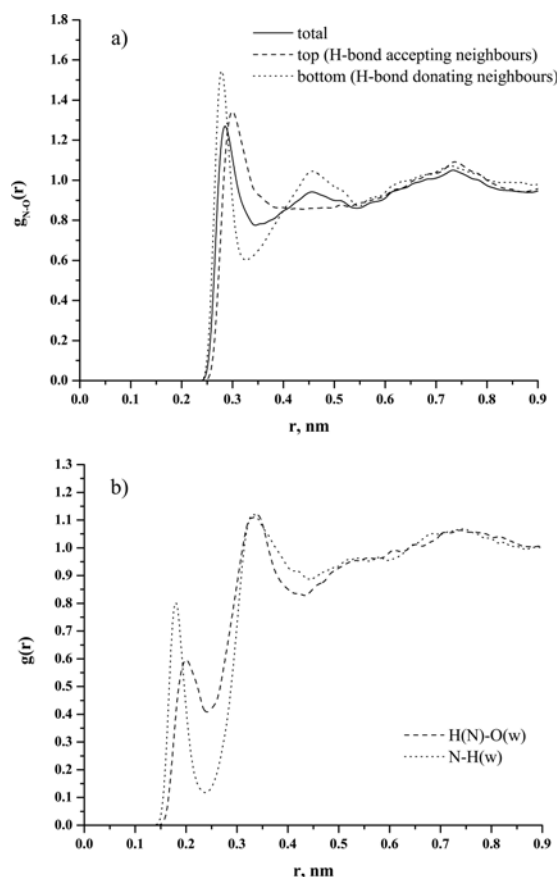


Figure 4.4 Radial distribution functions between a) nitrogen – oxygen (water) and b) hydrogen (amino) – oxygen (water) and nitrogen-hydrogen (water) in aqueous aniline solution at 298 K.

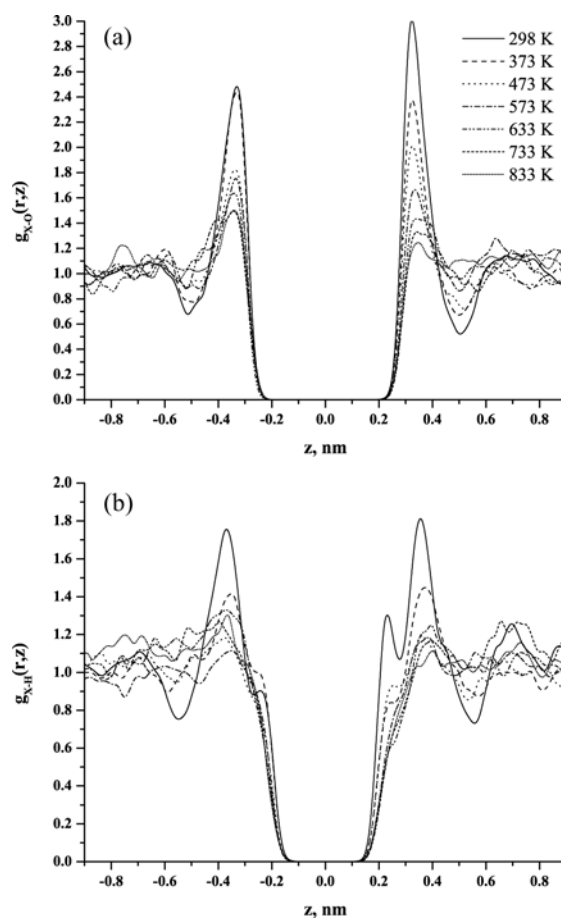


Figure 4.5 Cylindrical distribution functions of (a) oxygen and (b) hydrogen atoms of water in the axial region of the benzene ring of aniline. The origin of the local frame is at the center of the benzene ring of aniline. The radius of the cylindrical sector is 1.4 Å.

The total coordination number of aniline was calculated from a triple integral of the aniline-oxygen SDF over the volume occupied by its hydration shell. As in our previous study¹⁷, the boundary of the hydration shell was determined by minimizing the average value of the $G_O(r, \Omega)$ on the surface of an ellipsoid. The outer boundary of the first hydration shell of aniline is shown in Fig. 4.3(a) by a dashed line. At ambient conditions the total coordination number of aniline was calculated to be approximately 32.

The changes in the primary hydration structure of aniline with temperature are illustrated in Figs. 4.5 and 4.6. As expected all peaks broaden and shift to larger distances. An apparent increase in the coordination number of the amino group at 373 and 473 K, see Fig. 4.7, is due to the shift of the position of the first minima in $g_{N-O}(r)$ from 3.42 Å at 298 K to 3.90 Å at 473 K. The total number of H-bonds with the amino group decreases from about 1.9 at 473 K to 0.82 at 633K and further to 0.55 at 833 K. The number of water molecules in π -coordination drops from 1.53 at ambient conditions to less than 0.3 at 833K. The disappearance of the pronounced minima in aniline-hydrogen CDF is noted at 473 K, Fig. 4.5(b). The number of π -type H-bonds at 473K and above was calculated by integrating the corresponding CDF up to 2.7 Å and yielded 0.47 and 0.13 at 473 and 633, respectively. The overall coordination number of aniline decreases from 26.5 at 473 K to about 8 water molecules at supercritical conditions. These changes in the hydration structure can be clearly seen in Fig. 4.8 and 4.9, which show local probability density maps at 473 and 633 K, respectively. Note almost complete disappearance of the solvation shell around aniline near the critical point of water, Fig. 4.9.

The self-diffusion coefficient of aniline was calculated from the linear velocity autocorrelation function (VACF). The relative uncertainty was estimated to be approximately 10%. The results are shown in Fig. 4.10. The value of the self-diffusion coefficient at 298 K was determined to be $0.992 \times 10^{-9} \text{ m}^2/\text{s}$, which compares well with the experimental value of $1.050 \times 10^{-9} \text{ m}^2/\text{s}$ reported by Niesner and Heintz⁴⁰. As expected, the self-diffusion coefficient of aniline increases with temperature. A dramatic rise in diffusivity of aniline is observed near the critical point of water. Such behaviour is due to the combined effects of increased thermal motion and disappearance of the H-bonded structure in supercritical water.

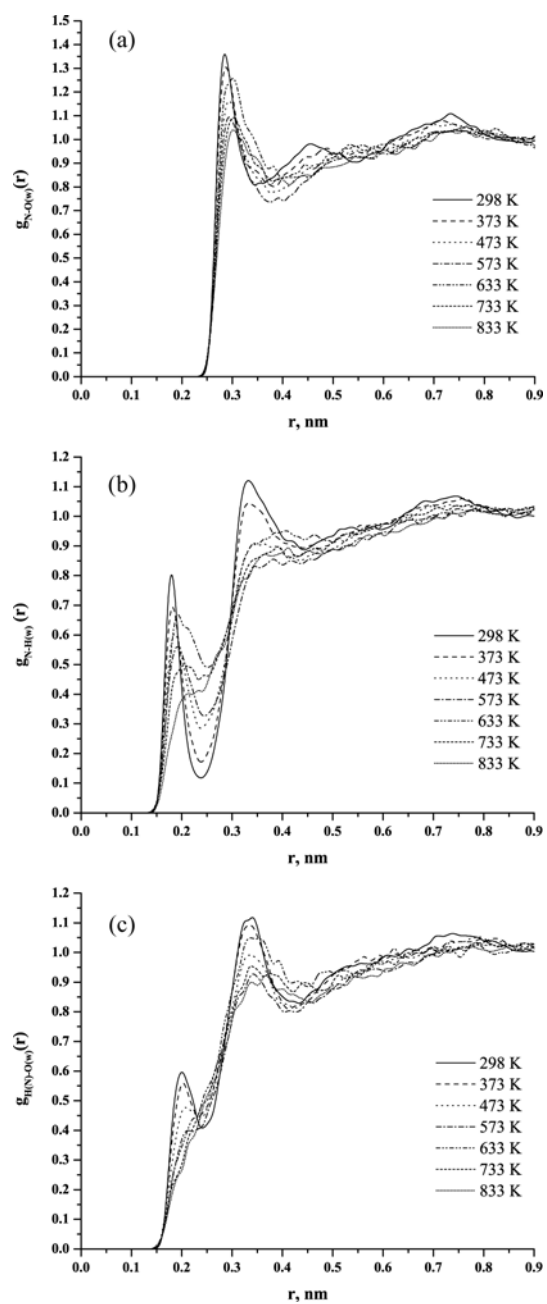


Figure 4.6 Radial distribution functions between a) nitrogen-oxygen and b) nitrogen-hydrogen (water) and hydrogen (amino) – oxygen in aqueous aniline solution.

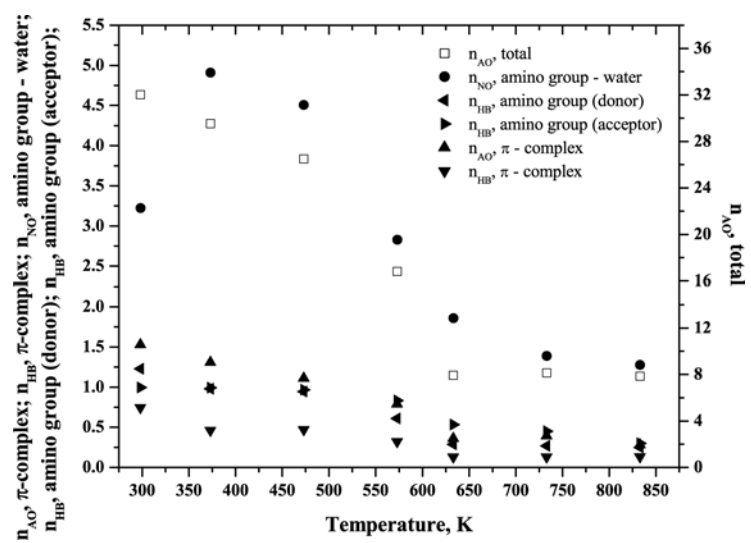


Figure 4.7 Coordination numbers and number of H-bonds for aniline.

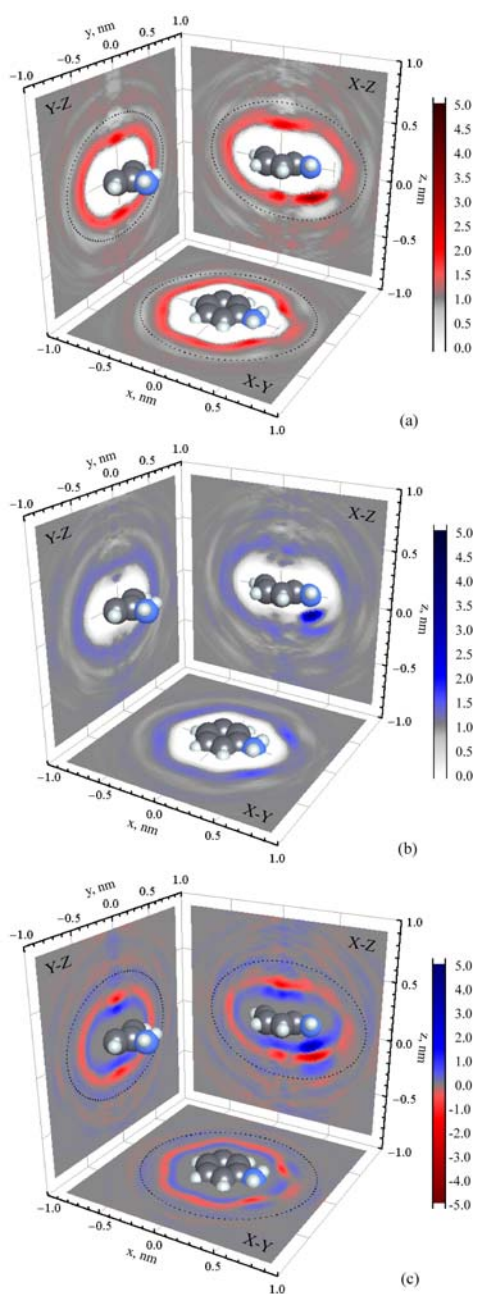


Figure 4.8 2D maps of local (a) oxygen, (b) hydrogen and (c) charge probability densities of water around aniline at 473 K. Color depths represent probability level. The boundary of the first hydration shell is shown by the dashed line.

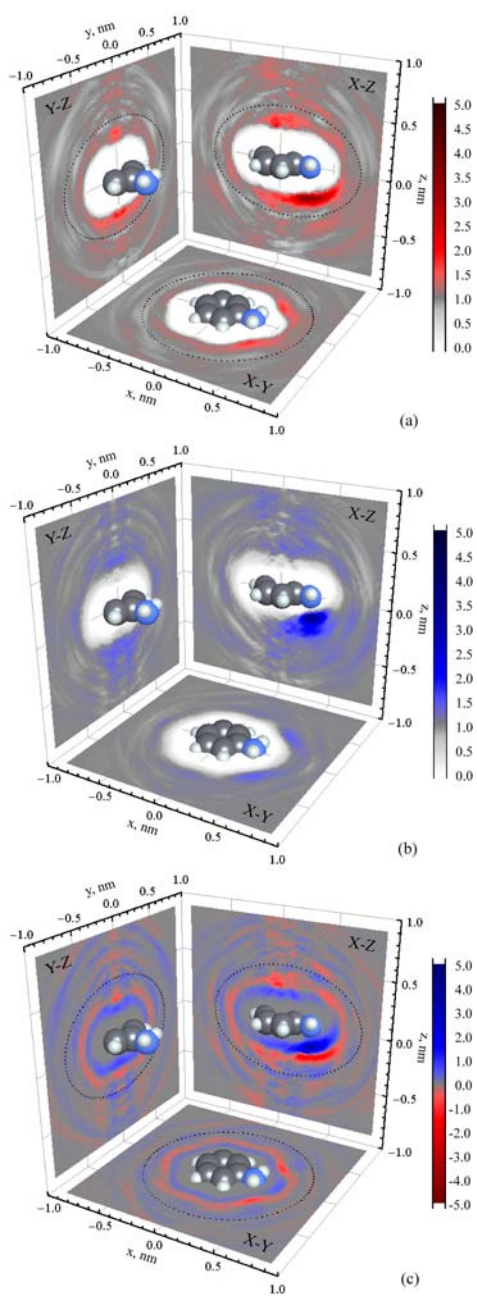


Figure 4.9 2D maps of local (a) oxygen, (b) hydrogen and (c) charge probability densities of water around aniline at 633 K. Color depths represent probability level. The boundary of the first hydration shell is shown by the dashed line.

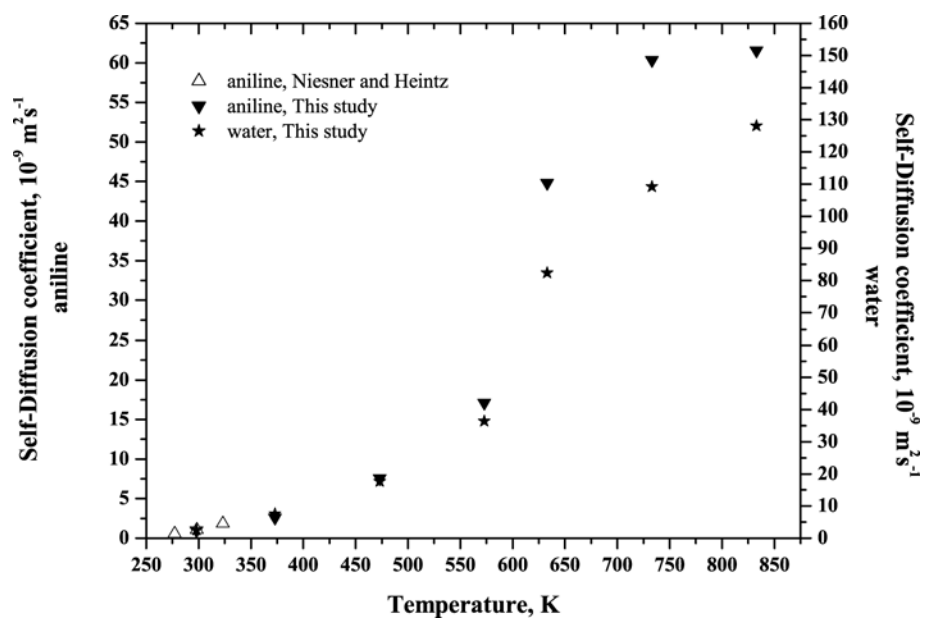


Figure 4.10 Self-diffusion coefficient of aniline in aqueous infinitely dilute solution.

4.5 Conclusion

MD simulations of aqueous aniline at infinite dilution were carried out along the coexistence curve of water up to the critical point of water and above the critical point with density fixed at 0.3 g/cm^3 . The spatial structure of water around the aniline molecule was calculated and analysed in detail. The results indicate that at ambient conditions the first hydration shell of aniline is comprised of about 32 water molecules. The amino group is coordinated to about three water molecules by accepting one strong and donating two weak (0.6) H-bonds. In addition, approximately 1.53 water molecules participate in the formation of a π -type complex with the aromatic region of aniline. The total number of π -H-bonds was calculated to be about 0.75 at 298K. As temperature increases, the hydration structure undergoes significant changes. The disappearance of the solvent “cage” is noted near the critical point of water. At 633 K aniline is solvated by only 8 water molecules, 1.86 of which are coordinated with the amino group, forming about 0.82 H-bonds in total. The changes in the hydration structure with temperature (and density) are reflected in the value of the self-diffusion coefficient of aniline which shows a dramatic rise near the critical point of water.

4.6 References for Chapter 4

1. M. D. Bermejo and M. J. Cocero, *AIChE J.* **52** (11), 3933 (2006).
2. A. Kruse and E. Dinjus, *J. Supercrit. Fluids* **39** (3), 362 (2007).
3. A. Kruse and E. Dinjus, *J. Supercrit. Fluids* **41** (3), 361 (2007).
4. A. Kruse and H. Vogel, *Chem. Eng. Technol.* **31** (9), 1241 (2008).
5. Ph. MacDonald, J. Buongiorno, J.W. Sterbentz, C. Davis and R. Witt, "Feasibility Study of Supercritical Light Water Cooled Reactors for Electric Power Production", Nuclear Energy Research Initiative Project 2001-001 INEEL/EXT-04-02530.
6. J. Kronholm, K. Hartonen and M.-L. Riekkola, *Trac.-Trends Anal. Chem.* **26** (5), 396 (2007).
7. K. Takahashi, D.M. Bartels, J.A. Cline and C.D. Jonah, *Chem. Phys. Lett.* **357** (5-6), 358 (2002).
8. J. Cline, K. Takahashi, T.W. Marin, C.D. Jonah and D.M. Bartels, *J. Phys. Chem. A* **106** (51), 12260 (2002).
9. T.W. Marin, J.A. Cline, K. Takahashi, D.M. Bartels and C. D. Jonah, *J. Phys. Chem. A* **106** (51), 12270 (2002).
10. K. Ghandi, B. Addison-Jones, J.C. Brodovitch, I. McKenzie, P.W. Percival and J. Schuth, *Phys. Chem. Chem. Phys.* **4** (4), 586 (2002).
11. K. Ghandi and P.W. Percival, *J. Phys. Chem. A* **107** (17), 3005 (2003).
12. I. Janik, D.M. Bartels and C.D. Jonah, *J. Phys. Chem. A* **111** (10), 1835 (2007).
13. J. Bonin, I. Janik, D. Janik and D. M. Bartels, *J. Phys. Chem. A* **111** (10), 1869 (2007).

14. T. Ohmori and Y. Kimura, *J. Chem. Phys.* **119** (14), 7328 (2003).
15. C. Nieto-Draghi, J.B. Avalos, O. Contreras, P. Ungerer and J. Ridard, *J. Chem. Phys.* **121** (21), 10566 (2004).
16. A. Plugatyr, I. Nahtigal and I.M. Svishchev, *J. Chem. Phys.* **124** (2), 024507 (2006).
17. I.M. Svishchev, A. Plugatyr and I.G. Nahtigal, *J. Chem. Phys.* **128** (12), 124514 (2008).
18. W.J. Lamb, G.A. Hoffman and J. Jonas, *J. Chem. Phys.* **74** (12), 6875 (1981).
19. K. Yoshida, C. Wakai, N. Matubayasi and M. Nakahara, *J. Chem. Phys.* **123** (16), 164506 (2005).
20. U. Spoerel and W. Stahl, *J. Molec. Spectrosc.* **190** (2), 278 (1998).
21. Y. Inokuchi, K. Ohashi, Y. Honkawa, N. Yamamoto, H. Sekiya and N. Nishi, *J. Phys. Chem. A* **107** (21), 4230 (2003).
22. G. Piani, M. Pasquini, I. Lopez-Tocon, G. Pietraperzia, M. Becucci and E. Castellucci, *Chem. Phys.* **330** (1-2), 138 (2006).
23. W.J. Dunn and P.I. Nagy, *J. Phys. Chem.* **94** (5), 2099 (1990).
24. W.J. Dunn, P.I. Nagy and E.R. Collantes, *J. Am. Chem. Soc.* **113** (21), 7898 (1991).
25. E.C. Meng, J.W. Caldwell and P.A. Kollman, *J. Phys. Chem.* **100** (6), 2367 (1996).
26. M.M. Kubo, E. Gallicchio and R.M. Levy, *J. Phys. Chem. B* **101** (49), 10527 (1997).
27. R.C. Rizzo and W.L. Jorgensen, *J. Am. Chem. Soc.* **121** (20), 4827 (1999).
28. P.G. Kusalik, D. Bergman and A. Laaksonen, *J. Chem. Phys.* **113** (18), 8036 (2000).
29. A.V. Gubskaya and P.G. Kusalik, *J. Phys. Chem. A* **108** (35), 7165 (2004).

30. P. Jedlovszky and A. Idrissi, *J. Chem. Phys.* **129** (16), 164501 (2008).
31. H.J.C. Berendsen, J.R. Grigera and T.P. Straatsma, *J. Phys. Chem.* **91** (24), 6269 (1987).
32. D.J. Evans and O.P. Morriss, *Comput. Phys. Rep* **1** (6), 297 (1984).
33. D.J. Evans, *Mol. Phys.* **34** (2), 317 (1977).
34. P.G. Kusalik and I.M. Svishchev, *Science* **265** (5176), 1219 (1994).
35. A. Laaksonen, P. Stilbs and R.E. Wasylshen, *J. Chem. Phys.* **108** (2), 455 (1998).
36. K.S. Sidhu, J.M. Goodfellow and J.Z. Turner, *J. Chem. Phys.* **110** (16), 7943 (1999).
37. P.G. Kusalik, A.P. Lyubartsev, D.L. Bergman and A. Laaksonen, *J. Phys. Chem. B* **104** (40), 9526 (2000).
38. T.M. Raschke and M. Levitt, *J. Phys. Chem. B* **108** (35), 13492 (2004).
39. D.T. Bowron, J.L. Finney and A.K. Soper, *J. Phys. Chem. B* **110** (41), 20235 (2006).
40. R. Niesner and A. Heintz, *J. Chem. Eng. Data* **45** (6), 1121 (2000).

Chapter 5

Accurate Thermodynamic and Dielectric Equations of State for High-Temperature Simulated Water

5.1 Abstract

The thermodynamic and dielectric properties of the Simple Point Charge Extended (SPC/E) water model are examined over wide temperature and density range by means of molecular dynamics simulations. Accurate analytical thermodynamic and dielectric equations of state for the SPC/E pair-potential are presented. Parameterizations cover a broad range of high temperature states including the critical region. The critical point parameters of SPC/E water were determined to be $\rho_c = 0.276 \text{ g/cm}^3$, $T_c = 640.25 \text{ K}$ and $p_c = 164.37 \text{ bar}$. The value of the static dielectric constant, ϵ , of SPC/E water at its critical point was calculated to be 5.35, which compares remarkably well with the corresponding experimental value of 5.36 [D.P. Fernandez *et al.*, *J. Phys. Chem. Ref. Data* **26**, 1125 (1997)]. Analytical thermodynamic and dielectric equations for the saturated liquid and vapour densities are also given.

5.2 Introduction

The behaviour of aqueous systems at elevated temperatures and pressures has become a topic of extensive research over the past few years. Knowledge of the thermodynamic, dielectric and transport properties of high temperature and supercritical water and aqueous fluids is very important for the continuing development of many essential technological processes like power generation, waste destruction, materials synthesis, etc.¹⁻⁵ Of special interest for current high temperature research is a novel combined GEN IV nuclear power cycle which utilizes supercritical water coolant for in-core and out-of-core components, leading to a significant improvement in energy efficiency.⁶

At present, computer simulations provide most of the information about the molecular level physical-chemical processes occurring in water at extreme conditions. However, the results are often difficult to interpret as the simulated fluid differs from the real substance in its phase coexistence properties and critical point parameters. It is important to emphasize that accurate knowledge of the thermodynamic behaviour of a model system is crucial for the determination of the corresponding states which allows for direct comparison of simulation data and experimental results. Considering the interest simulations can have for power and chemical industries, and for geochemistry, there exists a great practical need for the development of accurate equations of state for computer simulated water.

One of the most widely used pair-potentials for water is the SPC/E water model of Berendsen *et al.*⁷ The thermodynamic properties of this model has been reported in a number of publications.⁸⁻¹³ These studies were primarily focused on elucidation of the coexistence properties of the SPC/E pair-potential. The dielectric properties of the SPC/E model have been examined by Guissani and Guillot⁸, Wasserman *et al.*¹⁴, Neumann¹⁵, Mountain and Wallqvist¹⁶, Skaf and

Laria¹⁷, Guàrdia and Martí¹⁸ and others. Despite its simplicity, the overall results indicate that the SPC/E water model describes fairly well the critical parameters of real water, its liquid-vapour coexistence curve and the behaviour of the dielectric constant. These findings make SPC/E model a very attractive pair-potential for simulating high temperature and supercritical states of water and aqueous solutions.

The first thermodynamic EOS for the SPC/E water was proposed by Guissani and Guillot⁸ who used the expression for the compressibility factor to describe the $p\rho T$ surface. Later, Hayward and Svishchev¹³ have parameterized the Pitzer-Sterner¹⁹ EOS for SPC/E water. Both EOS have rather limited range of validity ($0.023 \leq \rho \leq 0.72 \text{ g/cm}^3$ and $550 \leq T \leq 660 \text{ K}$). In addition, the Pitzer-Sterner EOS for the SPC/E water does not adequately describe the behaviour of the higher-order derivatives of the pressure. This is due, in part, to the limited number of simulated $p\rho T$ data points used in the optimization of the EOS, as well as quite complex (27 coefficients) non-linear functional form of the Pitzer-Sterner formulation. It is worth mentioning that the reference state-of-the-art equations of state for real substances, such as IAPWS-95²⁰ (56 coefficients), are parameterized by using so-called “multi-property fitting”, where, in addition to a substantial $p\rho T$ data set, values of heat capacities, speed of sound, second virial coefficient, etc. are also included to ensure proper behaviour of the derivatives. Unfortunately, even nowadays, simulation of assorted thermophysical properties for a large number of state points over a wide $p\rho T$ area is still a tedious and time consuming task. Hence, the choice of the functional form of the EOS for simulated fluids is extremely important.

Recently, a new class of advanced technical equations of state has been developed by Wagner and Span.²¹⁻²⁴ The functional forms of this new type of EOS were successfully optimized for non-polar, weakly polar and typical polar fluids²¹⁻²³, as well as for natural gases and mixtures²⁴. The latter EOS²⁴ was adopted by the GERG (Groupe Européen de Recherche

Gazières) as the international reference equation of state for natural gases (GERG-2004). This equation was also parameterized for the corresponding binary and multicomponent mixtures. Detailed description regarding the development and performance of this class of EOS can be found in Refs. [21,24]. Simplicity and excellent numerical stability, combined with the high achievable accuracy²⁴, (similar to the best state-of-the-art reference equations), makes them very attractive for use in computer based predictions of properties of fluids. Perhaps, their best advantage from a simulation point of view is that substance-specific coefficients can be easily fitted to restricted data sets.

In the general form these equations of state are written as:

$$\frac{a(\rho, T)}{RT} = \frac{a^\circ(\rho, T) + a^r(\rho, T)}{RT} = \alpha^\circ(\delta, \tau) + \alpha^r(\delta, \tau), \quad (5.1)$$

where a is the Helmholtz energy, R is the gas constant, T is the temperature, ρ is the density, $\delta = \rho/\rho_c$ is the reduced density and $\tau = T_c/T$ is the inversely reduced temperature ($R = 8.314472 \text{ J mol}^{-1} \text{ K}^{-1}$ and $MW(\text{H}_2\text{O}) = 18.015280 \text{ g mol}^{-1}$). All thermodynamic properties can be calculated from Eq. 5.1 by considering the ideal, α° , and residual, α^r , parts of the Helmholtz energy and their derivatives. For example, the expression for pressure is given by:

$$\frac{P}{\rho RT} = 1 + \delta \cdot \alpha'_\delta, \quad (5.2)$$

where $\alpha'_\delta = (\partial \alpha^r / \partial \delta)_\tau$. Other applicable relations can be found in Ref. [24].

The explicit functional form of the new GERG-2004 EOS for water reads²⁴:

$$\begin{aligned}
\frac{a(\rho, T)}{RT} &= \alpha(\delta, \tau) = \alpha^\circ(\delta, \tau) + \alpha^r(\delta, \tau) = \\
&= \alpha^\circ(\delta, \tau) + n_1 \delta \tau^{0.5} + n_2 \delta \tau^{1.25} + n_3 \delta \tau^{1.875} + n_4 \delta^2 \tau^{0.125} + n_5 \delta^2 \tau^{1.5} \\
&+ n_6 \delta^3 \tau + n_7 \delta^4 \tau^{0.75} + n_8 \delta \tau^{1.5} e^{-\delta} + n_9 \delta^5 \tau^{0.625} e^{-\delta} + n_{10} \delta^5 \tau^{2.625} e^{-\delta} \quad (5.3) \\
&+ n_{11} \delta \tau^5 e^{-\delta^2} + n_{12} \delta^2 \tau^4 e^{-\delta^2} + n_{13} \delta^4 \tau^{4.5} e^{-\delta^2} + n_{14} \delta^4 \tau^3 e^{-\delta^3} \\
&+ n_{15} \delta \tau^4 e^{-\delta^5} + n_{16} \delta \tau^6 e^{-\delta^5}
\end{aligned}$$

The GERG-2004 EOS for water is represented by 16 linear coefficients and two reduced parameters, δ and τ . It is noteworthy, that the accuracy of the $p\rho T$ fit for this new EOS is not affected by the choice of the reference (scaling) temperature (say, T_c) as the fit coefficients simply scale as:

$$n_i^* = n_i \left(\frac{T_c}{T_c^*} \right)^{t_i} \quad (5.4)$$

where T_c and T_c^* are “true” and “pseudo” critical temperatures respectively. The same does not apply to critical density; however, most of the influence of the inaccurate value of the ρ_c on the quality of the $p\rho T$ fit can be still compensated by the optimized coefficients.²¹

Considerable efforts have been also directed to the improvement of the dielectric EOS for water and steam. Recently, Fernandez *et al.*²⁵ have collected and analyzed a large data set of static dielectric constants values for water. They presented dielectric EOS for real water valid over the temperature range from 238 to 873 K and pressures up to 1200 MPa. The functional form of the analytical EOS is very similar to that proposed by Wagner and Span²⁴.

The purpose of this study is to parameterize the thermodynamic (GERG-2004) and dielectric equations of state for SPC/E water over a wide range of temperatures and densities and examine their performance. The remainder of this chapter is organized as follows. Simulation

methodology is described in Section 5.3. The fitting procedures are presented in Section 5.4. Analysis of the EOS is given in Section 5.5. Our conclusions are given in Section 5.6.

5.3 Simulation Details

Thermodynamic and dielectric properties of the SPC/E water model were obtained in the NVT ensemble (constant density) by using conventional molecular dynamics. We have simulated over 250 state points between temperatures of 460 to 880 K with densities ranging from 0.023 to 0.920 g/cm³. Simulations were performed by using 343 particles in cubic periodic boundary conditions (PBC). We have also performed several additional simulations using a smaller, 216 particle, and a bigger, 512 particle, system; the results obtained were the same within statistical uncertainty. The fourth-order Gear algorithm²⁶ was used to integrate the isokinetic equations of motion with a time-step of 1 fs. Rotational degrees of freedom were represented using quaternions²⁷. The Ewald summation technique was employed exclusively to handle the long-range Coulomb forces. It has been shown²⁸ that for the examination of the dielectric properties of a polar fluid in PBC, it is advantageous to use Ewald summation method with dielectric boundary ϵ_{RF} similar to that of bulk medium. The static dielectric constant was calculated from the equilibrium fluctuations of the total dipole moment of the simulation cell.^{29,30}

$$\frac{(\epsilon - 1)(2\epsilon_{RF} + 1)}{(2\epsilon_{RF} + \epsilon)} = \frac{4\pi \langle M^2 \rangle}{3 V k_B T}, \quad (5.5)$$

where ϵ is the static dielectric constant, ϵ_{RF} is the dielectric constant at the boundary, V is the volume of the simulation box, k_B is the Boltzmann constant and T is the temperature. Note, that in this study the ratio $\langle M \rangle^2 / \langle M^2 \rangle$ does not exceed 0.005 %, with typical values being around 0.001%. The value of ϵ_{RF} was taken to be that of real water at given density and temperature. The simulation runs were 250 ps long with an equilibration period of 20 ps. Average root-mean-

square fluctuations for the pressure and static dielectric constant were determined to be within 10%.

5.4 Data Sets and Fitting Procedure

5.4.1 Thermodynamic EOS

In order to properly describe the low density states of the SPC/E model we have added (to the simulation data) 70 data points at densities ranging from 0.1 to 9.1×10^{-7} g/cm³ every 50 K between 460 and 780 K. The pressure for these low density states was calculated using the second virial coefficient, $B(T)$, of the SPC/E water model.³¹ Overall, 399 $p\rho T$ points were generated, 148 of which are unstable states. Unstable states are located inside the liquid-vapour coexistence region, having a positive derivative of the pressure with respect to density. Although we did not observe any phase separation at these state points on the time-scale of our simulations, they were excluded from the EOS parameterization to mimic “real” fluid thermodynamics. We find however that our final analytical fits reproduce the simulated $p\rho T$ values for these unstable states remarkably well (within the statistical uncertainty of the simulated data).

In the GERG-2004 formulation the expression for the Helmholtz free energy is given in reduced parameters and, thus, requires the values of the T_c and ρ_c to be determined. In molecular simulation, the location of the critical point can be deduced by calculating the coexistence properties in the Gibbs ensemble Monte Carlo^{32,33} (GEMC) followed by application of the scaling law (order parameter) and the law of rectilinear diameters.^{8,11} Unfortunately, high uncertainty in density estimates and finite size effects in the vicinity of the critical point may not allow for an accurate determination of the critical parameters.³⁴ A higher accuracy in the determination of the

critical parameters has been claimed by using the mixed-field finite-size scaling^{35,36} (MF-FSS) combined with histogram-reweighting³⁷ MC simulations in the grand canonical ensemble^{12,38,39} (HRGC). A comprehensive review of MC techniques in the study of phase equilibria can be found in Ref. [34].

Alternatively, one can determine the location of the critical point by simulating a large number of state points over entire $p\rho T$ surface and parameterizing an analytical EOS.^{8,13} However, this method may not yield the correct result either due to analyticity of the EOS.

In this work we take advantage of the dimensionless functional form of the GERG-2004 EOS, which enables self-consistent optimization of the critical parameters. The evaluation of the critical parameters, adopted in this study, relies on the examination of the thermodynamic behaviour of the analytical EOS in the vicinity of the critical point. The critical temperature and density were obtained by comparing the variation of the order parameter and the diameter of the coexistence curve of the SPC/E model with those of real water. The parameterization of the EOS was performed as follows. First, the coefficients in Equation 5.3 were optimized with “estimate” values of ρ_c^* and T_c^* over the range of densities and temperatures from 0.25 to 0.32 g/cm³ and from 625 to 645 K, respectively, with $\Delta\rho = 0.005$ g/cm³ and $\Delta T = 1$ K. All data points were assigned equal weighting as the structure of the data set is fairly even. In order to ensure correct behaviour of the first and second derivatives of the pressure at the critical point, an additional constraint during optimization was imposed:

$$\left(\frac{\partial p}{\partial \rho}\right)_{T=T_c} = 0 \quad \text{and} \quad \left(\frac{\partial^2 p}{\partial \rho^2}\right)_{T=T_c} = 0. \quad (5.6)$$

Next, for each set of optimized coefficients and corresponding ρ_c^* and T_c^* values, the coexistence properties of the EOS were evaluated. The calculation of the liquid-vapour boundary was based on the phase-equilibrium condition, which represents the equality of temperature,

pressure and Gibbs free energy (Maxwell construction) in the coexisting vapour and liquid phases:

$$\frac{P_\sigma}{RT\rho'} = 1 + \delta' \cdot \alpha_\delta^r(\delta', \tau), \quad (5.7.1)$$

$$\frac{P_\sigma}{RT\rho''} = 1 + \delta'' \cdot \alpha_\delta^r(\delta'', \tau), \quad (5.7.2)$$

$$\frac{P_\sigma}{RT} \left(\frac{1}{\rho''} - \frac{1}{\rho'} \right) - \ln \left(\frac{\rho'}{\rho''} \right) = \alpha_\delta^r(\delta', \tau) - \alpha_\delta^r(\delta'', \tau), \quad (5.7.3)$$

where p_σ is saturated pressure, ρ' and ρ'' are saturated liquid and vapour densities, respectively.

After that, the order parameter, $\rho_{lv}^* = (\rho_l - \rho_v)/2\rho_c$, and diameter, $\rho_d^* = (\rho_l + \rho_v)/2\rho_c$, of the analytical EOS were compared to those of real water over the temperature range of $0.01 < \theta < 0.04$, where $\theta = 1 - T/T_c$. Note, that the lower limit of θ was set to 0.01 in order to ensure that the correlation length did not exceed the simulation box size. The sum of squares, χ^2 (X^2), for the order parameter and rectilinear diameter was plotted as a function of ρ_c^* and T_c^* (here, X^2 represents mean-square deviations of the fitted model properties from real water values). The values of the critical density and temperature for the SPC/E model were obtained by locating the minimum on the χ^2 - ρ_c^* - T_c^* surface.

5.4.2 Dielectric EOS

To the selected values of the static dielectric constant of SPC/E water obtained in this study (240 state points) we have added 87 literature values from studies by Guissani and Guillot⁸, Wasserman¹⁴, Svishchev³⁰, Neumann¹⁵ and Mountain and Wallqvist¹⁶. The resulting data set

covers the density and temperature range from 0.023 to 1.0 g/cm³ and from 298 to 2500 K, respectively, with the majority of the values (306 points) located above T = 500 K isotherm.

In this study the values of the dielectric constant of SPC/E water were fitted by an EOS of the form:

$$\varepsilon = 1 + v_1 \delta \tau^{1/4} + v_2 \delta \tau + v_3 \delta \tau^{10/4} + v_4 \delta^2 \tau^{6/4} + v_5 \delta^3 \tau^{6/4} + v_6 \delta^3 \tau^{10/4}, \quad (5.8)$$

where δ and τ are the same as in Eq. 5.1.

The functional form of this equation was adopted from the work of Fernandez *et al.*,²⁵ who used a similar expression to describe density and temperature variations of the Alder-Harris g-factor. All data points were assigned equal weighting.

5.5 Data Analysis

5.5.1 Thermodynamic EOS

The simulated state points and analytical isotherms for the SPC/E water are shown in Fig. 5.1. The critical parameters were determined to be $\rho_c = 0.276$ g/cm³ and $T_c = 640.25$ K with a corresponding critical pressure of $p_c = 164.37$ bar. The results agree well with some previous estimates for the SPC/E water, see Table 5.1. The order parameter and diameter of the coexistence curve are plotted in Fig. 5.2. The temperature behaviour of the effective Verschaaffelt exponent, $\beta_{eff} = \partial \ln(\rho_l - \rho_v) / \partial \ln|\theta|$, is plotted in Fig. 5.3. As can be seen from Fig. 5.3, the variation of β_{eff} with temperature is very similar to that of real water up to $\theta \approx 0.06$, followed by an increase to the classical limit of 0.5 at $T = T_c$. Similar observations for the SPC/E pair-potential were reported by Guissani and Guillot.⁸

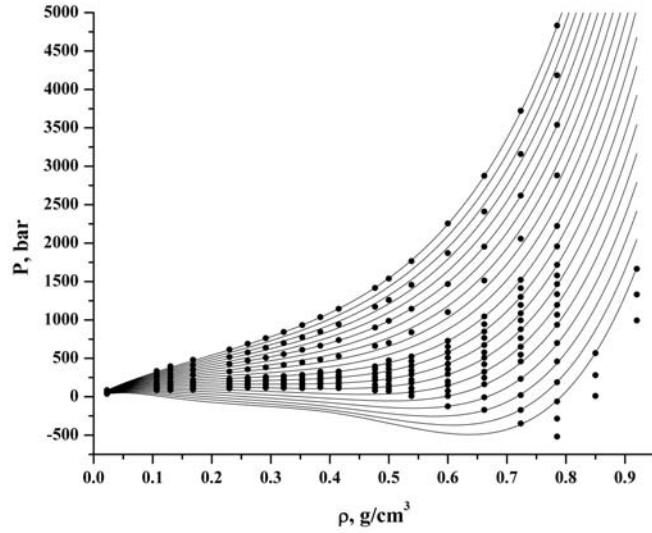


Figure 5.1 Representative isotherms for the SPC/E water. Continuous lines show isotherms from 500 (bottom curve) to 880 K (top curve) with $\Delta T = 20$ K. The points are the simulation results.

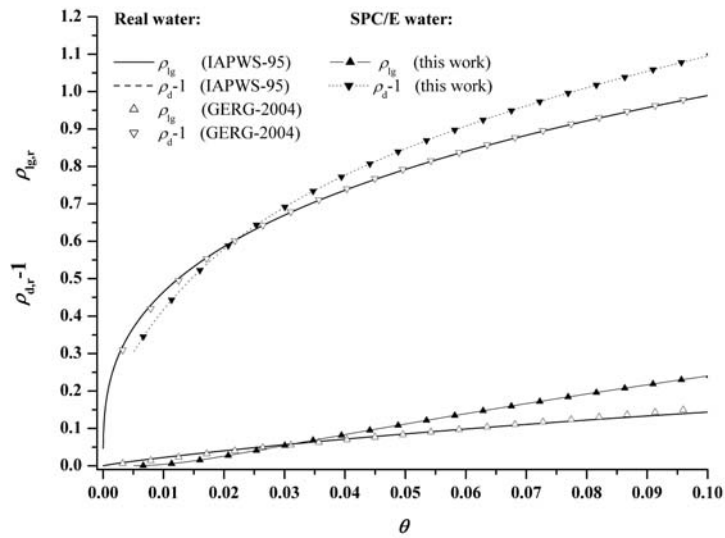


Figure 5.2 Order parameter and the diameter of the coexistence curve as a function of the reduced temperature $\theta = 1 - T/T_c$.

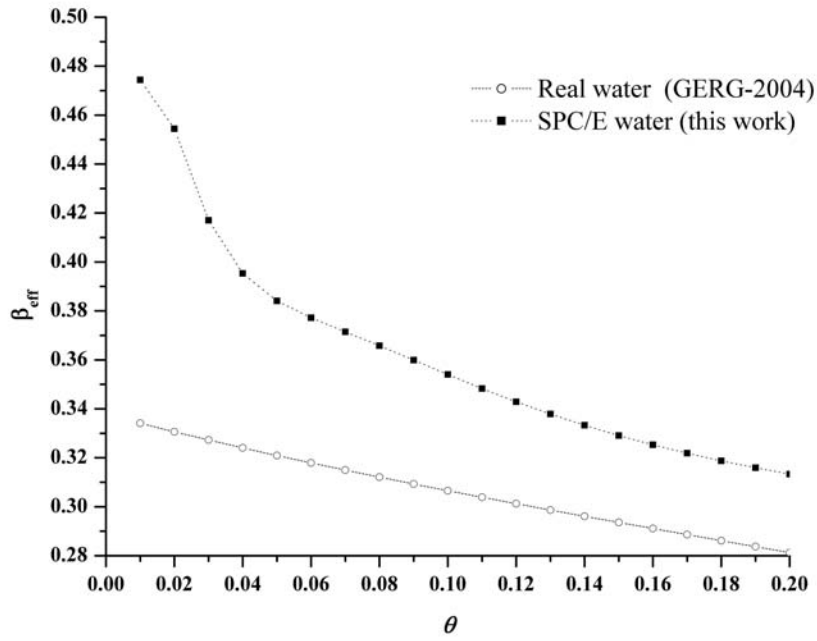


Figure 5.3 Temperature dependence of the Verschaffelt exponent, β_{eff} .

Table 5.1 Critical point parameters of the SPC/E water

	<i>Method</i>	T_c (K)	ρ_c (g/cm ³)	p_c (bar)	Z_c	Ref.
<i>Guissani and Guillot</i>	<i>MD, scaling laws</i>	640	0.29	160	0.187	8
<i>Errington et al.</i>	<i>THSG</i>	639.0 ± 1.1	0.2622 ± 0.0084			9
<i>Alejandre et al.</i>	<i>MD, scaling laws</i>	630.4	0.308			10
<i>Boulougouris et al.</i>	<i>GEMC</i>	630	0.295	148	0.172	11
<i>Errington et al.</i>	<i>HRGC, MF-FSS</i>	638.6 ± 1.5	0.273 ± 0.009	139 ± 4		12
<i>Hayward and Svishchev</i>	<i>MD, EOS</i>	641	0.28	163	0.197	13
<i>This work</i>	<i>MD, EOS</i>	640.25	0.276	164.37	0.201	
<i>Exptl.</i>		647.096	0.322	220.64	0.229	20

The mean relative error of the fit was determined to be on the order of 2% for pressure, which is significantly less than the calculated statistical uncertainty of the simulation (approximately 10%). The resulting liquid-vapour coexistence curve of the SPC/E water is compared with previous simulations and experimental data in Fig. 5.4. As can be seen from this figure, our results agree reasonably well with previous simulations by Alejandre *et al.*¹⁰ and Boulougouris *et al.*¹¹ Note, that the current EOS shows good extrapolation behaviour for the coexistence curve down to temperatures of about 400 K, which is significantly below the temperature range of simulated data. Nevertheless, we recommend the range of validity for this EOS to be from 460 to 880 K, in temperature, and from 0 to 0.92 g/cm³, in density (the range of simulated state points), as the relative error of the analytical fit becomes too high below 460 K.

In general, it is worth noting that based on our experience with classical water models and various equations of state, an accurate analytical parameterization of the low temperature states of computer simulated water should be left to a separate study, if one seeks to cover the region around the density maximum and supercooled states. The quality of a global analytical fit of the $p\rho T$ data worsens dramatically with the inclusion of low temperature state points, and for the SPC/E pair-potential their accurate analytical description could be even futile. The SPC/E model exhibits the density maximum and equilibrium melting point at a very low temperature (T_m of around 215 K according to Abascal *et al.*⁴⁰), with slow kinetics and large equilibration times (hence, modest practical utility).

In addition to the fit parameters for the GERG-2004 EOS for the SPC/E water, which are given in Appendix A.1, we also provide corresponding auxiliary equations for the saturated liquid and vapour densities, by using the same functional forms as in the reference IAPWS-95 formulation for real water substance²⁰:

Saturated liquid density equation:

$$\frac{\rho'}{\rho_c} = 1 + b_1\theta^{1/3} + b_2\theta^{2/3} + b_3\theta^{5/3} + b_4\theta^{16/3} + b_5\theta^{43/3} + b_6\theta^{110/3}, \quad (5.9)$$

with $\theta = 1 - T/T_c$.

Saturated vapour density equation:

$$\ln\left(\frac{\rho''}{\rho_c}\right) = c_1\theta^{2/6} + c_2\theta^{4/6} + c_3\theta^{8/6} + c_4\theta^{18/6} + c_5\theta^{37/6} + c_6\theta^{71/6}. \quad (5.10)$$

The coefficients for the Equations 5.9 and 5.10 for the SPC/E water are given in Appendix A.2.

In Fig. 5.5 we have compared the coexistence curve, thermodynamic spinodals and line of maximum isothermal compressibility [$\kappa_T = \rho^{-1}(\partial\rho/\partial p)_T$] of simulated EOS with those of real water in reduced units. This figure illustrates that the SPC/E potential nicely captures the thermodynamics of a real fluid at high temperatures; for instance, it provides a good description of the derivative properties, such as the compressibility. The density and temperature behaviour of the isothermal compressibility is shown separately in Fig. 5.6 to illustrate quality of the SPC/E model in the vicinity of the critical point.

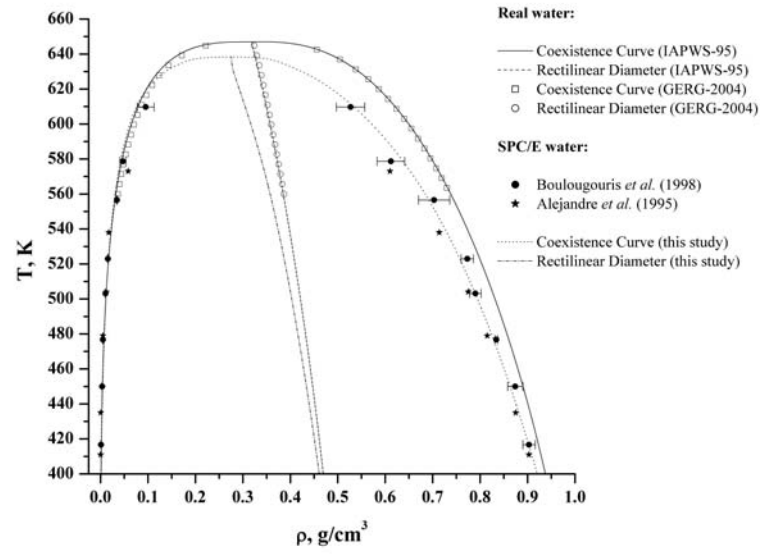


Figure 5.4 Liquid-vapour coexistence curve for water.

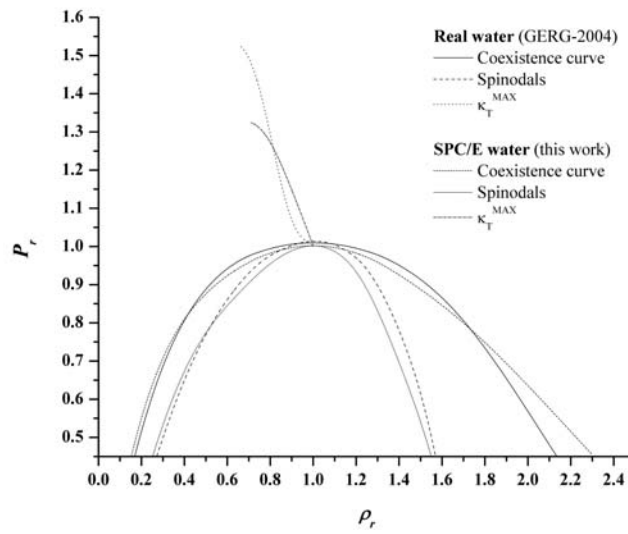


Figure 5.5 Liquid-vapour coexistence curve, thermodynamic spinodals and line of compressibility maximum of water, κ_T^{MAX} .

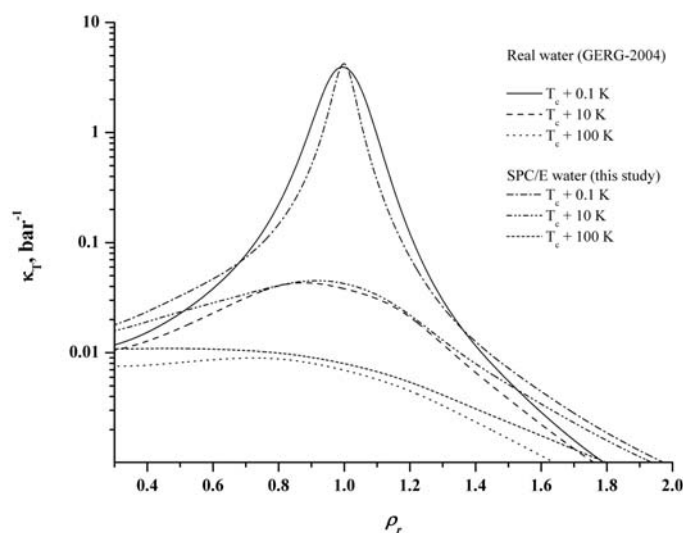


Figure 5.6 Isothermal compressibility of water as a function of reduced density at three selected temperatures above T_c .

5.5.2 Dielectric EOS

The temperature dependence of the static dielectric constant of SPC/E water along selected isochors together with data set values are shown in Fig. 5.7. The mean relative error of the fit was calculated to be less than 4%. The fitting parameters for the dielectric EOS (Equation 5.8) are given in Appendix B.1. The variation of the dielectric constant of the SPC/E water along the liquid-vapour coexistence curve (Equations 5.11 and 5.12), is compared to that of real water in Fig. 5.8. As expected (from a non-polarizable model), above its critical density the SPC/E water model slightly underestimates the value of the dielectric constant, whereas below ρ_c the prediction of the model is consistently higher than that in experiment. A similar conclusion has

been reached by Skaf and Laria¹⁷; with simulations done by Guàrdia and Martí¹⁸ also support this claim. We may note that some of the calculated values for the dielectric constant of the SPC/E water provided by Skaf and Laria fall into a parameterization range of our EOS. We have confirmed that these values are within the statistical uncertainty of our fit. The value of the static dielectric constant at the critical point of the SPC/E water was calculated to be 5.346, which is very close to the accepted experimental value of 5.361. We also provide auxiliary equations for the behaviour of the static dielectric constant along the coexistence line. The fitting parameters are given in Appendix B.2.

Static dielectric constant at saturated liquid density:

$$\frac{\varepsilon'}{\varepsilon_c} = 1 + k_1\theta^{1/3} + k_2\theta^{2/3} + k_3\theta^{5/3} + k_4\theta^{16/3} + k_5\theta^{43/3} + k_6\theta^{110/3}. \quad (5.11)$$

Static dielectric constant at saturated vapour density:

$$\ln\left(\frac{\varepsilon'' - 1}{\varepsilon_c - 1}\right) = l_1\theta^{2/6} + l_2\theta^{4/6} + l_3\theta^{8/6} + l_4\theta^{18/6} + l_5\theta^{37/6} + l_6\theta^{71/6}. \quad (5.12)$$

Note also that, although our dielectric EOS (Eq. 5.8) for SPC/E water is capable of fitting all available simulation data from 298 to 2500 K within total error of 4 %, we recommend its technical use be restricted to temperatures ranging from 400 to 880 K only, where the thermodynamic EOS accurately predicts the coexistence properties and derivatives of the pressure. In this case, any ambiguities regarding the definition of the coexistence curve, reduced parameters and corresponding states of the model and real fluid will be avoided.

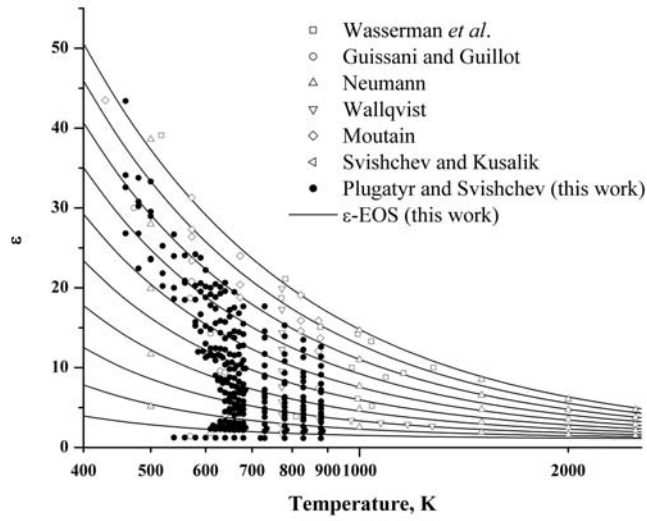


Figure 5.7 Temperature dependence of the static dielectric constant of the SPC/E water. Continuous lines represent isochors from 0.1 (bottom) to 1.0 g/cm³ (top).

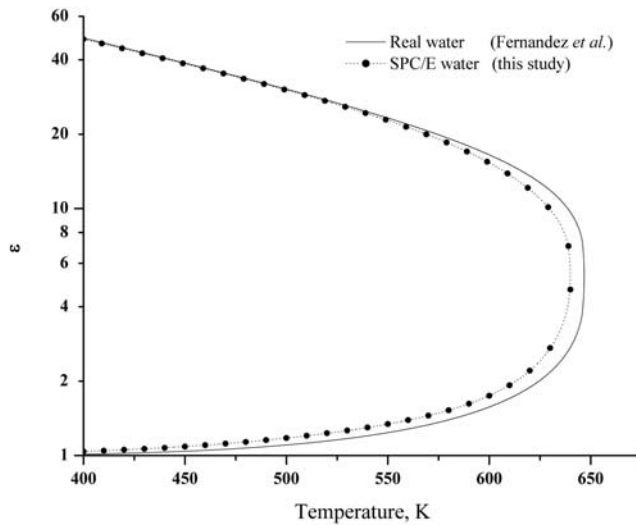


Figure 5.8 Static dielectric constant along the coexistence curve of water.

5.6 Conclusion

We have examined over 320 thermodynamic state points of the SPC/E water model in the NVT ensemble by means of MD simulation. Accurate thermodynamic and dielectric equations of state for SPC/E water are presented. The thermodynamic EOS is valid over the temperature and density ranges, of 460 to 880 K and 0.0 to 0.92 g/cm³, respectively. It is shown that the proposed EOS describes well the liquid-vapour coexistence properties of SPC/E water and exhibits good extrapolation behaviour to temperatures and pressures beyond its parameterization range. The critical parameters of SPC/E water were determined to be $\rho_c = 0.276$ g/cm³, $T_c = 640.25$ K and $p_c = 164.37$ bar. The dielectric EOS, fitted over a wider density and temperature range from 0.0 g/cm³ to 1.0 g/cm³ and from 298 to 2500 K, respectively, provides the most accurate, up-to-date, representation of the dielectric properties of SPC/E water. The value of the dielectric constant at the critical point of SPC/E water was determined to be 5.35, which compares very well with the corresponding experimental value of 5.36. Analytical thermodynamic and dielectric equations for saturated liquid and vapour densities are also given.

5.7 References for Chapter 5

1. M. D. Bermejo, M. J. Cocero, *AIChE J.* **52**, 3933 (2006).
2. A. Kruse, E. Dinjus, *J. Supercrit. Fluids* **39**, 362 (2007).
3. A. Kruse, E. Dinjus, *J. Supercrit. Fluids* **41**, 361 (2007).
4. J. Kronholm, K. Hartonen, M. Riekkola, *Trac-Trends Anal.Chem.* **26**, 396 (2007).
5. A. Kruse, H. Vogel, *Chem. Eng. Technol.* **31**, 1241 (2008).
6. P. MacDonald, J. Buongiorno, J.W. Sterbentz, C. Davis, R. Witt, Technical Report, Nuclear Energy Research Initiative Project 2001-001, "Feasibility Study of Supercritical Light Water Cooled Reactors for Electric Power Production" INEEL/EXT-04-02530.
7. H. J. C. Berendsen, J. R. Grigera, T. P. Straatsma, *J. Phys. Chem.* **91**, 6269 (1987).
8. Y. Guissani, B. Guillot, *J. Chem. Phys.* **98**, 8221 (1993).
9. J. R. Errington, K. Kiyohara, K. E. Gubbins, A.Z. Panagiotopoulos, *Fluid Phase Equilibr.* **150-151**, 33 (1998).
10. J. Alejandre, D. J. Tildesley, G. A. Chapela, *J. Chem. Phys.* **102**, 4574 (1995).
11. G. C. Boulougouris, I. G. Economou, D. N. Theodorou, *J. Phys. Chem. B* **102**, 1029 (1998).
12. J. R. Errington, A. Z. Panagiotopoulos, *J. Phys. Chem. B* **102**, 7470 (1998).
13. T. M. Hayward, I. M. Svishchev, *Fluid Phase Equilibr.* **182**, 65 (2001).
14. E. Wasserman, B. Wood, J. Brodholt, *Ber. Bunsen Phys. Chem.* **98** (1994) 906-911.
15. M. Neumann, *Computer simulation of water and the dielectric equation of state*, in Physical Chemistry of Aqueous Systems: Meeting the Needs of Industry, Proceedings of the 12th International Conference on the Properties of Water and Steam, edited by H. J. White Jr., J. V. Sengers, D. B. Neumann and J. C. Bellows, pp. 261-268 (1995).

16. R. Mountain, A. Wallquist, **NISTIR** 5778 (1996).
17. M. S. Skaf, D. Laria, *J. Chem. Phys.* **113**, 3499 (2000).
18. E. Guàrdia, J. Martí, *Phys. Rev. E.* **69**, 011502 (2004).
19. K. S. Pitzer, S. M. Sterner, *J. Chem. Phys.* **101**, 3111 (1994).
20. W. Wagner, A. Pruss, *J. Phys. Chem. Ref. Data* **31**, 387 (2002).
21. R. Span, W. Wagner, *Int. J. Thermophys.* **24**, 1 (2003).
22. R. Span, W. Wagner, *Int. J. Thermophys.* **24**, 41 (2003).
23. R. Span, W. Wagner, *Int. J. Thermophys.* **24**, 111 (2003)
24. O. Kunz, R. Klimeck, W. Wagner, M. Jaeschke, *The GERG-2004 wide-range equation of state for natural gases and other mixtures*, Fortschr.-Ber. VDI, Düsseldorf, 2007.
25. D.P. Fernandez, A. R. H. Goodwin, E. W. Lemmon, J. M. H. L. Sengers, R. C. Williams, *J. Phys. Chem. Ref. Data* **26**, 1125 (1997).
26. D.J. Evans, O. P. Morriss, *Comput. Phys. Rep.* **1**, 297 (1984).
27. D.J. Evans, *Mol. Phys.* **34**, 31 (1977).
28. P. G. Kusalik, *J. Chem. Phys.* **93**, 3520 (1990).
29. M. Neumann, O. Steinhauser, G. S. Pawley, *Mol. Phys.* **52**, 97 (1984).
30. I. M. Svishchev, P. G. Kusalik, *J. Phys. Chem.* **98**, 728 (1994).
31. P. G. Kusalik, F. Liden, I. M. Svishchev, *J. Chem. Phys.* **103**, 10169 (1995).
32. A. Z. Panagiotopoulos, *Mol. Phys.* **61**, 813 (1987).
33. A. Z. Panagiotopoulos, N. Quirke, M. Stapleton, D. J. Tildesley, *Mol. Phys.* **63**, 527 (1988).
34. A. Z. Panagiotopoulos, *J. Phys.-Condes. Mat.* **12**, 25 (2000).

35. N. B. Wilding, A. D. Bruce, *J. Phys.-Condes. Mat.* **4**, 3087 (1992).
36. N. B. Wilding, *Phys. Rev. E* **52**, 602 (1995).
37. A. M. Ferrenberg, R. H. Swendsen, *Phys. Rev. Lett.* **61**, 2635 (1988).
38. N. B. Wilding, M. Muller, K. Binder, *J. Chem. Phys.* **105**, 802 (1996)
39. A. Z. Panagiotopoulos, V. Wong, M. A. Floriano, *Macromolecules* **31**, 912 (1998).
40. J.L.F. Abascal, E. Sanz, R. G. Fernandez, C. Vega, *J. Chem. Phys.* **122**, 234511 (2005).

Chapter 6

Residence Time Distribution Measurements and Flow Modeling in a Supercritical Water Oxidation Reactor: Application of Transfer Function Concept

6.1 Abstract

Residence time distribution (RTD) measurements are carried out in a flow-through tubular supercritical water oxidation (SCWO) reactor using *ex situ* pulse response experiments. The experiments are performed from ambient to supercritical water conditions with a volumetric flow rate fixed at 1 ml/min. The transfer function concept is used to interpret tracer information and to elucidate hydrodynamic flow patterns inside the “hot zone” of the reactor vessel. The experimental RTD curves are modeled by an axially dispersed plug flow. At supercritical conditions the studied tubular SCWO reactor can be characterized as a mixed flow system (with Péclet numbers of 1.4 – 2). The results also indicate the presence of fast preferential fluid flow in the reactor below 573 K and 10 MPa.

6.2 Introduction

Supercritical water oxidation is now recognized as one of the most promising “green” technologies for the destruction of hazardous organic waste. The development and process optimization of this advanced technology requires thorough understanding of both the chemical reaction kinetics and physical effects (hydrodynamic flow patterns) at supercritical water conditions. In recent years, a double-wall reactor concept (transpiring wall reactor)¹⁻⁷ has been implemented in order to overcome the main technological problems of the SCWO process, namely corrosion of reactor materials and precipitation of salts. In a transpiring wall reactor oxidation takes place in the upper zone of the tubular space under supercritical water conditions, whereas the lower zone of the reactor is kept below the critical temperature to minimize salt precipitation.

From a physical standpoint, the flow pattern in a SCWO reactor (especially in a transpiring wall reactor) is arguably quite complex to be described by ideal flow models. These models are often used for the estimation of mean residence times in experimental laboratory SCWO studies, Ref. [8-10] and therein. It is important to emphasize that the kinetics data obtained without proper account of the hydrodynamic regime of a SCWO reactor may be inconsistent or even misleading, which makes any comparison of the prospective reactor configurations ambiguous and may cause problems if used in scale-up.^{11,12} Generally, deviations from ideal reactor behaviour may arise from non-uniform fluid velocity profile distribution, back-mixing (axial dispersion), imperfect mixing (continuously stirred reactors), by-passing, the existence of dead space, etc. Rigorous testing of the hydrodynamic performance of the SCWO reactor and accurate determination of the residence times of the reacting mixture inside the “hot reaction zone” is therefore crucial for obtaining reliable and reproducible kinetics data.

One of the approaches to modeling flow patterns in chemical reactors employs computational fluid dynamics (CFD) methods. The application of CFD requires accurate values of the transport properties of the fluid under supercritical conditions in order to solve momentum balance (Navier-Stokes) equations. The fluid flow in SCWO reactors has been examined by means of CFD tools by several research groups.^{3,13,14}

An alternative and perhaps easier method for evaluating the hydrodynamic performance of chemical reactors uses the residence time distribution (RTD) measurements. This method does not require *a priori* knowledge of fluid properties. The RTD curves are obtained by introducing an inert tracer compound at the reactor inlet and monitoring its concentration at the outlet[†].

Unfortunately, due to extreme supercritical water conditions a direct *in situ* approach of obtaining the RTD curves is quite difficult and requires sophisticated analytical equipment capable of withstanding high temperatures, pressures and a corrosive environment. In addition, in cases where the time-concentration profile of a tracer is monitored only at the reactor outlet, the RTD measurements under supercritical water conditions also necessitate extensive calibration procedures in order to account for changes in water density, attenuation of the spectroscopic coefficients or, in the case of electrochemical detection, changes to the dielectric constant of water.

Current literature contains only a handful of RTD studies for SCWO reactors, which are summarized in Table 6.1. As can be seen from Table 6.1, previous RTD studies were conducted either under subcritical water conditions or using scCO₂ as a carrier. With the exception of a study by Lieball,³ the RTD experiments were performed using a one-point measuring technique (i.e. tracer concentration was monitored at the reactor outlet only). In the case of indirect RTD

[†] Detailed description of the RTD measurements can be found in classical chemical engineering texts such as Levenspiel [15].

measurements, where concentration of a tracer is monitored after temperature and pressure let down,¹⁶ caution should be taken in interpreting the tracer information, as the RTD curves obtained in this fashion do not describe the behaviour of the reactor alone, but also reflect alterations to the flow in other system components, such as heat exchangers, various fittings, the back-pressure regulator, etc.

In this work, we examine the hydrodynamic performance of a flow-through SCWO reactor using *ex situ* RTD measurements. The response curves of the SCWO reactor system are obtained with and without the reactor section in separate pulse injection experiments. The transfer function concept is then used to interpret tracer information and gain insights into flow patterns inside the reactor's "hot zone". This approach significantly simplifies the technical aspects of RTD experiments under supercritical water conditions, as tracer injection and detection are performed outside the "hot zone" of the SCWO reactor system. We characterize the hydrodynamic behaviour of a tubular flow-through reactor equipped with narrow inlet and outlet lines, from ambient to supercritical conditions.

The remainder of this chapter is organized as follows. The experimental apparatus and procedures are given in Section 6.2. The modeling procedure and employed flow models are described in Section 6.3. The results are discussed in Section 6.4. Our conclusions are given in Section 6.5.

Table 6.1 Summary of the RTD studies in SCWO reactors.

<i>Reactor Type</i>	<i>Carrier</i>	<i>Conditions</i>	<i>Tracer</i>	<i>Measuring Technique</i>	<i>Detection</i>	<i>Ref.</i>
Transpiring wall (2-zone)	CO ₂	T = 323 K P = 5 MPa	Toluene	1 point, direct	UV	1
Transpiring wall	water	T = 573 K P = 25 MPa	Salt solution	2 point, direct	Electric Conductivity	3
Tubular	CO ₂	T = 373 - 473 K P = 10 - 30 MPa	Isophorone in MeOH	1 point, direct	UV	16
	water	T = 473 - 523 K P = 20 - 25 MPa	Benzoic acid	1 point, indirect		
Helical tubular	water	T = 573 K P = 24 MPa	Rodamine B	1 point, direct	UV - Vis	17

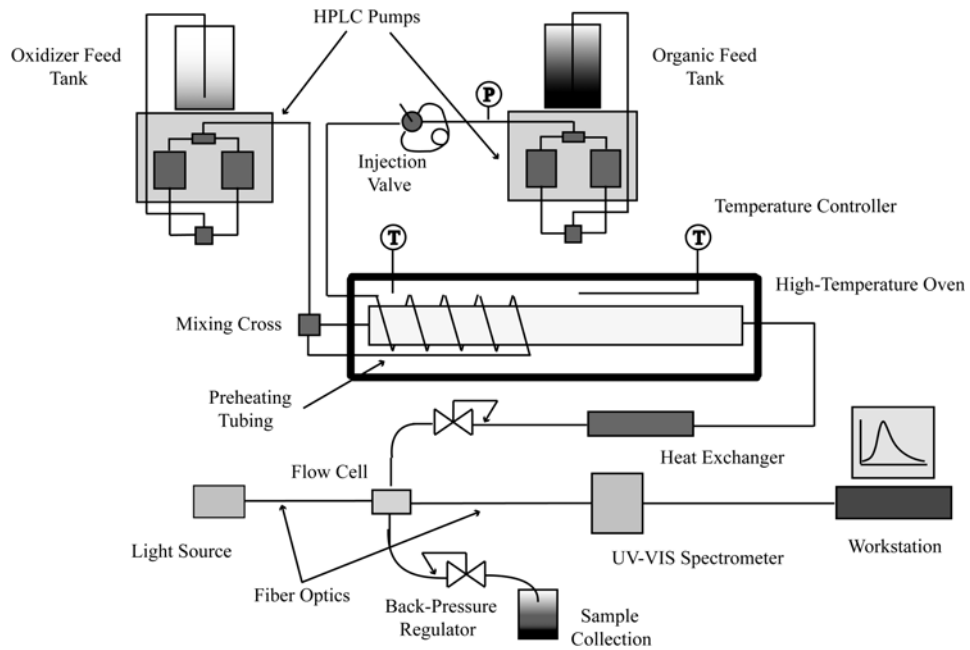


Figure 6.1 Schematics of the flow-through SCWO reactor system

6.3 Experimental Apparatus and Procedure

6.3.1 Experimental apparatus

The schematics of the employed bench-top flow-through tubular SCWO reactor system is shown in Fig. 6.1. The apparatus consists of two HPLC pumps (Bio-Rad® 1330 and Waters® M6000 A). In this study, only one pump was used to deliver pure degassed deionized water, which serves as a carrier fluid. A six-port two position manual sample injection valve, equipped with a 500 μ L sample loop, was installed to carry out flow injections of a tracer solution into the SCWO system. The reactor was constructed of a stainless steel SS316 tube (4.6 mm i.d., $L = 250$ mm). Carrier water was preheated to the operating temperature by passing through a coiled capillary tube (0.25 mm i.d., $L = 1$ m) before entering the reactor. The preheater and the reactor fit inside a high temperature oven. The temperature of the oven was maintained and controlled by a thermostat (Omron® E5SC) equipped with a K-thermocouple. A heat exchanger was used to cool down the effluent to ambient temperature. Cooled and partially depressurized effluent was passed through a 10 mm optical path stainless steel flow cell FIA-Z-SMA (FIA Inc.). On-line spectroscopic measurements were performed using Ocean Optics® USB-2000 UV-Vis spectrometer equipped with a CCD camera. The effluent was fully depressurized after passing the second back pressure regulator. The pressure in the system was controlled by an adjustable back pressure regulator (Upchurch® P-880) and monitored using a Nupro® pressure gauge. All high-pressure parts of the employed SCWO reactor system, from the pumps to the back pressure regulator, are connected using stainless steel SS316 tubing (0.5 mm i.d.).

6.3.2 Experimental procedure

Two sets of flow injection experiments were performed. The first series of experiments was conducted without the tubular SCWO reactor in order to obtain the response curves of the injection section (fore- and after- sections) of the experimental apparatus. The preheater was connected directly to the heat exchanger using a low dead-volume union. The second series of experiments was performed at identical operating conditions as the first one, but with the SCWO reactor installed. In both sets of experiments at least three individual RTD measurements were performed at each state point. The volumetric flow rate in all experiments was fixed at 1 ml/min. Summary of experimental conditions as well as calculated fluid velocities and Reynolds numbers are given in Table 6.2. The fluid velocity was estimated based on the assumption of an ideal plug flow behaviour in the tubular reactor. The Reynolds number was obtained according to the following expression:

$$Re = \frac{\rho \cdot u \cdot d}{\mu}, \quad (6.1)$$

where ρ , u , and μ are density, velocity and dynamic viscosity of the fluid, respectively, and d is the diameter of the tube. The reactor was assumed to operate isothermally.

In this study, phenol was used as a tracer compound. High thermal stability of phenol in the absence of oxygenated media has been reported in a number of studies.^{19,20} Phenol (Sigma-Aldrich, 99% pure) was used to prepare 1000 ppm stock solution. Fresh tracer solutions were made by diluting stock phenol solution with deionized water. Prior to each injection, the system was allowed to stabilize at a set operating temperature and pressure for about 20 min. After that, an injection valve, preloaded with tracer solution, was switched on, and a pulse of aqueous phenol solution was introduced into the system. The duration of the square pulse in this study was 30 s. The beginning of spectra acquisition was synchronized with the injection event. The primary

channel of the spectrometer was used to monitor phenol absorbance at a wavelength of 270 nm. The baseline spectrum was collected at 500 nm. The spectrometer acquisition time was set at 1 sec. The spectrometer was calibrated using five external standard injections.

In order to ensure correct mass balance during RTD measurements, the total concentration of phenol was calculated from the obtained RTD curves and compared with the total concentration of injected tracer. In this study, more than 95% of the injected phenol was detected in each individual experiment.

Table 6.2 Summary of the experimental conditions*

T, K	p, MPa	$\rho, kg \cdot m^{-3}$	$\mu, \mu Pa \cdot s$	$u, 10^{-3} m \cdot s^{-1}$	Re
298	2	998	890	1.0	5
473	5	867	135	1.2	34
573	10	715	87.1	1.4	53
648	22.5	408	48.2	2.5	96
698	22.5	105	27.5	9.6	168
748	22.5	85	29.2	11.8	158
798	22.5	77	31.6	13.0	146

*The values of density and dynamic viscosity of water were taken from Ref. [18]

6.4 Modeling procedure and flow models

6.4.1 Flow parameter estimation from *ex situ* RTD measurements

In this study, we combine the experimental approach of van Nugteren-Osinga *et al.*²¹ with the transfer function concept in order to examine hydrodynamic behaviour of the tubular flow-through reactor under sub- and supercritical water conditions. Van Nugteren-Osinga *et al.* have shown that under suitable experimental conditions it is possible to obtain an impulse/response function of a particular section of the flow system by means of a deconvolution procedure of the response curves obtained with and without the section concerned (This section can be a reactor itself, back-pressure regulator, mixing tee, or any other component of the flow system.). In their study the fast Fourier transform algorithm was used to calculate the time domain impulse/response functions of the flow-injection system components.

The application of transfer functions in RTD modeling studies has been described in a number of studies, Ref. [11, 22-25] and therein. The transfer function is defined as the ratio of the transformed time domain response and input functions. The transfer function of the residence time distribution can be written as²⁵:

$$h(s) = \frac{\mathcal{L}\{R'(t)\}}{\mathcal{L}\{I'(t)\}} = \frac{\int_0^{\infty} R'(t)e^{-st} dt}{\int_0^{\infty} I'(t)e^{-st} dt} = \frac{r(s)}{i(s)}, \quad (6.2)$$

where s is the Laplace space variable, $r(s)$ and $i(s)$ are the Laplace transforms of the normalized time domain input, $I'(t)$, and output, $R'(t)$, concentration curves.

The schematic diagrams of the *in situ* RTD measurements and the *ex situ* approach employed in this study are shown in Fig. 6.2. In a typical *in situ* RTD experiment (see Fig.6.2(a)),

the input and output concentration curves are measured directly at the reactor's inlet and outlet, which is often referred to as the two point measuring technique. In the *ex situ* RTD measurements (see Fig.6.2(b)), the concentration response curves are obtained in a series of pulse injection experiments conducted without and with the section of the flow system concerned.

A typical SCWO apparatus consists of a feed line, preheater, reactor, heat exchanger, back-pressure regulator, various fittings, etc. The RTD curve for the SCWO reactor system can be viewed as a convolution of several functions that characterize the flow in each individual section of the experimental apparatus. The response of a system without the section of interest can be written in Laplace space as:

$$r_1(s) = p(s) \cdot h_A(s) \cdot h_B(s), \quad (6.3)$$

where $p(s)$ is the Laplace transform of the normalized tracer pulse function, $P'(t)$, and transfer functions $h_A(s)$ and $h_B(s)$ characterize the flow in the fore- and after- sections of the experimental apparatus, respectively.

The Laplace domain response of the system with the section of interest installed (e.g. reactor) is given by:

$$r_2(s) = p(s) \cdot h_A(s) \cdot h_R(s) \cdot h_B(s), \quad (6.4)$$

where $h_R(s)$ is the transfer function of the new section of the flow system.

Thus, under the assumption that the tracer solutions entering consecutive flow system components are homogeneously mixed over the cross-section, the transfer function of the section under investigation, $h_R(s)$, can be found from the deconvolution of the two normalized experimental response curves obtained with, $R'_2(t)$, and without, $R'_1(t)$, the section of interest:

$$h_R(s) = \frac{r_2(s)}{r_1(s)} = \frac{\mathbb{L}\{R'_2(t)\}}{\mathbb{L}\{R'_1(t)\}}. \quad (6.5)$$

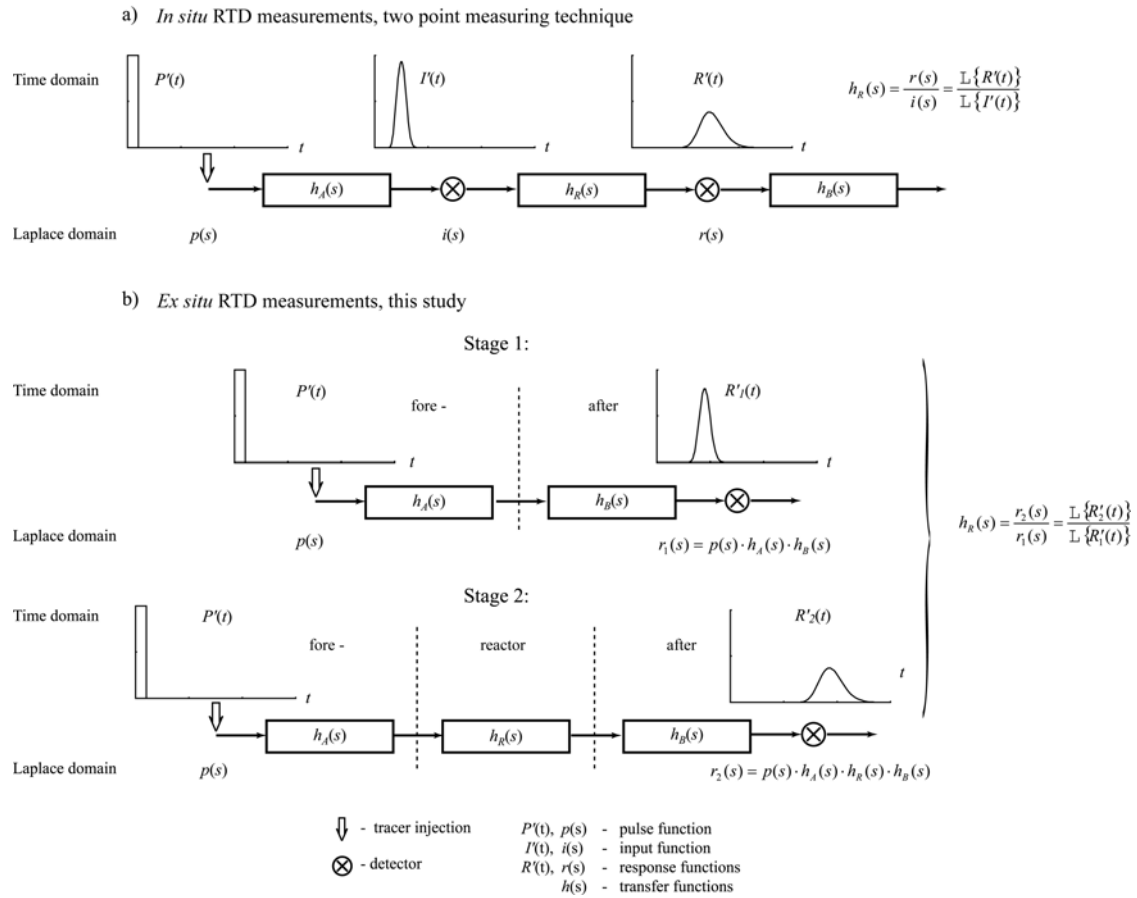


Figure 6.2 Schematic diagrams of the a) in situ and b) ex situ RTD measurements

An analytical expression for a transfer function can be derived from Eq. 6.2 using a particular flow model and appropriate boundary conditions.¹¹ Modeling of complex reactor behaviour may require a combination of several “basic” transfer functions in series or in parallel. The application of combined flow models has been described in detail by Wen and Fen.¹¹

Among the techniques used for flow parameter estimation from RTD data are moment analysis, weighted moment analysis, Fourier analysis, transfer function fitting in the Laplace domain and time domain curve-fitting.²⁴⁻²⁷ Detailed description of these methods can be found in Ref. [27]. Time domain curve-fitting is considered to be the most robust and reliable procedure.²⁷ The method is based on time-domain comparison of the experimental and predicted response curves. According to Eq. 6.5, the concentration response curve of the flow-through system obtained with the section of interest, $R'_2(t)$, can be predicted by using the experimental RTD curve of injection section of experimental apparatus, $R'_1(t)$, and the flow model transfer function for the section under investigation.

Briefly, both normalized response curves can be expressed in terms of Fourier series:

$$R'_{(k=1,2)}(t) = \frac{a_k^0}{2} + \sum_{n=1}^{\infty} \left[a_k^n \cos\left(\frac{n \cdot \pi \cdot t}{\tau}\right) + b_k^n \sin\left(\frac{n \cdot \pi \cdot t}{\tau}\right) \right] \quad (6.6)$$

with Fourier coefficients evaluated by

$$a_{(k=1,2)}^n = \frac{1}{\tau} \int_0^{2\tau} R'_k(t) \cos\left(\frac{n \cdot \pi \cdot t}{\tau}\right) dt \quad (6.6.1)$$

and

$$b_{(k=1,2)}^n = \frac{1}{\tau} \int_0^{2\tau} R'_k(t) \sin\left(\frac{n \cdot \pi \cdot t}{\tau}\right) dt, \quad (6.6.2)$$

where 2τ is the time at which the signal of the response function, $R'_2(t)$, vanishes. The Fourier coefficients of both response functions are related through the definition of the transfer function in the Fourier domain ($s = in\pi/\tau$):

$$h_R\left(\frac{i \cdot n \cdot \pi}{\tau}\right) = \frac{\int_0^{2\tau} R'_2(t) e^{-\left(\frac{i \cdot n \cdot \pi}{\tau}\right)t} dt}{\int_0^{2\tau} R'_1(t) e^{-\left(\frac{i \cdot n \cdot \pi}{\tau}\right)t} dt} = \frac{a_2^n - ib_2^n}{a_1^n - ib_1^n}. \quad (6.7)$$

Thus, the response of the system with the section installed, $R'_2(t)$, can be predicted by evaluating its Fourier coefficients using the experimental RTD curve, $R'_1(t)$, and the transfer function for the section under investigation. The experimental and predicted response curves are then compared in terms of the root mean square error (*RMS*)²⁷:

$$RMS = \sqrt{\frac{\int_{t_1}^{t_2} (R'_{2,exptl.}(t) - R'_{2,pred.}(t))^2 dt}{\int_{t_1}^{t_2} (R'_{2,exptl.}(t))^2 dt}}, \quad (6.8)$$

which is minimized with respect to transfer function parameters using an optimization algorithm.

6.4.2 Flow models

In this study, the flow pattern in a tubular SCWO reactor were characterized using the axially dispersed plug-flow (ADPF) model:

$$\frac{\partial C}{\partial t} = D_a \frac{\partial^2 C}{\partial x^2} - \bar{u}_0 \frac{\partial C}{\partial x} - k' C, \quad (6.9)$$

where C is the average cross-section tracer concentration, D_a is the axial dispersion coefficient, \bar{u}_0 is the averaged axial velocity of the fluid and k' is a pseudo-first order rate constant. The

ADPF model is perhaps the most widely used model for the description of flow in tubular chemical reactors.^{11,24,28} In this flow model, the axial dispersion coefficient accounts for the deviations of real systems from an ideal plug flow behaviour. One of the main advantages of this flow model is that it allows for the description of flow patterns ranging from plug ($D_a = 0$) to fully mixed ($D_a \rightarrow \infty$) flow and does not require any prior knowledge of the velocity distribution profile in the system²⁸. The axial dispersion coefficient, D_a , is commonly expressed as a characteristic dimensionless Péclet number, Pe :

$$Pe = \frac{uL}{D_a}, \quad (6.10)$$

where L is the characteristic length of the section of experimental apparatus.

The transfer function for the ADPF model (closed-closed boundary conditions) is given by¹¹:

$$h^{ADPF}(s) = \frac{4 \cdot \varphi \exp\left[\frac{Pe}{2}(1-\varphi)\right]}{(1+\varphi)^2 - (1-\varphi)^2 \exp[-Pe \cdot \varphi]}, \quad (6.11)$$

where $\varphi = \sqrt{1 + 4 \cdot (s+k') \cdot \bar{\tau}/Pe}$ and Pe is the Péclet number, $\bar{\tau}$ is the mean residence time of the fluid in the system and k' is the pseudo-first order rate constant for tracer disappearance (for a non-reacting system, $k' = 0$).

It is important to emphasize that the employed SCWO reactor features narrow inlet and outlet lines. It has been shown that such reactor configurations may exhibit marked variations in radial fluid velocity, where the fluid passing along the center of the tube has distinctly shorter residence time than that flowing closer to the periphery.²⁹ Hence, two flow models have been constructed. The block diagrams of the two flow models employed in this study are shown in Fig. 6.3. In Model 1, Fig. 6.3(a), the flow in the system is described using the ADPF model, for which

the flow is characterized by two parameters, the mean residence time, $\bar{\tau}$, and the Péclet number, Pe . In Model 2, Fig. 6.3(b), the flow pattern in the reactor vessel is viewed as a combination of two sub-flows in parallel, where each sub-flow is represented using the ADFP model. Here, the flow in the reactor is characterized by two sets of flow parameters; Pe_1 and $\bar{\tau}_1$ are, respectively, the dispersion coefficient and the mean residence time of the fast flowing fraction f , while Pe_2 and $\bar{\tau}_2$, are the corresponding flow parameters of the remaining fluid. It should be noted that Péclet numbers, obtained in this study, must be considered as mean values that characterize the overall dispersion in the SCWO reactor.

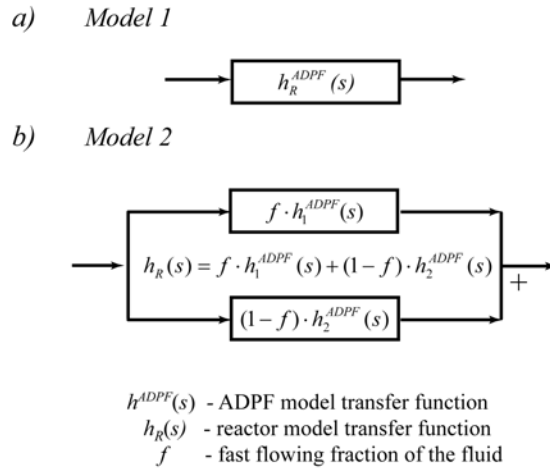


Figure 6.3 Block diagrams of the employed flow models

Due to the “two-stage” nature of the *ex situ* RTD experiments, the mean response of the system without the section of the experimental apparatus under investigation (reactor) was calculated by averaging several individual normalized RTD curves obtained at the same experimental conditions. It should be noted that all experimental RTD curves, acquired without the reactor section at identical experimental conditions, showed excellent reproducibility with the root mean square deviation being less than 3%.

In the optimization of Model 1, the mean residence time parameter was initialized using the value calculated from the difference in the first moments of the normalized experimental RTD curves obtained with , $R_2'(t)$, and without, $R_1'(t)$, the SCWO reactor:

$$\bar{\tau}_{mom.} = \int_0^{t_2} t \cdot R_2'(t) dt - \int_0^{t_1} t \cdot R_1'(t) dt . \quad (6.12)$$

The flow parameters obtained from Model 1 were used as starting parameters for the optimization of Model 2. Time domain curve-fitting procedure was carried out using Mathematica® 4.1 package. The non-linear fit was performed according to the Levenberg – Marquardt algorithm.

6.5 Results and Discussion

The inspection of experimental RTD curves, obtained without and with the SCWO reactor, suggests that the flow in the studied tubular reactor is subject to a substantial degree of mixing at all experimental conditions examined, see Fig. 6.4.

The results obtained using Model 1 (the ADPF model) as well as mean residence times calculated from moment analysis are given in Table 6.3. At ambient and moderate conditions ($Re \leq 34$) Model 1 does not capture the shape of the experimental RTD curves, as the *RMS* error of the fit exceeds 24%, see Table 6.3. However, at $Re \geq 53$, the ADPF model reproduces the experimental data quite well with the *RMS* error of less than 8.3%, Fig. 6.4(c-d). The Péclet number decreases from approximately 2.1 at 573 K and 10 MPa ($Re = 53$) to 1.4 at 798 K and 22.5 MPa ($Re = 146$). Relatively low Péclet numbers indicate a high rate of mixing of the fluid in the reactor at elevated temperatures and pressures. This hydrodynamic behaviour can be attributed to a turbulent flow with recirculation, the presence of which was observed by Batten for

similar reactor geometries at $Re > 130$.²⁹ The turbulence occurs due to a sudden increase in the diameter of the tube, where the fluid entering the vessel has a significantly higher velocity than that in the reactor. When the length of such a reactor is too short, the laminar flow, which is expected at low Reynolds numbers ($Re < 2000$), is not established. Furthermore, the presence of a narrow outlet line creates a recirculation zone.

Model 2, for which the flow in the reactor is described using two sub-flows in parallel, provides a much better fit for the experimental data at low temperatures, Fig. 6.4 (e and f). The *RMS* error of the fit was calculated to be less than 6 %, Table 6.4. The results obtained from Model 2 suggest that at low Reynolds numbers ($Re \leq 34$) about 37% of fluid maintains a rather high average axial velocity. At 298 K and 2 MPa ($Re = 5$), the Péclet number and the mean residence time of the fast flowing fraction were determined to be approximately 89 and 169 s, respectively. The remaining 63% of the fluid is characterized by a distinctly longer mean residence time of 319 s and a somewhat low Peclet number of approximately 9. At 473 K and 5 MPa ($Re = 34$), the Péclet number of the fast and slow fractions decreases to about 53 and 4, respectively, with corresponding mean residence times of approximately 112 and 311 s. These results suggest that the overall rate of mixing of the fluid in the reactor increases with Reynolds number. At higher temperatures and pressures ($Re > 53$) the flow is fairly well mixed and, as a result, can be described using the more simple Model 1.

It is worth pointing out that once the flow parameters in the reactor system have been determined, the transfer function approach can also be used for the direct evaluation of the rate constants for reactions occurring in the “hot zone” of flow-through SCWO reactors. No doubt, these investigations will provide more accurate information about oxidation reaction rates under supercritical water conditions.

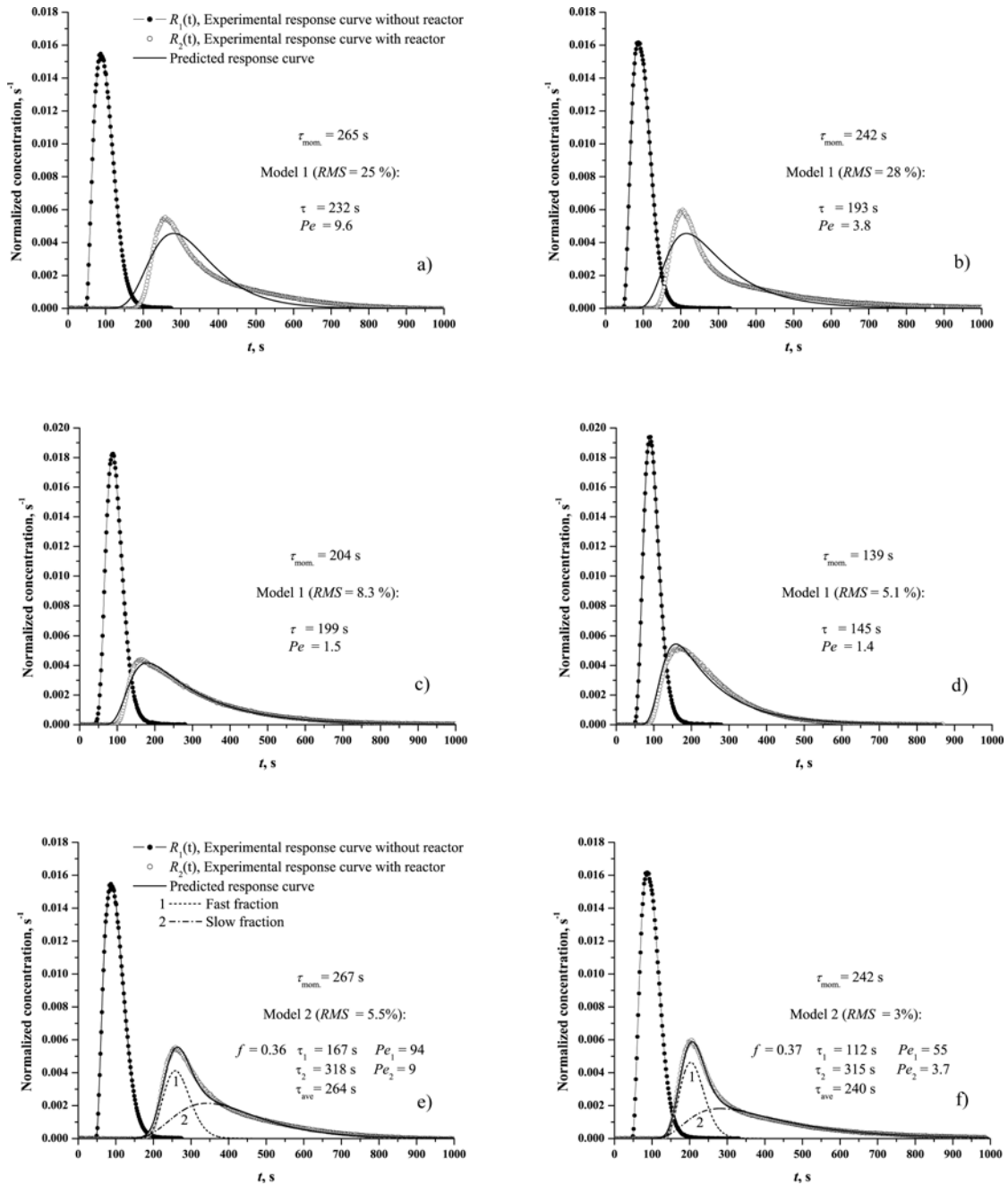


Figure 6.4 Examples of experimental and predicted RTD curves using Model 1 (a-d) and Model 2 (e-f) at a) 298 K b) 473 K, c) 648K, d) 748 K, e) 298K and f) 473 K.

Table 6.3 Mean residence times, Péclet numbers and the average *RMS* error obtained using Model 1.

T, K	P, MPa	Re	$\bar{\tau}_{mom}, s$	Pe	$\bar{\tau}, s$	$RMS, \%$
298	2	5	266.8 ± 5.1	10.0 ± 1.0	233.3 ± 5.9	24.5
473	5	34	239.0 ± 10	3.9 ± 0.2	189.3 ± 7.4	27.7
573	10	53	225.8 ± 3.6	2.1 ± 0.1	221.7 ± 5.0	8.1
648	22.5	96	203.8 ± 71.2	1.6 ± 0.2	200.7 ± 67.7	8.0
698	22.5	168	202.5 ± 7.7	2.0 ± 0.6	205.5 ± 5.5	3.6
748	22.5	158	138.2 ± 27.6	1.6 ± 0.6	144.0 ± 23.6	4.8
798	22.5	146	138.4 ± 4.3	1.4 ± 0.4	136.8 ± 2.7	8.2

*Uncertainties correspond to 95% confidence intervals.

Table 6.4 Mean residence times, Péclet numbers and the average *RMS* error obtained using Model 2.

T, K	P, MPa	Re	f	Pe_1	$\bar{\tau}_1, s$	Pe_2	$\bar{\tau}_2, s$	$\bar{\tau}_{ave}^a, s$	$RMS, \%$
298	2	5	0.37 ± 0.03	88.5 ± 16.8	169.2 ± 5.3	9.2 ± 0.5	319.3 ± 2.4	263.6 ± 4.3	5.7
473	5	34	0.37 ± 0.03	52.6 ± 14.9	111.8 ± 1.2	3.6 ± 0.3	310.8 ± 10.3	236.4 ± 9.1	3.2

*Uncertainties correspond to 95% confidence intervals.

$$^a \bar{\tau}_{ave} = f \cdot \bar{\tau}_1 + (1 - f) \cdot \bar{\tau}_2$$

6.6 Conclusion

A methodology for the evaluation of the hydrodynamic performance of flow-through SCWO reactors from the *ex situ* RTD measurements has been described. The method is based on the application of the transfer function concept for the deconvolution of the experimental RTD curves obtained with and without the reactor section. The main advantage of the described approach is that tracer injection and detection are performed outside the “hot zone” of the experimental SCWO apparatus, which allows for the use of standard analytical tools for tracer detection.

The pulse response experiments were carried out in a flow-through tubular SCWO reactor system from ambient to supercritical conditions. Phenol was used as a tracer compound. The behaviour of the reactor was characterized over a wide range of temperatures and pressures by calculating the mean residence time of the fluid and the degree of axial dispersion, the Péclet number. The obtained results suggest that above 573 K and 10 MPa the studied tubular reactor configuration behaves as a mixed system ($Pe \sim 1.4 - 2$). The results also indicate the presence of fast preferential flow in the reactor vessel below 473 K and 5 MPa.

References for Chapter 6

1. E. Fauvel, C. Joussot-Dubien, E. Pomier, P. Guichardon, G. Charbit, F. Charbit and S. Sarrade, *Ind. Eng. Chem. Res.* **42**, 2122 (2003).
2. M.D. Bermejo, F. Fernandez-Polanco and M.J. Cocero, *Ind. Eng. Chem. Res.* **44**, 3835 (2005).
3. K.S. Lieball, Doctoral Thesis no. 14911, Zurich, Switzerland: ETH (2003).
4. M.D. Bermejo, F. Fdez-Polanco and M.J. Cocero, *Ind. Eng. Chem. Res.* **45**, 3438 (2006).
5. V. Casal and H. Schmidt, *J. Supercrit. Fluids* **13**, 269 (1998).
6. Y. Calzavara, C. Jousot-Dubien, H.-. Turc, E. Fauvel and S. Sarrade, *J. Supercrit. Fluids* **31**, 195 (2004).
7. M.J. Cocero and J.L. Martinez, *J. Supercrit. Fluids* **31**, 41 (2004).
8. B. Veriansyah, J. Kim, J. Lee and Y. Lee, *J. Hazard. Mater.* **124**, 119 (2005).
9. G. Anitescu, L.L. Tavlarides and V. Munteanu, *AIChE J.* **50**, 1536 (2004).
10. J.T. Henrikson and P.E. Savage, *AIChE J.* **49**, 718 (2003).
11. C.Y. Wen and L.T. Fan, *Models for Flow Systems and Chemical Reactors*, Marcel Dekker Inc., New York (1973).
12. F. Vogel, J.L.D. Blanchard, P.A. Marrone, S.F. Rice, P.A. Webley, W.A. Peters, K.A. Smith and J.W. Tester, *J. Supercrit. Fluids* **34**, 249 (2005).
13. C.H. Oh, R.J. Kochan, T.R. Charlton and A.L. Bourhis, *Energy Fuels* **10**, 326 (1996).
14. N. Zhou, A. Krishnan, F. Vogel and W.A. Peters, *Adv. Environ. Res.* **4**, 75 (2000).
15. O. Levenspiel, *Chemical Reaction Engineering*, 3rd ed., Wiley & Sons (1999).

16. J. García-Serna, E. García-Verdugo, J.R. Hyde, J. Fraga-Dubreuil, C. Yan, M. Poliakoff and M.J. Cocero, *J. Supercrit. Fluids* **41**, 82 (2007).
17. A. Kruse and C. Lietz, *Chem. Eng. Technol.* **26**, 1119 (2003).
18. H.J. White Jr., J.V. Sengers, D.B. Neumann and J.C. Bellows, *Physical Chemistry of Aqueous Systems: Meeting the Needs of Industry*, Proceedings of the 12th International Conference on the Properties of Water and Steam. (1995).
19. T.D. Thornton, Doctoral Thesis, University of Michigan, Ann Arbor, MI (1991).
20. M. Koo, W.K. Lee and C.H. Lee, *Chem. Eng. Sci.* **52**, 1201 (1997).
21. I.C. van Nugteren-Osinga, M. Bos and W.E. van der Linden, *Anal. Chim. Acta* **214**, 77 (1988).
22. A. Abad, S. C. Cardona, J. I. Torregrosa, F. López and J. Navarro-Laboulais, *J. Math. Chem.* **V38**, 541 (2005).
23. C. Castelain, D. Berger, P. Legentilhomme, A. Mokrani and H. Peerhossaini, *Int. J. Heat Mass Transfer* **43**, 3687 (2000).
24. A.P. Torres and F.A.R. Oliveira, *J. Food Eng.* **36**, 1 (1998).
25. M.J. Hopkins, A.J. Sheppard and P. Eisenklam, *Chem. Eng. Sci.* **24**, 1131 (1969).
26. W.C. Clements, *Chem. Eng. Sci.* **24**, 957 (1969).
27. M.A. Fahim and N. Wakao, *Chem. Eng. J.* **25**, 1 (1982).
28. S.D. Kolev, *Anal. Chim. Acta* **308**, 36 (1995).
29. J.J. Batten, *Aust. J. Appl. Sci.* **12**, 11 (1960).

Chapter 7

Diffusion Coefficients of Phenol in Hot Compressed Water: *Ex situ* Taylor Dispersion Technique and Molecular Dynamics Simulations

7.1 Abstract

Application of *ex situ* flow injection method in combination with the Taylor dispersion technique to measurements of binary diffusion coefficients in high-temperature compressed water is presented. Diffusion coefficients for phenol in aqueous solution are measured at 25 MPa from 298 to 473 K. Self-diffusion coefficients for phenol in infinitely dilute aqueous solution are also calculated over a wide temperature and density range, including supercritical states, by means of the molecular dynamics simulation method. The values of limiting binary diffusion coefficient of phenol, obtained by using the *ex situ* Taylor dispersion method, agree well with available experimental and computer simulation data. The *ex situ* Taylor dispersion method is a promising technique for diffusion measurements in high-temperature and supercritical water.

7.2 Introduction

Technological applications of high-temperature and supercritical water for power generation, hazardous waste utilization, materials processing, etc. have attracted much attention over the last two decades.¹⁻⁶ Despite significant research in the area, very little is known about mass transfer coefficients of organic and inorganic solutes in aqueous solutions at elevated temperatures and pressures. This is primarily due to experimental difficulties in conducting diffusivity measurements in the sub- and supercritical region ($T_c = 647$ K and $p_c = 22.1$ MPa for water). Up-to-date only a few experimental measurements of diffusion coefficients in hot compressed water have been reported.⁷⁻¹⁴ The technical problems in determining mass transfer coefficients in aqueous solutions at extreme conditions have prompted application of molecular dynamics simulation methods.¹⁵⁻²⁶ The need for additional data and validation of molecular simulation results necessitate the development of accurate and easy-to-use experimental methods for diffusion measurements at sub- and supercritical water conditions.

Amongst the methods^{27,28} employed for diffusion measurements in supercritical fluids, the most commonly used is the Taylor dispersion technique^{29,30}, see Refs. [27, 31-38] and therein. The method is based on the dispersion measurement of a narrow pulse of a solute (pure or in solution) flowing through a long tube of uniform diameter in a fully developed laminar flow. The Taylor dispersion technique (a.k.a. the capillary peak broadening method) combines experimental simplicity with high achievable accuracy. The fundamentals and practical applications of the Taylor dispersion technique have been described in-detail by Alizadeh *et al.*³⁹, Levelt Sengers *et al.*³¹, Funazukuri³² and others. Unfortunately, application of the Taylor dispersion method to diffusion measurements at extreme experimental conditions *in situ* is difficult and requires

sophisticated analytical equipment capable of withstanding high temperatures and pressures. To our knowledge, only one experimental investigation of diffusion coefficients in sub- and supercritical water using the *in situ* Taylor dispersion technique has been reported by Goemans *et al.*¹⁰

Recently, we have developed the *ex situ* flow injection methodology, which has been successfully applied to the examination of the hydrodynamic regime of a flow-through tubular reactor under supercritical water conditions.⁴⁰ The main advantage of the *ex situ* method is that the sample injection and detection are performed outside the “hot zone” of the experimental apparatus, which allows for the use of standard “off-the-shelf” injectors and flow-through detectors.

The goal of this study is two-fold. First, to test the applicability of the *ex situ* method to the Taylor dispersion technique for diffusion measurements by examining the limiting binary diffusion coefficients of phenol from ambient to supercritical conditions. Second, to calculate the molecular self-diffusion coefficient of phenol in infinitely dilute aqueous solution over a wide temperature and density range by means of the molecular dynamics (MD) simulation method.

The remainder of this chapter is organized as follows. The *ex situ* experimental approach is explained in Section 7.3. The experimental apparatus and procedures are described in Section 7.4. The results are discussed in Section 7.5. Our conclusions are given in Section 7.6.

7.3 *Ex situ* Taylor dispersion technique

The experimental approach is schematically illustrated in Fig. 7.1. Essentially, the *ex situ* flow injection method is a modification of the two point measurement technique^{32,41}, where the impulse and response signals are recorded *in situ* at the entrance and exit of a section of the experimental apparatus under investigation, see Fig. 7.1(a). In contrast, the *ex situ* experiment, Fig. 7.1(b), is conducted in two stages. In Stage 1, the dispersion of a solute pulse in the flow system is measured without the diffusion tube, whereas in Stage 2, performed under identical experimental conditions as in Stage 1, the dispersion of a pulse is recorded with the diffusion tube installed. The extent of dispersion of a solute pulse in the diffusion tube *alone* can be calculated from the deconvolution of the response curves obtained in Stages 1 and 2, by using the same methodology as in typical two point measurement experiments. The deconvolution methodology is described in detail elsewhere^{32,40,41}, here we provide a concise overview.

The response curve of a tracer can be viewed as a convolution of several functions that characterize the flow in each individual section of the experimental apparatus (injector, preheater, diffusion tube, temperature exchanger, back-pressure regulator, detector, various fittings, etc.). In Laplace space, the response of a system without the section of interest (in this case, diffusion tube) can be written as:

$$r_1(s) = p(s) \cdot h_A(s) \cdot h_B(s), \quad (7.1)$$

where $p(s)$ is the Laplace transform of the normalized input pulse function, $P'(t)$, and transfer functions $h_A(s)$ and $h_B(s)$ characterize the flow in the fore- and after- sections of the experimental apparatus, respectively.

The response of the system with the diffusion tube installed is given in the Laplace domain by:

$$r_2(s) = p(s) \cdot h_A(s) \cdot h_D(s) \cdot h_B(s), \quad (7.2)$$

where $h_D(s)$ is the transfer function of the diffusion tube of the flow system.

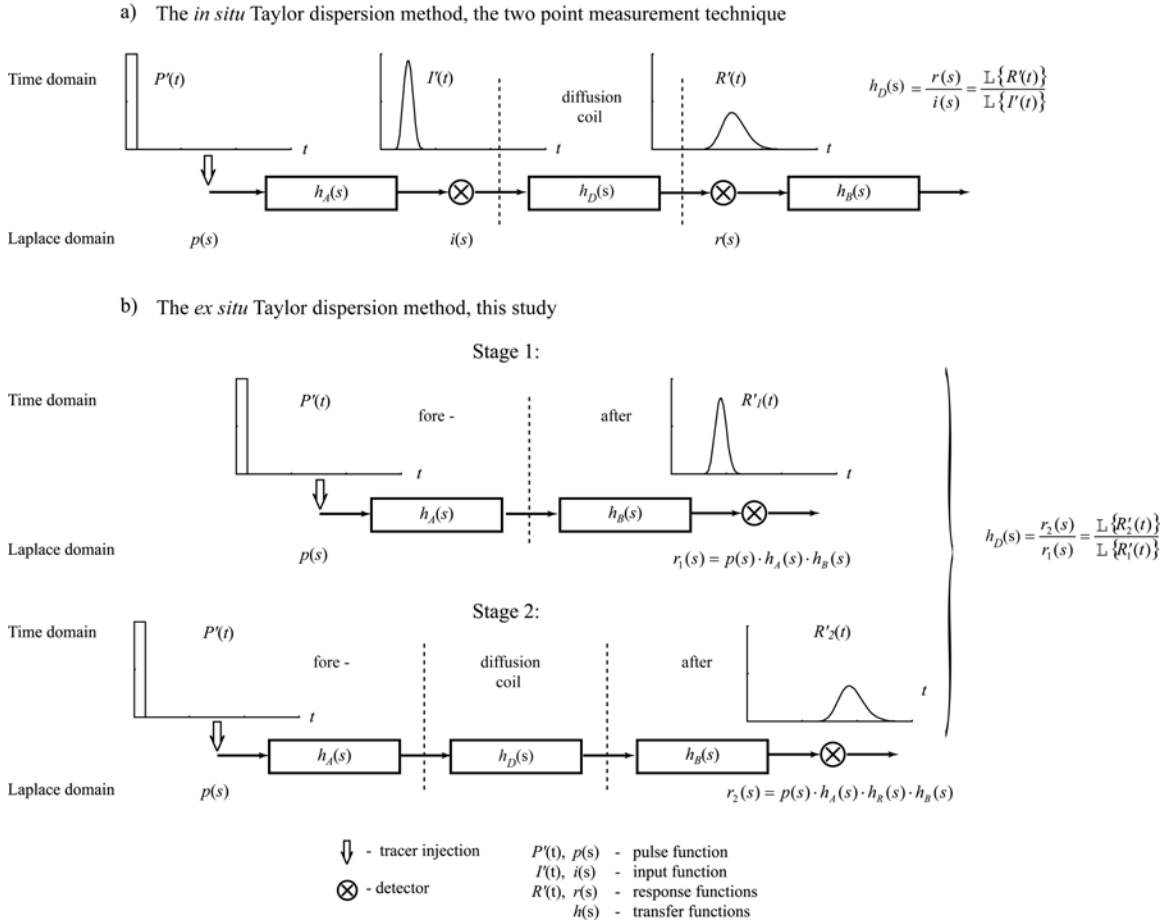


Figure 7.1 Schematic diagrams of the a) *in situ* and b) *ex situ* Taylor dispersion techniques

Thus, the transfer function of the diffusion tube, $h_D(s)$, can be found from the deconvolution of the two normalized experimental response curves $R'_2(t)$ and $R'_1(t)$:

$$h_D(s) = \frac{r_2(s)}{r_1(s)} = \frac{\mathcal{L}\{R'_2(t)\}}{\mathcal{L}\{R'_1(t)\}}. \quad (7.3)$$

An analytical expression for a transfer function can be derived from its definition, Eq. 7.4, using a particular flow model and appropriate boundary conditions:

$$h(s) = \frac{\mathcal{L}\{R'(t)\}}{\mathcal{L}\{I'(t)\}} = \frac{\int_0^{\infty} R'(t)e^{-st} dt}{\int_0^{\infty} I'(t)e^{-st} dt} = \frac{r(s)}{i(s)}, \quad (7.4)$$

where s is the Laplace space variable, $r(s)$ and $i(s)$ are the Laplace transforms of the normalized time domain input, $I'(t)$, and output, $R'(t)$ response curves.

The dispersion of an inert solute in a steady-state laminar flow through a tube of uniform diameter can be described by a one-dimensional differential equation for the concentration perturbation averaged over a cross section, or the Axially Dispersed Plug Flow³⁹ model (ADPF):

$$\frac{\partial C}{\partial t} = D_a \frac{\partial^2 C}{\partial x^2} - \bar{u}_0 \frac{\partial C}{\partial x}, \quad (7.5)$$

where C is the solute concentration, D_a is the axial dispersion coefficient and \bar{u}_0 is the cross section averaged axial velocity of the fluid. The binary diffusion coefficient of a solute, D_{12} , is related to the axial dispersion coefficient, D_a , via^{29,39}:

$$D_a \cong D_{12} + \frac{\bar{u}_0^2 d_0^2}{192 \cdot D_{12}} \quad (7.6)$$

where d_0 is the inner diameter of the tube. Note, that Eq. 7.6 is subject to certain experimental conditions discussed by Alizadeh *et al.*³⁹

The transfer function for the ADPF model (Eq. 7.5) with small extents of dispersion ($Pe_L > 500$) is given by⁴²:

$$h^{ADPF}(s) = \exp\left[\frac{Pe_L}{2}(1 - \phi)\right] \quad (7.7)$$

where $\varphi = \sqrt{1 + \frac{4 \cdot s \cdot \bar{\tau}}{Pe}}$ and $Pe_L = \frac{\bar{u}_0 L}{D_a}$ is the Péclet number, $\bar{\tau}$ is the mean residence time of the fluid in the system and L is the characteristic length of the section of experimental apparatus. From (7.3) and (7.7) it follows that

$$\exp\left[\frac{Pe_L}{2}(1 - \varphi)\right] = \frac{\int_0^{\infty} R_2'(t)e^{-st} dt}{\int_0^{\infty} R_1'(t)e^{-st} dt}. \quad (7.8)$$

The transfer function parameters, namely the mean residence time, $\bar{\tau}$, and Péclet number, Pe_L , can be obtained from experimental response curves $R_1'(t)$ and $R_2'(t)$ by using the time domain curve-fitting procedure, described by Fahim⁴³. Finally, the binary diffusion coefficient is calculated from Eq.7.6 with \bar{u}_0 and D_a given by:

$$\bar{u}_0 = \frac{L}{\bar{\tau}} \quad (7.9)$$

and

$$D_a = \frac{\bar{u}_0 L}{Pe_L}. \quad (7.10)$$

The proposed experimental approach addresses the main technical issues of conducting experimental measurements in high-temperature and supercritical water. First, the detection of the response curve is performed at ambient conditions *after* cooling and depressurization, which significantly simplifies experimental set up. Secondly, sample injection into a pressurized carrier fluid is carried out at ambient temperature, eliminating problems associated with injection into compressible fluids. Thirdly, the deconvolution approach accounts for the finite volume of the injected sample, the finite volume of the detector, as well as all variations in the fluid velocity profile in both the fore- and after- sections of the experimental apparatus due to capillary

curvature, its non-uniformity and the presence of various fittings (unions, back-pressure regulator, etc). It is important to emphasize that a sufficiently long preheater section must be installed in order to ensure that dispersion measurements are conducted at isothermal conditions.

7.4 Experimental Apparatus and Procedures

7.4.1 Experimental Apparatus

The schematics and photograph of the experimental apparatus is shown in Fig. 7.2. The apparatus consists of two HPLC pumps (Bio-Rad® 1330 and Waters® 590). One pump was used to deliver pure degassed deionized water, which serves as a carrier fluid, while the other pump, connected to the sample injection valve, was used for loading the sample loop with aqueous phenol solution. A six-port two-position electrically actuated sample injection valve (Valco®), equipped with a 250 μ L sample loop (i.d. = 0.03") was employed. To avoid pressure drop upon the injection event, the sample loop was pressurized to the same operating conditions as the flow system. All parts of the flow-through apparatus were constructed of stainless steel SS316 tubing and connected using SS316 zero dead volume unions (Valco®). Note, all tubing and fittings of the flow injection manifold have internal diameter of 0.03" (\sim 0.762 mm). The carrier water was preheated to the operating temperature by passing through a 3.0 m coiled capillary tube. A 3.10 m coiled diffusion tube with coil diameter of 25 mm was used in this study. The inner diameter of the diffusion tube was determined gravimetrically in a separate set of experiments to be 0.7847 mm. The coiling ratio, $\omega = D_c/d_0$, of the diffusion tube in this study is 31.86. The preheater and the diffusion tube fit inside a high temperature oven. Oven temperature was controlled by a thermostat (Omega® CN2110) equipped with a K-thermocouple. A custom built heat exchanger

($L = 2.5$ m), coupled to a cold plate (TE Technology, Inc.) was used to cool down the effluent to ambient temperature. The temperature of the heat exchanger was maintained at 25 °C by a temperature controller (TE Technology, TC-24-25). The pressure in the system was controlled by adjustable back pressure regulators (Upchurch® P-880) and monitored using a Nupro® pressure gauge. The pressure gauge was installed upstream from the sample injection valve. Cooled and depressurized effluent was passed through a 10 mm optical path stainless steel flow cell (FIA-Z-SMA, FIA Inc.). On-line spectroscopic measurements were performed using an Ocean Optics® USB-2000 UV-Vis spectrometer equipped with a CCD camera.

7.4.2 Experimental procedure and flow parameters

Two sets of flow injection experiments were performed. The first series of experiments was conducted without the diffusion tube in order to obtain the response curves of the injection section (fore- and after- sections) of the experimental apparatus. The preheater was connected directly to the heat exchanger using a zero dead-volume union. The second series of experiments was performed at identical operating conditions as the first one, but with the diffusion tube installed. In both sets of experiments at least four individual measurements were performed at each state point. In order to minimize the effect of diffusion tube curvature on the dispersion of a solute due to elongation of the velocity profile and the presence of secondary flows, the volumetric flow rate at the pump in all experiments was set at 50 $\mu\text{L}/\text{min}$. According to Eq. 71 of Ref. [39] deviations from the straight tube behaviour at this flow rate at all experimental conditions examined do not exceed 0.2 %. The gravimetrically measured average flow rate in all experiments was determined to be 47.693 ± 0.069 $\mu\text{L}/\text{min}$. Instantaneous pressure fluctuations due to the HPLC pump were about 0.15 MPa.

In this study we have chosen to examine the limiting binary diffusion coefficients of phenol, primarily due to its high thermal stability at elevated temperatures and pressures.^{44,45} Standard 1000 ppm aqueous phenol solution (LabChem Inc.) was diluted to prepare fresh 50 ppm (0.531 mmol/L) working solutions. Prior to each injection, the system was allowed to stabilize at set operating conditions for about two hours. After that, a sequence of four square-wave pulses was introduced into the manifold. Note that application of a complex input function, used in this study, helps to minimize uncertainty in obtaining fitting parameters in the deconvolution procedure. The sample injection valve was controlled by a custom build programmable timer. The time delay between sequential pulses was set to be precisely 20 min. At the operating flow rate, the duration of a single square pulse in this study was approximately 315 s. The beginning of spectra acquisition was synchronized with the first injection event. The primary channel of the spectrometer was used to monitor phenol absorbance at a wavelength of 270 nm. The baseline spectrum was collected at 500 nm. The spectrometer acquisition time was set at 1 sec.

In order to ensure correct mass balance during diffusion measurements, the total concentration of phenol was calculated from the obtained response curves and compared with the total concentration of injected tracer. In this study, more than 98% of the injected phenol was detected in each individual experiment.

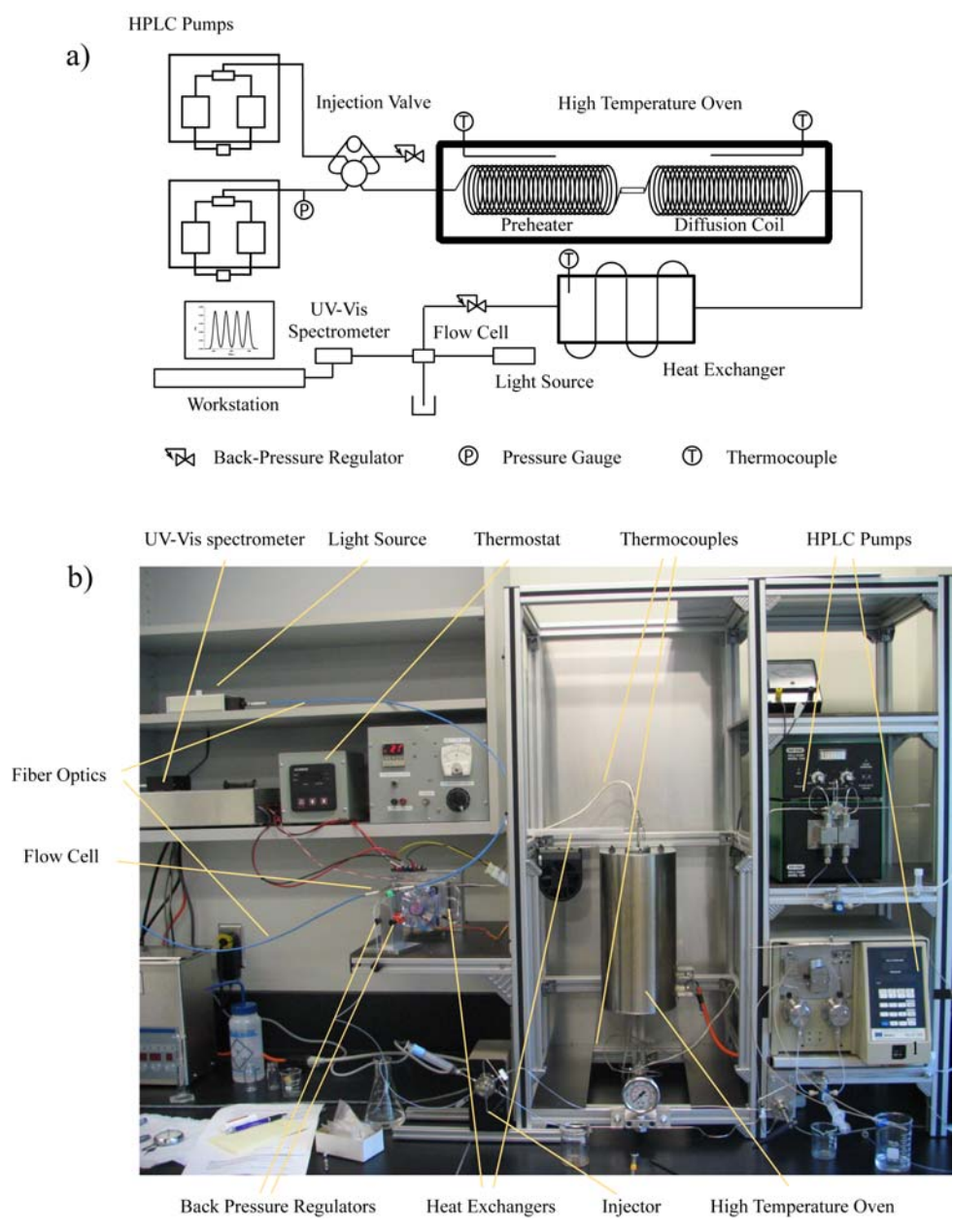


Figure 7.2 a) Schematic diagram and b) photograph of the experimental apparatus

7.4.3 Simulation details

Simple Point Charge Extended (SPC/E) model of Berendsen *et al.*⁴⁶ for water was used in this study. Among several rigid point charge models for phenol found in literature⁴⁷⁻⁴⁹, we have used the model of Mooney *et al.*⁴⁹ The charges, geometry and Lennard-Jones (LJ) parameters used in this work are given in Table 7.1.

Molecular dynamics simulations were carried out in the *NVT* and the *NPT* ensembles. Constant density simulations were performed from 0.2 to 1.0 g/cm³ at 298, 373, 473, 573, 673 and 773 K. The constant pressure simulations were carried out over the same temperature range with the model fluid pressure set at 18.6 MPa which corresponds to approximately 25 MPa of the real fluid (the same corresponding states were simulated as in experimental measurements). Note, that the critical pressure of the SPC/E water was estimated to be 16.3 MPa by Hayward and Svishchev⁵⁰, 16.0 MPa by Guissani and Guillot⁵¹ and 16.4 MPa by Plugatyr and Svishchev⁵². The system size was 503 water molecules and 1 phenol molecule. The isokinetic equations of motions were integrated using the forth-order Gear algorithm⁵³ with a time step of 1 fs. Rotational degrees of freedom were represented using quaternions⁵⁴. The equilibrated simulation run lengths were 500 ps. The long-range Coulomb forces were evaluated using the Ewald summation technique in cubic periodic boundary conditions. The cutoff distance for the LJ interactions was set at half of the cell length. The translational self-diffusion coefficients were calculated from the velocity autocorrelation function, with the statistical uncertainty being around 10%. The simulations were carried out on a Linux-based parallel Transport GX28 system with dual 64 bit AMD Opteron processors.

Table 7.1 Electrostatic, geometric and Lennard-Jones parameters for water and phenol models

Species	Atom	ϵ , kJ/mol	σ , Å	q , e	r , Å	\angle , deg
H_2O^a	H	0	0	0.4238		
	O	0.6517	3.166	-0.8476	1.0	109.47 (H-O-H)
$C_6H_5OH^b$	H	0	0	0.44		
	O	0.650	3.07	-0.64	0.960 (H-O)	110.5 (H-O-C)
	C _{aro:1}	0.294	3.55	0.54	1.364 (C-O)	120.0 (O-C-C)
	C _{aro:2,6}	0.294	3.55	-0.4125	1.390 (C-C)	120.0 (C-C-C)
	C _{aro:3,5}	0.294	3.55	-0.03		120.0 (C-C-H)
	C _{aro:4}	0.294	3.55	-0.30		
	H _{aro:2,6}	0.126	2.42	0.20	1.08 (C-H)	180.0 (dihedral)
	H _{aro:3,5}	0.126	2.42	0.143		
	H _{aro:4}	0.126	2.42	0.159		

^a Ref. [46]; ^b Ref. [49].

7.5 Results and Discussion

Normalized experimental response curves obtained at 298, 373 and 473 K and 25 MPa are shown in Fig. 7.3. As can be seen from this figure, all individual peaks are nearly Gaussian in shape and exhibit excellent reproducibility within each run. The reproducibility of the response curves obtained at identical experimental conditions (i.e. between runs) was evaluated by calculating the average root mean square (*RMS*) deviation, Eq. 7.11. In this study the mean *RMS* deviation was determined to be 0.5 and 1.4% for the response curves obtained without and with the diffusion tube, respectively.

$$RMS = \sqrt{\frac{\int_{t_1}^{t_2} (R'_a(t) - R'_b(t))^2 dt}{\int_{t_1}^{t_2} (R'_a(t))^2 dt}}, \quad (7.11)$$

where functions $R'(t)$ represent normalized response curves and subscripts a and b identify different runs.

Due to the fact that the experiments performed with and without diffusion tube are independent in nature, the statistical analysis was performed using all combinations of the response curves, $R'_1(t)$ and $R'_2(t)$, obtained at identical experimental conditions. The fitting parameters of the ADPF model, namely, the mean residence time, $\bar{\tau}$, and the Péclet number, Pe_L were obtained by using the time-domain fitting procedure⁴³. In this study, the average RMS of the fit does not exceed 0.05 %.

In order to validate the proposed experimental method we have performed measurements at ambient conditions. The value of the limiting binary diffusion coefficient of phenol in aqueous solution at 298 K and 0.1 MPa obtained in this study is $0.996 \times 10^{-9} \text{ m}^2/\text{s}$. Our result is somewhat higher than that of Yang and Matthews⁵⁵ ($0.925 \times 10^{-9} \text{ m}^2/\text{s}$ at 298.15 K) and Castillo *et al.*⁵⁶ ($0.940 \times 10^{-9} \text{ m}^2/\text{s}$ at 296.2 K), but agrees well with the value of $0.998 \times 10^{-9} \text{ m}^2/\text{s}$, reported by Niesner and Heintz⁵⁷, and the result from our computer simulation of $1.05 \times 10^{-9} \text{ m}^2/\text{s}$.

The limiting binary diffusion coefficients for phenol, obtained in this study, are given in Table 7.2 along with experimental flow parameters. The results of our computer simulations are shown in Table 7.3. The experimental and simulation data along with available literature values are shown in Fig. 7.4. Note, that all previous experiments were conducted at ambient pressure with the highest temperature examined being 343 K by Castillo *et al.*⁵⁶ We report experimental diffusion coefficients for phenol in aqueous solution obtained at a much higher pressure of 25

MPa and over a significantly wider temperature range from 298 to 473 K. The binary diffusion coefficient for phenol in aqueous solution at 25 MPa was determined to be 1.17×10^{-9} , 2.82×10^{-9} and 7.38×10^{-9} m²/s at 298, 373 K and 473 K, respectively. These values are in agreement, within statistical uncertainty, with our molecular simulation results of 1.12×10^{-9} , 2.61×10^{-9} and 7.39×10^{-9} m²/s at the corresponding state points.

The main experimental uncertainty in estimation of the diffusion coefficients in this work comes from the values of the Péclet number, Pe_L , obtained from the fit. In our experiments Pe_L values increase from about 680 at 298 K to approximately 2150 at 473 K with corresponding increase in uncertainty of the fit from 3.5 to 14 %. It should be mentioned, that rather high uncertainty in Péclet numbers at elevated temperatures is mainly due to the limitation of the experimental apparatus, namely the length of diffusion column (3.1 m). Increased fluid velocity at higher temperatures (lower densities) combined with faster solute diffusion result in very small differences in the shape of the response curves obtained with and without the diffusion tube, which, ultimately affects the accuracy in determining the fitting parameter, Pe_L . In this study we report values of the diffusion coefficient of phenol only up to 473 K, as the error margins at higher temperatures may exceed 30 % with the employed diffusion column geometry.

The simulation data along the experimental 25 MPa isobar is shown in Fig. 7.4. As can be seen from this figure, the self-diffusion coefficient of phenol increases dramatically with temperature as the critical point of water is approached. Thus, at temperatures of 673 K and 773 K its value was calculated to be 68.3×10^{-9} and 128.5×10^{-9} m²/s, respectively. Such behaviour can be attributed to the combined effect of increased thermal motion at elevated temperatures and the disappearance of the H-bonded network structure of water at near and supercritical conditions.

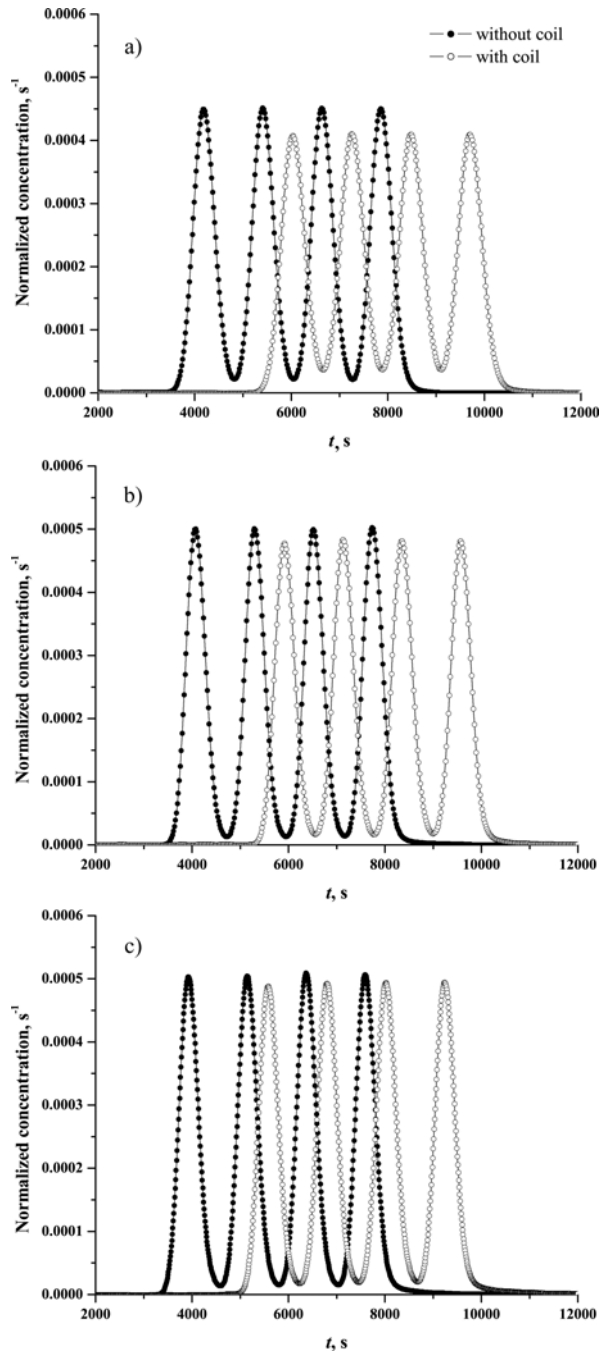


Figure 7.3 Examples of the response curves obtained with and without diffusion coil at 25 MPa and a) 298 K, b) 373 K and c) 473 K.

Table 7.2 Flow parameters and the limiting binary diffusion coefficient of phenol obtained by using the *ex situ* Taylor dispersion technique.

T, K	P, MPa	$\eta^a, \mu Pa s$	Re	De	Sc	$De Sc^{1/2}$	$D_{expt.} \times 10^9, m^2/s$
298.15	0.1	890.9	1.45	0.26	897.1	7.68	0.996 ± 0.026
298.15	25	887.6	1.45	0.26	752.6	7.06	1.17 ± 0.04
373.15	25	288.7	4.47	0.79	105.6	8.13	2.82 ± 0.15
473.15	25	140.0	9.21	1.63	21.5	7.57	7.38 ± 1.94

^a Values were obtained from the IAPS Formulation 1985 for the Viscosity of Ordinary Water Substance.⁵⁸

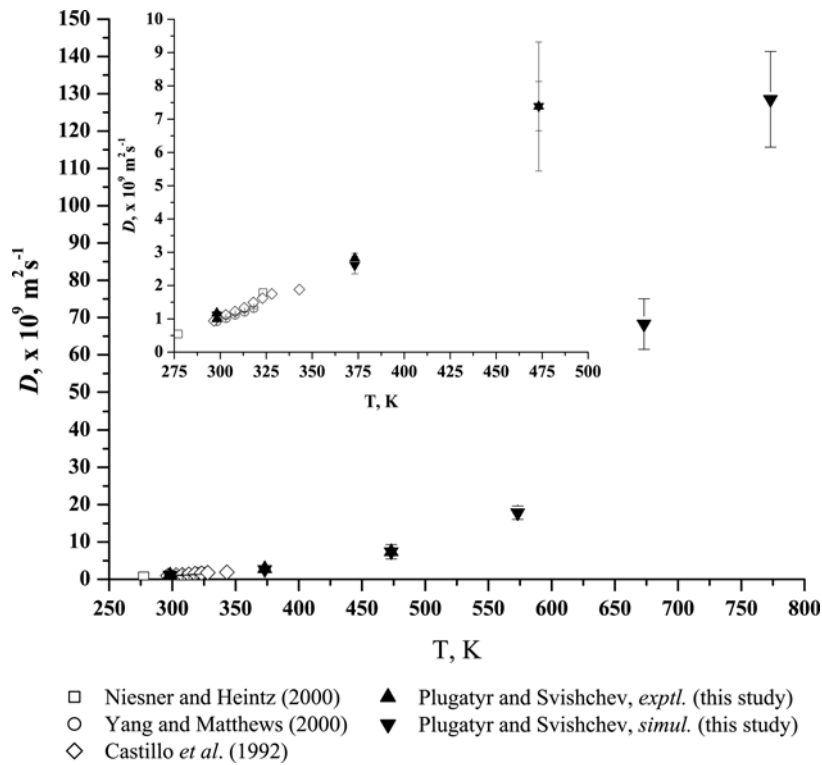


Figure 7.4 Temperature dependence of the binary diffusion coefficient of phenol in aqueous solution. The insert shows low temperature data.

Table 7.3 Self-diffusion coefficients of phenol in aqueous infinitely dilute solution obtained by using MD simulations.

$\rho, \text{g/cm}^3$	T, K	P^*, MPa	$D_{\text{simul.}} \times 10^9, \text{m}^2/\text{s}$
1.0	298.15		1.05
	373.15		2.57
	473.15		5.79
	573.15		7.12
	673.15		7.79
	773.15		11.15
0.8	298.15		1.89
	373.15		4.75
	473.15		8.53
	573.15		10.92
	673.15		14.08
	773.15		16.56
0.6	573.15		21.07
	673.15		25.53
	773.15		27.13
0.4	673.15		32.45
	773.15		41.52
0.2	673.15		59.96
	773.15		71.22
	298.15	18.6	1.12
	373.15	18.6	2.61
	473.15	18.6	7.39
	573.15	18.6	17.83
	673.15	18.6	68.26
	773.15	18.6	128.5

* Corresponds to approximately 25 MPa of real water.

7.6 Conclusion

The application of the *ex situ* flow injection technique in combination with the Taylor dispersion method to binary diffusion coefficient measurements in high-temperature compressed water was investigated. The self-diffusion coefficient for phenol in infinitely dilute aqueous solution was calculated over a wide temperature and density range by means of MD simulations.

The proposed *ex situ* experimental approach was validated by performing diffusion measurements of phenol in aqueous solution at temperatures from 298 to 473 K and pressures of 0.1 and 25 MPa. The results obtained in this study are in excellent agreement with available experimental and simulation data. The *ex situ* Taylor dispersion technique is a promising method for measurements of the diffusion coefficients in sub- and supercritical water. This study provides new experimental and simulation data on the diffusivity of phenol in water over a wide range of state parameters; further mass transfer studies of high-temperature and supercritical aqueous fluids are underway.

7.7 References for Chapter 7

1. M.D. Bermejo, and M.J. Cocero, *AIChE J.* **52**, 3933 (2006).
2. A. Kruse, and E. Dinjus, *J. Supercrit. Fluids* **39**, 362 (2007).
3. A. Kruse, and E. Dinjus, *J. Supercrit. Fluids* **41**, 361 (2007).
4. A. Kruse, and H. Vogel, *Chem. Eng. Technol.* **31**, 1241 (2008).
5. P. MacDonald, J. Buongiorno, J.W. Sterbentz, C. Davis and R. Witt, *Feasibility Study of Supercritical Light Water Cooled Reactors for Electric Power Production*. Nuclear Energy, Research Initiative Project 2001-001 INEEL/EXT-04-02530 .
6. J. Kronholm, K. Hartonen, M. Riekkola, *Trac-Trends Anal.Chem.* **26**, 396 (2007).
7. W.J. Lamb, G.A. Hoffman, J. Jonas, Self-Diffusion in Compressed Supercritical Water. *J. Chem. Phys.* **74**, 6875 (1981).
8. W.M. Flarsheim, Y.M. Tsou, I. Trachtenberg, K.P. Johnston, A.J. Bard, *J. Phys. Chem.* **90**, 3857 (1986).
9. T.J. Butenhoff, M.G.E. Goemans, S.J. Buelow, *J. Phys. Chem.* **100**, 5982 (1996).
10. M.G.E. Goemans, *Mass Transfer in SCWO Process: Molecular Diffusion and Mass Transfer Coefficients of Inorganic Nitrate Species in Sub- and Supercritical Water*, Proceedings of the Second International Symposium on Environmental Applications of Advanced Oxidation Technologies (1996).
11. C.Y. Liu, S.R. Snyder, A.J. Bard, *J. Phys. Chem. B* **101**, 1180 (1997).
12. L.N. Trevani, E. Calvo, H.R. Corti, *J. Chem. Soc. Faraday T.* **93**, 4319 (1997).

13. K. Yoshida, C. Wakai, N. Matubayasi, M. Nakahara, *J. Chem. Phys.* **123**, 164506 (2005).
14. K. Yoshida, N. Matubayasi, M. Nakahara, *J. Chem. Phys.* **125**, 074307 (2006).
15. P.B. Balbuena, K.P. Johnston, P.J. Rossky, J.K. Hyun, *J. Phys. Chem. B* **102**, 3806 (1998).
16. G.H. Goo, G.H. Sung, S.H. Lee, *Mol. Simulat.* **30**, 37 (2004).
17. J.K. Hyun, K.P. Johnston, P.J. Rossky, *J. Phys. Chem. B* **105**, 9302 (2001).
18. M. Kubo, R.M. Levy, P.J. Rossky, N. Matubayasi, M. Nakahara, *J. Phys. Chem. B* **106**, 3979 (2002).
19. S.H. Lee, *Mol. Simulat.* **30** 669 (2004).
20. S.H. Lee and P.T. Cummings, *J. Chem. Phys.* **112**, 864 (2000).
21. C. Nieto-Draghi, J.B. Avalos, O. Contreras, P. Ungerer, J. Ridard, *J. Chem. Phys.* **121**, 10566 (2004).
22. J.P. Noworyta, S. Koneshan, J.C. Rasaiah, *J. Am. Chem. Soc.* **122**, 11194 (2000).
23. T. Ohmori, and Y. Kimura, *J. Chem. Phys.* **119**, 7328 (2003).
24. A. Plugatyr, I. Nahtigal, I.M. Svishchev, *J. Chem. Phys.* **124**, 024507 (2006).
25. I.M. Svishchev, A. Plugatyr, I.G. Nahtigal, *J. Chem. Phys.* **128**, 124515 (2008).
26. I.M. Svishchev, and A.Y. Plugatyr, *J. Phys. Chem. B* **109**, 4123 (2005).
27. T. Funazukuri, C.Y. Kong, S. Kagei, *J. Supercrit. Fluids* **46**, 280 (2008).
28. K.K. Liong, P.A. Wells, N.R. Foster, *J. Supercrit. Fluids* **4**, 91 (1991).
29. R. Aris, *Proc. Roy. Soc. Lond.* **A235**, 67 (1956).
30. G.I. Taylor, *Proc. Roy. Soc. Lond.* **A219**, 186 (1953).

31. J.M.H. Levelt Sengers, U.K. Deiters, U. Klask, P. Swidersky, G.M. Schneider, *Int. J. Thermophys.* **14**, 893 (1993).
32. T. Funazukuri, C.Y. Kong, S. Kagei, *J. Chromatogr. A* **1037**, 411 (2004).
33. H. Weingartner, U. Klask, G.M. Schneider, *Z. Phys. Chemie-Int. J. Res. Phys. Chem. Chem. Phys.* **219**, 1261 (2005).
34. T. Funazukuri, C.Y. Kong, S. Kagei, *J. Supercrit. Fluids* **38**, 201 (2006).
35. C.Y. Kong, T. Funazukuri, S. Kagei, *J. Supercrit. Fluids* **37**, 359 (2006).
36. O. Suarez-Iglesias, I. Medina, C. Pizarro, J.L. Bueno, *Fluid Phase Equilib.* **260**, 279 (2007).
37. C. Pizarro, O. Suarez-Iglesias, I. Medina, J.L. Bueno, *Ind. Eng. Chem. Res.* **47**, 6783 (2008).
38. O. Suarez-Iglesias, I. Medina, C. Pizarro, J.L. Bueno, *J. Chem. Eng. Data* **53**, 779 (2008).
39. A. Alizadeh, Nieto de Castro, C. A., W.A. Wakeham, *Int. J. Thermophys.* **1**, 243 (1980).
40. A. Plugatyr, and I.M. Svishchev, *J. Supercrit. Fluids* **44**, 31 (2008).
41. C. Castelain, D. Berger, P. Legentilhomme, A. Mokrani, H. Peerhossaini, *Int. J. Heat Mass Transfer* **43**, 3687 (2000).
42. A.P. Torres, and F.A.R. Oliveira, *J. Food Eng.* **36**, 1 (1998).
43. M.A. Fahim, and N. Wakao, *Chem. Eng. J.* **25**, 1 (1982).
44. T.D. Thornton, *Phenol Oxidation in Supercritical Water: Reaction Kinetics, Products and Pathways*. Doctoral Thesis, University of Michigan, Ann Arbor, MI (1991).
45. M. Koo, W.K. Lee, C.H. Lee, *Chem. Eng. Sci.* **52**, 1201 (1997).
46. H.J.C. Berendsen, J.R. Grigera, T.P. Straatsma, *J. Phys. Chem.* **91**, 6269 (1987).

47. K. Sagarik, and P. Asawakun, *Chem. Phys.* **219**, 173 (1997).
48. N.A. McDonald, H.A. Carlson, W.L. Jorgensen, *J. Phys. Org. Chem.* **10**, 563 (1997).
49. D.A. Mooney, F. Muller-Plathe, K. Kremer, *Chem. Phys. Lett.* **294**, 135 (1998).
50. T.M. Hayward, and I.M. Svishchev, *Fluid Phase Equilib.* **182**, 65 (2001).
51. Y. Guissani, and B. Guillot, *J. Chem. Phys.* **98**, 8221 (1993).
52. A. Plugatyr, and I.M. Svishchev, *Fluid Phase Equilib.* (accepted, Dec.8, 2009) .
53. D.J. Evans, and O.P. Morriss, *Comput. Phys. Rep.* **1**, 297 (1984).
54. D.J. Evans, *Mol. Phys.* **34**, 317 (1977).
55. X.N. Yang, and M.A. Matthews, *J. Colloid. Interface Sci.* **229**, 53 (2000).
56. R. Castillo, C. Garza, J. Orozco, *J. Phys. Chem.* **96**, 1475 (1992).
57. R. Niesner, and A. Heintz, *J. Chem. Eng. Data* **45**, 1121 (2000).
58. H.J. White Jr., J.V. Sengers, D.B. Neumann and J.C. Bellows, *Physical Chemistry of Aqueous Systems: Meeting the Needs of Industry*, Proceedings of the 12th International Conference on the Properties of Water and Steam. (1995).

Chapter 8

Summary and Future Outlook

The properties of hydrothermal fluids were examined by using MD simulations and flow injection methods. The MD simulations of naphthalene, aniline and phenol in aqueous infinitely dilute solution were performed from ambient to supercritical conditions. The hydration structures of naphthalene and aniline were analyzed with the aid of the radial, cylindrical and spatial distribution functions. The detailed spatial atomic density maps of water around solute molecules were presented. The coordination and H-bond numbers were calculated. The self-diffusion coefficients of naphthalene, aniline and phenol in sub- and supercritical water were also obtained. The results indicate that the hydration structures at near-critical conditions are drastically different from those in ambient water. The disappearance of the solvation shell is noted near the critical point of water. The changes in the hydration structures of solutes with temperature and density are reflected in the value of the self-diffusion coefficients which show a dramatic increase near the critical point of water.

The thermodynamic and dielectric properties of SPC/E water over a wide range of high-temperature and supercritical states were examined. The thermodynamic and dielectric EOS for high-temperature SPC/E water were parameterized. The thermodynamic EOS captures nicely the liquid-vapour coexistence curve of SPC/E water as well as the behaviour of the derivative properties and exhibits good extrapolation behaviour to temperatures and pressures beyond its parameterization range. The proposed thermodynamic and dielectric EOS provide the most accurate, up-to-date description of the properties of SPC/E water at elevated temperatures and pressures.

The experimental hydrothermal flow-through reactor system for the study of aqueous fluids at elevated temperatures and pressures has been constructed. Recognizing the difficulties of conducting physical measurements at supercritical water conditions, a novel *ex situ* flow injection methodology was developed. The method permits the use of standard “off-the-shelf” flow-through detectors in the study of hydrothermal fluids. The technique has been successfully applied to the examination of the hydrodynamic regime of a flow-through chemical reactor from ambient to supercritical water conditions. The developed *ex situ* Taylor dispersion technique has been used for measurements of the limiting binary diffusion coefficients of phenol in hot compressed water. The *ex situ* methodology provides a basis for application of flow-injection analysis methods in the study of hydrothermal fluids.

Considering the future development of emerging hydrothermal technologies for power generation, hydrogen production, etc. there is a need to explore properties of supercritical aqueous solutions well above the critical point of water. Despite recent progress in the development of experimental methods for the examination of aqueous systems at supercritical conditions, molecular simulations will likely become the main source of information at extreme temperatures and pressures. Therefore examination and standardization of the thermophysical properties of binary and multicomponent model systems, such as water-oxygen, water-hydrogen and water-nitrogen mixtures, at high-temperatures and pressures is of high priority. Prospective experimental studies will be aimed at further development of the *ex situ* methodology for direct kinetics measurements under supercritical water conditions.

Appendix A.1

Parameters of the GERG-2004 EOS (Eq. 5.3) for the SPC/E water potential.

<i>i</i>	<i>n_i</i>
1	0.1375067×10^1
2	-0.2714312×10^1
3	0.2291789
4	0.1235740×10^{-1}
5	0.1363098
6	$-0.4761535 \times 10^{-1}$
7	0.1070494×10^{-1}
8	-0.6433575
9	0.1904144×10^{-1}
10	0.1381584×10^{-1}
11	-0.2904775
12	0.1338702
13	$-0.5428815 \times 10^{-1}$
14	$-0.8407437 \times 10^{-2}$
15	$-0.5574307 \times 10^{-2}$
16	0.4128380×10^{-2}

$$\rho_c = 0.276 \text{ g/cm}^3$$

$$T_c = 640.25 \text{ K}$$

$$p_c = 164.37 \text{ bar}$$

$$R = 8.3114472 \text{ J mol}^{-1} \text{ K}^{-1}$$

$$MW(\text{H}_2\text{O}) = 18.015280 \text{ g mol}^{-1}$$

Appendix A.2

Parameters in Eqs. 5.9 and 5.10 for the saturated liquid and vapour densities for the SPC/E water potential.

<i>i</i>	<i>b_i</i>	<i>c_i</i>
1	1.68476	-1.08882
2	3.26727	-7.17605
3	-2.78144	3.80079
4	2.22876×10^1	-4.01415×10^1
5	6.12971×10^4	2.66399×10^2
6	7.69858×10^{13}	-1.83639×10^4

Appendix B.1

Parameters in the dielectric EOS (Eq. 5.8) for the SPC/E water potential.

<i>i</i>	<i>v_i</i>
1	1.295308×10^{-1}
2	5.766912×10^{-1}
3	1.703666
4	2.181501
5	-9.539024×10^{-2}
6	-1.498977×10^{-1}

Appendix B.1

Parameters in Eqs. 5.11 and 5.12 for the static dielectric constant for the SPC/E water potential along saturated liquid and vapour densities.

<i>i</i>	<i>k_i</i>	<i>l_i</i>
1	1.5438526	-1.718803
2	7.035231	-8.375979
3	1.410946×10^1	1.027206×10^1
4	1.185805×10^2	-4.853311×10^1
5	-1.449341×10^5	3.779133×10^2
6	1.555298×10^{14}	-2.667138×10^4

$$\varepsilon_c = 5.346$$